Thermal investigations on polymer dispersed liquid crystal composites and thermo-electric polymer composites using photothermal techniques

Maju Kuriakose

THERMAL INVESTIGATIONS ON POLYMER DISPERSED LIQUID CRYSTAL COMPOSITES & THERMO-ELECTRIC POLYMER COMPOSITES USING PHOTOTHERMAL TECHNIQUES

A THESIS

submitted to

L'UNIVERSITÉ DU LITTORAL - CÔTE D'OPALE

for the award of the degree of

Doctor of Philosophy in Physics

by

Maju KURIAKOSE

Defended on 26 June 2013 before the board of examiners consists of:

Agustín SALAZAR	PROFESSOR Universidad del País Vasco, Spain	Rapporteur
Gilles TESSIER	MAÎTRE DE CONFÉRENCES, HDR ESPCI Paris Tech	Rapporteur
Dorin DADARLAT	RESEARCHER SPECIALIST INCDTIM, Cluj-Napoca, Romania	Examinateur
Emmanuel GUILMEAU	CNRS SENIOR RESEARCHER CRISMAT, Université de Caen	Examinateur
Michaël DEPRIESTER	MAÎTRE DE CONFÉRENCES(Supervisor) Université du Littoral Côte d'Opale	Examinateur
Abdelhak HADJ SAHRAOUI	PROFESSOR (Director of Thesis) Université du Littoral Côte d'Opale	Examinateur

Unité de Dynamique et Structure des Matériaux Moléculaires

UNIVERSITÉ DU LITTORAL CÔTE D'OPALE

Acknowledgement

There is always a world of people behind the scenes, with supports, sacrifices and good hopes in order to accomplish each and every piece of work. My PhD thesis wouldn't exist without all of those my well wishers and supporters. Therefore, I would like to use this opportunity to thank everyone those who helped me to carry out this thesis work and also all those who have supported me to be what I am at present, as a professional and as a person.

Firstly, I would like to thank Dr. Jean-Marc BUISINE, Director of the Unité de Dynamique et Structure des Matériaux Moléculaires (UDSMM), for accepting my candidature as well as providing me all the necessary supports for my entire stay in France during the thesis work.

Equally, I am thankful to Dr. Abdelhak Hadj Sahraoui (Professor) and Dr. Michael Depriester (Maître de Conférences) for welcoming me as their student and giving me all scientific supports to do this PhD in UDSMM, Université du littoral côte d'opale (ULCO), Dunkerque.

Dr. Abdelhak has been an excellent mentor in all respects- kind, efficient, firm and meticulous in weeding out all weak links in my work, attitude and in my thesis. I am very happy and proud to say that I have been a part of his group. I am also grateful to him for being generous with my holidays whenever I wanted to visit my family in India, for all the conference trips that he funded and giving proper guidance and word of supports in the midst of difficult situations.

Michael has been a good friend, daily supervisor and upto a certain extend, my local guardian too, all rolled into one during the last two and a half years. He was sincerely attentive to all my doubts and ideas. He has been always with helping mentality and without his helps my earlier days in France, hardly knowing french, would be a real tragedy.

I am grateful to both of you for all your supports, corrections and reviews of my thesis

text and also for all the numerous enjoyable technical discussions.
Prof. Fréderick Roussel (Université de Lille 1) has been kind hearted for supplying some of the samples and passing their related informations. I am grateful to him for his contributions and supports.

My sincere thanks to the board of examiners, Dr. Agustín Salazar (Professor, Universidad del País Vasco, Spain) and Dr. Gilles Tessier (Maître de Conférences, ESPCI Paris Tech) as reporters, as well as Dr. Dorin Dadarlat (Research specialist, INCDTIM, Cluj-Napoca, Romania) and Emmanuel Guilmeau (CNRS Senior Researcher, CRISMAT, University of Caen) as examiners, for their kind acceptance to evaluate this thesis work and to come for the viva.

If there is a person who can claim, through him I am here, then that is Dr. Stéphane Longuemart. He has been a wonderful colleague, always open for discussions on scientific problems and kind hearted to help me during my arrival and stay in France by perceiving them in advance. I am deeply indebted to him for all his helps and advices.
I am also thankful to Sylvain Delenclos for helping me in preparing some of the samples and sharing his experiences.
Special thanks to Benoit Escorne, for his timely helps in needs of technical supports, and thanks to Benoit Duponchel, Chantal Dessailly for their administrative helps.

It is always hard to find places like this where its members embrace people from different cultures and considering them as their family. I never felt that I was in an alien environment even though there has been a big language barrier. My heartfelt thanks to Corinne Kolinsky, Abdelylah Daoudi, Philippe Hus, Fabrice Goutier, Mathieu Bardoux, Abdelaziz Elass, Remi Deram, Aoumeur Boulerouah, Yahia Boussoualem, Alejandro Segovia, and all other fellow workers as well as the members of the lab at Calais and Lille parts, for their supports, being treated me as a member among you and delivering me cheerful and enjoyable days.

Obtaining experience from experts are priceless blessings. I would be lacking of many scientific techniques, if I had not been at ATF, Katholieke Universiteit Leuven, Belgium. The year before starting of this PhD and a week during the thesis work, I have come across brand new ideas and activities while I was working under Prof. Christ Glorieux. I am grateful to him for all his scientific advices and supports. Also, I am thankful to Dr. Rajesh Ravindran Nair and Dr. Preethy C. Menon, post doctoral researchers, for their

assistance and generous supports on research activities at ATF.

Like many others, there was a cause for me also for choosing the field of Photothermal techniques and thermal transport studies as my favourite subject of research. It happened when I was being selected to conduct research works under the guidance of Prof. K. N. Madhusoodanan, Dept. of Instrumentation, Cochin University of Science and Technology (CUSAT), India. I am deeply indebted to him for introducing me this research field and providing me scholarship for my stay as well as grants for various research activities.
I am also grateful to Prof. Jacob Philip, Director, Sophisticated Tests and Instrumentation Centre, India for his valuable advices and many helps for continuing and extending my research career into European universities.

I have been fortunate to had many friends during my research career, all of them coloured my days both in India and Europe. They are: Nisha Radha, Nisha M. R., Uma S., Anu Philip & Subin, Ginson T. J., Prof. Raghu O., Prof. Manjusha K. P., Prof. Viji Chandra, Prof. Alex A. V., Prof. Benjamin, late prof. Satish, Sreeprasanth & Krishna, Joice Thomas & Nithya, Sandeep Sangameswaram & Parvathy, Dhanya, Vinay & Santhi, Lathesh K. C. & Ramya, Rany & Doni, Applonia, Rini, Minta, Liya, Suchithra Sundaram, Dr. Rojin & Sumitha, Mohanan chettan & Latha chechi, Mahesh Vyloppilly & Lakshmi, Jose and many more (extremely sorry to those whose names I missed!). I enjoyed their friendship and care very much.

Sharon Fellowship Church Karingachira, India., is not only a church but it is more or less a home for me. I am deeply indebted to all the church members and the pastor: Dr. Georgekutty K. B. as well as the previous pastors for their spiritual supports, advices and cares.

If there is any place where I get the highest of all- appreciation, love, compassion, support and acceptance, then that is my home. I am undoubtedly fortunate to born as the son of Mrs. Leela and Mr. M. A. Kuriakose. They educated me, protected me and fulfilled all my daily needs by sacrificing many of their happiness and well-being. Their priceless deeds couldn't be described here and a word of gratitude is just not worthy enough to honour them. I am grateful to both my parents for all their invaluable cares and blessings. This is also true while saying about my parent in-laws, Mr. T. M. Mathew and Mrs. Valsamma. Their righteous deeds astound me and their prayers keep me safe. Heartfelt thanks to both of them for all their cares.

I actually feel lucky and proud to be the one and only brother of Liju Kuriakose, a christian missionary to Chathisgarh, India., from whom I have gained my first scientific experiences, in his small home electronics lab. I have been always fascinated by his thoughts and social interactions. Many thanks to him and his wife, Lisa and their children, Abel and Angel for all their supports to me.

More than that, I am blessed for having Sharon Mathew and his wife Toniya along with their daughter Johanna, as well as our little Akku (though he is extra taller than me) as my brother in-laws. They are much like my own brothers and I am grateful to them for their loving heart towards me.

Many many thanks also to all my cousins, uncles and aunts, and neighbours for their cares and concerns.

"*A wife of noble character who can find? She is worth far more than rubies. Proverbs 31:10*". My wife, Sneha, can be best described by this verse. She has been with me during my entire PhD time, by sacrificing her professional life, helping and comforting me in all the difficulties and cheerfully waited for my return from lab late at night in many days. Moreover, she has been also a wonderful mother to our son, Johan. I am extremely thankful to her for making my PhD research life much easier.

"*Through him all things were made; without him nothing was made that has been made. John 1:3*". Looking back to the ways I have gone through, I would say 'God cares for me'. He made me, leads me and helps me. So, above all, I am richly blessed to have wonderful family, invaluable friends and excellent and outstanding mentors as my research guides. I give thanks to the almighty God- the Father, the Son and the Holy-spirit for all the loving kindness that He has bestowed upon me.

Maju Kuriakose

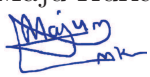

03-May-2013

Dunkerque

Picture of Peace

There once was a King who offered a prize to the artist who would paint the best picture of peace. Many artists tried. The King looked at all the pictures, but there were only two he really liked, and he had to choose between them.

One picture was of a calm lake. The lake was a perfect mirror for the peaceful towering mountains all around it. Overhead was a blue sky with fluffy white clouds. All who saw this picture thought that it was a perfect picture of peace.

The second picture had mountains, too. But these were rugged and bare. Above was an angry sky from which rain fell, and in which lightning played. Down the side of the mountain tumbled a foaming waterfall. This did not look peaceful at all. But when the King looked further, he saw behind the waterfall a tiny bush growing in a crack in the rock. In the plant a mother bird had built her nest. There, in the midst of the rush of angry water, sat the mother bird on her nest... a picture of perfect peace.

Which picture won the prize? The King chose the second picture. Why? "Because," explained the King, "peace does not mean to be in a place where there is no noise, trouble or hard work. Peace means to be in the midst of all those things and still be calm in your spirit. That is the real meaning of peace."

Author Unknown

List of Publications in Peer reviewed Journals

During PhD

1. Photothermoelectric Effect as a Means for Thermal Characterization of Nanocomposites Based On Intrinsically Conducting Polymers and Carbon Nanotubes

   Maju Kuriakose, Michael Depriester, Roch Chan Yu King, Frédérick Roussel, and Abdelhak Hadj Sahraoui *Journal of Applied Physics, 113, 044502, (2013)*

2. Improved Methods For Measuring Thermal Parameters of Liquid Samples Using Photothermal Infrared Radiometry

   Maju Kuriakose, Michael Depriester, Dorin Dadarlat and Abdelhak Hadj Sahraoui *Measurement Science and Technology, 24 (2013) 025603 (9pp)*

3. Thermal Parameters Profile Reconstruction of a Multilayered System by a Genetic Algorithm

   M. Kuriakose, M. Depriester, M. Mascot, S. Longuemart, D. Fasquelle, J. C. Carru, and A. Hadj Sahraoui. (DOI: 10.1007/s10765-013-1473-4, *International Journal of Thermophysics, 2013)*

4. The Photothermoelectric (PTE) Technique, an Alternative to Photothermal Calorimetry (To be Submitted)

   D. Dadarlat, M. Streza, **M. Kuriakose**, M. Depriester, A. H. Sahraoui

5. Maxwell Wagner Sillars effects on the thermal transport properties of Polymer dispersed liquid crystals (To be Submitted)

   M. Kuriakose, S Delenclos, M Depriester, S Longuemart and A H Sahraoui

Additional Papers

1. Dynamics of Specific Heat And Other Relaxation Processes in Supercooled Liquids by Impulsive Stimulated Scattering

   J Fivez, R Salenbien, **M Kuriakose Malayil**, W Schols and C Glorieux *(Journal of Physics: Conference Series 278 (2011) 012021)*

2. Thermal Analysis of PNIPAAm-PAAm Mixtures via Photopyroelectric Technique

   G. Akin Evingur, P. Menon, R. Rajesh, **M. Kuriakose** and C. Glorieux *(Journal of Physics: Conference Series 214 (2010) 012034)*

Dedicated to My Family and My Church

Contents

Acknowledgement i

Abstract 1

Introduction 7

1 Photothermal Techniques:- An Overview 11

1.1 Photothermal phenomena 11

1.2 Contact Photothermal Techniques 13

1.2.1 Photopyroelectric Technique (PPE) 14

1.2.2 Piezoelectric detection 15

1.2.3 Photothermoelectric Technique (PTE) 15

1.3 Non-Contact Photothermal Techniques 16

1.3.1 Photoacoustic Spectroscopy (PA) 16

1.3.2 Photothermal Beam Deflection (PBD) 17

1.3.3 Impulsive Stimulated Scattering 17

1.3.4 Photothermal Radiometry (PTR) 19

1.4 Summary 19

2 Theory of Heat Transfer Through Multi-layered Systems 20

2.1 Heat transfer through multi layered Systems 21

2.1.1 Heat Diffusion Equation 21

2.1.2 Solution of 1-Dimensional Heat Diffusion Equation for Periodically Varying Temperature Field 24

2.1.3 Temperature Field for Different Layers 25

2.2 Special Cases and Approximations 28

2.2.1 Optically Opaque Sample (A Surface Absorption Model) 28
2.3 Summary 30

3 Polarisation Field Effects on Heat Transport in PDLCs- Investigations Using Improved Photothermal Radiometry Techniques 31
3.1 Photothermal Infrared Radiometry (PTR) 32
3.1.1 Thermal Parameters from Radiometry signals 33
3.1.2 Measuring Liquid Samples Using Photothermal Radiometry (A Novel Approach) 33
3.1.2.1 Back-Front PTR (BF-PTR) :- For Finding Absolute Thermal Diffusivity 34
3.1.2.2 Back PTR (B-PTR) :- For Simultaneous Detection of Diffusivity and Effusivity 37
3.1.2.3 Front-PTR (F-PTR) 39
3.1.3 Photothermal Radiometry Experimental Set Up 41
3.1.3.1 From Laser Excitation to Infrared Detection 41
3.1.3.2 Electronic Circuitry and Signal Recording 42
3.1.3.3 Temperature Controlling 43
3.1.3.4 Electric Field Varying Experiments 43
3.1.3.5 Cell for Liquid Samples 44
3.2 Validation of PTR Methods for Liquids 45
3.2.1 Results obtained with BF-PTR configuration 46
3.2.1.1 BF-PTR experiment with water 46
3.2.1.2 BF-PTR experiment on 5CB with varying electric field . . 48
3.2.2 Results obtained with B-PTR configuration 50
3.2.2.1 B-PTR experiment on glycerol 50
3.2.2.2 B-PTR experiment on 5CB with varying electric field . . . 54
3.2.2.3 B-PTR experiment on 5CB with varying temperature . . . 54
3.2.3 Results obtained Using F-PTR configuration 56
3.2.4 Plausibility of PTR Methods for Characterizing Liquid Sample's Thermally 58
3.3 PDLC Results 58

3.3.1 Maxwell-Wagner-Sillars Effect 60
3.3.2 Thermophysical, Electrical and Dielectric Properties 62
3.3.3 Chemical Synthesis 62
3.3.4 PDLC Under Varying Electric Field 63
3.3.4.1 Effective Medium Theory and Interfacial Thermal Resistance: 66
3.3.5 PDLC Under Frequency Varying Electric Field 68
3.3.5.1 Experimental Results on PDLCs as function of Frequency 68
3.3.5.2 Effective Thermal Conductivity of LC Droplets 69
3.3.5.3 Frequency Dependent Thermal Conductivity and MWS Effect 73
3.4 Summary of the Experimental Results on Liquid Samples 77

4 Thermal Characterization of Thermoelectric Polymer-Nano Composites using A Novel Photothermoelectric (PTE) Technique 78
4.1 Introduction 78
4.2 A Novel PhotoThermoElectric Technique (PTE) 79
4.2.1 Simulations on Convection Effects and Sensitivity 81
4.2.2 Experimental Results using PTE technique 82
4.2.2.1 Intrinsically Conducting Polymers 82
4.2.2.2 Sample Preparation 84
4.2.2.3 Experimental Details 85
4.2.2.4 Results and Discussion 86
4.3 Photothermal Radiometry Experiments as a Validation for PTE Results . 88
4.3.0.5 Thermal Properties of PANI-CNT nanohybrids using PTR technique 89
4.4 Results and Discussions on Thermoelectric Properties of PANI-CNT nanohybrids 91
4.4.0.6 Summary of the results on PANI-CNT samples 94
4.5 PTE Technique for Thermal Investigation of Solids samples 95
4.5.1 Front Photothermoelectric Configuration (FPTE) 95
4.5.2 Back Photothermoelectric Configuration (BPTE) 97
4.5.3 Comparison with PPE 98
4.5.4 Mathematical simulations 98

4.5.5 Experiments on Solid Samples Using PTE technique 99
4.5.5.1 Experimental Results 101
4.5.5.2 Summary of PTE Experimental Results on Solid Samples 105
4.6 Summary 106

General Conclusions and Future Outlook **108**

Appendix **113**

Bibliography **115**

Abstract

Investigations on thermal transport properties of heterogeneous substances with existing and newly developed techniques are described in this manuscript. Primarily, we present newly developed, high sensitive and accurate methods for thermal characterization of liquids using photothermal radiometry (PTR). A three layer thermal configuration in which the sample liquid at the centre of transparent top and bottom layers serve as the sample container. Absorbing coatings at each inner surfaces (in contact with the sample) of both the top and bottom windows absorb the exciting laser radiation and acts as the point of heat generation. Moreover, the top window used for the experiments (made of CaF_2) is transparent to infrared signals generated at the CaF_2-sample boundary. In this type of configuration, the sample can be heated from the top as well as from bottom. We propose two configurations so called back-PTR (B-PTR), in which the heating for sample and reference scans are from the back side, and back-front-PTR (BF-PTR) for which front and back laser heatings for the sample are being utilized. B-PTR gives any two of the thermal parameters simultaneously (thermal diffusivity and effusivity or conductivity) and needs replacement of the sample liquid with a known reference liquid while BF-PTR provides absolute thermal diffusivity of the sample under investigation without using a separate reference liquid. Our experimental results show that the uncertainty in measured thermal parameters, thermal diffusivity, effusivity and conductivity, are in the same order of magnitude as existing contact photothermal measuring techniques with an additional advantage of non-contact capability. B-PTR and BF-PTR methods are used to study polymer dispersed liquid crystal samples.

Polymer dispersed liquid crystal (PDLC) samples of polystyrene (PS) - 5CB (4-Cyano-4′-pentylbiphenyl) are prepared by solvent induced phase separation methods. The samples are prepared for two different weight ratios of 5CB:PS (85:15 and 73:27). Both samples are analysed under polarizing microscope and calculated approximate liquid crystal (LC)

droplet sizes inside PS matrix. Dynamic thermal properties of both samples are analysed versus amplitude varying applied electric field (EF) with constant frequency as well as versus frequency varying electric field with constant amplitude. For amplitude varying experiments, we find the thermal properties are increased from an initial value to a maximum until a threshold field is reached and stay unaltered with further increase in the amplitude of the applied EF. The changes are attributed to the effect of EF on aligning the liquid crystal director in the direction of the EF. Using effective medium theory, we deduce the kapitza resistance at the LC droplet- PS matrix boundaries. These results are also used to calculate reorientation angle (θ) of the liquid crystal droplets. Investigation on thermal parameters of PDLC samples under frequency dependent EF with constant threshold amplitude corresponding to the saturation point of increase in thermal parameters (found from the amplitude varying studies) are used to analyse depolarization field effects called as Maxwell-Wagner-Sillars (MWS) effect. Our results clearly show the thermal properties of the samples are prone to depolarizing field effects at the lower frequencies of the applied EF. The experimental results are modelled against existing theories to predict electric properties of the sample composites. We have also deduced the droplet elastic constant (K). As obtained values for K are slightly lower than the reported bulk values of 5CB.

Second part of the manuscript describes the development of a novel photothermal technique based on thermoelectric (TE) effect. This technique, so called photothermoelectric (PTE), is particularly useful for thermally characterizing thermoelectric materials without using a separate sensor for measuring induced temperature changes. PTE technique is presented both theoretically and experimentally. The experiments are done on polyaniline (PANI) - carbon nanotube (CNT) composite pellets by measuring Seebeck voltage generated by the samples upon heating by a modulated laser beam alike other photothermal experiments using a lock-in amplifier. Additional PTR experiments are done on the same samples and the results are in good agreement with the one found by PTE technique. Later on, the chapter experimentally describes the possibility of PTE technique to be used for finding thermal transport properties of materials by using TE materials as photothermal sensors with known thermal properties. Two methods have been developed to find thermal effusivity and diffusivity of samples under investigation. In the first method, so called front-PTE, the TE sensor in contact with the sample via a coupling liquid having known thermal parameters, is irradiated with a chosen chopping frequency of the laser beam and

the signal is recorded as a function of the thickness of coupling fluid by implementing thermal wave resonant cavity (TWRC) procedure. This method is used to find sample's thermal effusivity. In the second case, so called back-PTE, the sample is irradiated directly using a modulated laser beam and photothermal signals from TE sensor which is in contact with the sample as a function of chopping frequency of the laser beam is analysed to find sample's thermal diffusivity. The validation measurements are performed by choosing material samples having known thermal parameters while covering wider range of typical parameter values.

Résumé

Les investigations des propriétés du transport thermique dans les substances hétérogènes avec des techniques existantes ou nouvellement développées sont décrites dans ce mémoire de thèse. Dans une première partie, une nouvelle méthode, précise et hautement sensible de caractérisation des paramètres thermiques de liquides par radiométrie photothermique (PTR) est présentée. Une configuration à 3 couches où l'échantillon liquide est emprisonné entre 2 fenêtres transparentes est proposée. Des dépôts opaques appliqués sur la surface des milieux transparents à l'interface fenêtre-liquide absorbent le faisceau laser et permettent la génération de chaleur. De plus, la fenêtre avant (en CaF2) est transparente aux radiations infrarouges émises à son interface avec l'échantillon. Dans ce type de configuration, l'échantillon peut être chauffé aussi bien par le dessus que par le dessous. Nous proposons 2 configurations. La première s'appelle la ≪ configuration arrière ≫ (B-PTR) dans laquelle la perturbation de l'échantillon et du matériau de référence s'effectuent par la face arrière et la seconde est nommée la ≪ configuration avant-arrière ≫ (BF-PTR) où les faces avant et arrière de l'échantillon sont successivement chauffées. La B-PTR donne deux paramètres thermiques simultanément (diffusivité et effusivité ou conductivité thermiques) et nécessite le remplacement de l'échantillon liquide par un liquide de référence tandis que la BF-PTR fournit la diffusivité thermique absolue sans requérir à un quelconque liquide de référence. Nos résultats expérimentaux montrent que les incertitudes sur les paramètres thermiques sont similaires aux techniques photothermiques classiquement utilisées pour les liquides avec ici l'avantage d'offrir une mesure sans contact. Par la suite, ces 2 configurations ont été utilisées pour l'étude de polymères dispersés dans des cristaux liquides (PDLC).

Des échantillons de polystyrène (PS)- 5 CB (4-Cyano-4'-pentyl-biphenyle) ont été préparés par mélange de ces éléments avec un solvant, suivi d'une évaporation de ce dernier. Deux échantillons de 5CB/PS aux fractions massiques différentes ont été préparés (85/15 % et 73/27 %). Chaque échantillon a été observé aux microscopes polarisants

et la taille des gouttelettes dans la matrice PS a été évaluée. Les propriétés thermiques dynamiques de chaque échantillon ont été mesurées en fonction de l'amplitude du champ électrique appliqué à une fréquence constante aussi bien qu'en fonction de la fréquence du champ électrique à une amplitude fixe. Pour les expériences où l'amplitude du champ électrique est la variable, nous trouvâmes que la valeur des paramètres thermiques s'accroît jusqu'à atteindre une limite qui ne peut être dépassée par tout accroissement additionnel du champ. Ces changements sont attribués à l'alignement des directeurs des cristaux liquides dans la direction du champ électrique. Par l'utilisation de la théorie des milieux effectifs, nous déduisîmes la résistance de Kapitza aux interfaces gouttelette - matrice. Ces résultats ont alors été utilisés pour calculer l'angle de réorientation (θ) des gouttes de cristaux liquides. Les analyses sur les paramètres thermiques d'échantillons PDLC en fonction de la fréquence du champ électrique, pour une amplitude fixée correspondant à la valeur de saturation des paramètres thermiques, sont utilisées pour analyser les effets du champ de dépolarisation appelé effet Maxwell-Wagner-Sillars (MWS). Nos résultats montrent clairement que les propriétés thermiques sont sujettes aux effets du champ de dépolarisation aux basses fréquences. Les résultats expérimentaux sont modélisés selon les théories prédisant les propriétés électriques des composites. Nous en avons également déduit la constante élastique des gouttelettes (K) qui se trouve être plus faible que celle reportée dans la littérature pour le 5 CB pur.

La seconde partie de ce manuscrit décrit la nouvelle technique photothermique basée sur l'effet thermoélectrique (TE). Cette technique également appelée photothermoélectricité (PTE) est particulièrement utile pour caractériser thermiquement les matériaux thermoélectriques sans avoir à recourir à un capteur extérieur pour mesurer le changement de température. Cette technique est présentée à la fois théoriquement et expérimentalement. Ces expériences sont réalisées avec des composites polyaniline/nanotubes de carbone (PANI/NTC) par mesure de la tension Seebeck générée par l'échantillon thermoélectrique chauffé par un faisceau laser. Des mesures additionnelles à l'aide de la PTR sur ces mêmes échantillons ont été réalisées et les résultats sont en bon accord avec ceux trouvés avec la PTE. Plus loin, ce chapitre évoque la possibilité d'utiliser les matériaux thermoélectriques comme capteur photothermique (aux caractéristiques thermiques connues) pour mesurer les paramètres thermiques via deux approches. Pour la première méthode, appelée PTE $\ll$ avant $\gg$, le capteur TE, en contact avec l'échantillon par l'intermédiaire d'un fluide

de couplage aux paramètres thermiques connus, est illuminé avec un faisceau laser à une fréquence de modulation adéquatement choisie et le signal est enregistré en fonction de l'épaisseur du fluide de couplage par l'implémentation d'une cavité résonnante à ondes thermiques (TWRC). Cette méthode est utilisée pour obtenir l'effusivité thermique de l'échantillon. Dans la seconde méthode appelée PTE $\ll$ arrière $\gg$, l'échantillon est irradié directement par le faisceau laser et le signal photothermique provenant du capteur TE est analysé afin d'en extraire la diffusivité thermique de l'échantillon. La validation des méthodes a été réalisée en sélectionnant des matériaux aux paramètres connus.

Introduction

In the ever extending fields of research, studies on thermal transport properties of materials are significant in many technological areas such as electronics [1], energy [2, 3], safety [4], heat exchangers [5, 6], health [7, 8] etc. As the technology grows, the ever shrinking sizes and increasing performance of instruments are always raising questions about thermal management and heat dissipation [9, 10]. Since heat is one of the unwanted by-product of almost all energy conversion processes, there is a huge interest to reduce the wastage of energy as heat as well as to remove heat effectively from the point of generation, in order to protect the device from over heating and thereby preventing system failure. The leap from micro to nano scale designing are also facing challenges on the successful implementation of the techniques. At nano scale, the physical behaviour of materials changes abruptly than while considering its properties in the bulk state. The factors like: grain boundary effects [11], inter facial thermal resistance [12, 13], surface roughness effects etc. are dominant at low dimensions. These effects may produce anomalous behaviour such as: changes in different phonon modes [14, 15], thermal conductivity [11, 16], phonon mean free path [17], refractive index [15] and so forth in the physical properties of materials [18].

As part of this PhD work, we investigate thermal transport properties of two different classes of technologically important material composites by studying them while considering all possible and aforementioned thermophysical behaviour of materials and keeping their design aspects in mind. In these, the first class contains polymer dispersed liquid crystal samples (PDLC) and the second deals with polymer thermo-electic (TE) composites. Both of these classes of material samples have been studied [19, 20, 21, 22] and being investigated in our laboratory by many researchers to understand their physical and chemical properties. So our present work is an extension to give more insight into the thermophysical properties of these materials.

Polymer dispersed liquid crystals have been attracted the scientists and manufactures

because of its many advantages over conventional liquid crystal (LC) displays. Manufacturing easiness, cost effectiveness and extended working conditions are some of its advantages. Electro-optic and thermo-dynamic behaviours of PDLCs were widely studied because of its direct application on practical implementations. So far, to the best of our knowledge, no studies were reported on PDLC's thermal behaviour other than the one reported from our lab [23].

On a fundamental point of view, PDLCs are heterogeneous mixtures and the transport properties are dependent on their constituent ratios, LC droplet size and shape, applied electric or magnetic fields, temperature, time and so on. Since these systems are more vulnerable and very sensitive to such process parameters, PDLCs are inherently more complex and often difficult to predict their behaviour without having a sound understanding versus different precess conditions.

Most often, since the PDLCs are operated by applied electric fields, their dielectric properties are also playing an important role in its working. Because of the system's heterogeneity, the difference in dielectric parameters lead to the manifestation of polarization field effects which is generally called as Maxwell-Wagner-Sillars (MWS) effect. Different electro-optical studies were reported on MWS effects in PDLCs but, until now, to the best of our knowledge, no electro-thermal studies are reported on MWS effects in PDLCs. Thus we investigate on the thermal and electro-thermal behaviours of PDLCs to study MWS effects on their thermal transport properties.

As part of the thermal investigation on PDLCs, we have developed high sensitive and accurate methods for liquid samples using photothermal radiometry (PTR) technique. These novel PTR methods principally have the capability to probe dynamic thermal transport properties like thermal diffusivity, effusivity and conductivity of liquid samples under investigation with enough resolution like other contact photothermal techniques. Since PTR is a non-contact technique, the newly developed methods are particularly suitable for electric field varying studies. In contact photothermal techniques, like photopyro electric (PPE) technique, the application of external electric field can produce extra noises and thus the experimental procedures are more difficult and tricky to obtain electrical signals from pyro sensors which are free from electric field interferences used to reorient the sample.

Chapter 2 gives the underlying theory of heat transfer through layered systems with special cases which can directly apply to analyse signals obtained from the used photothermal

experimental techniques. Chapter 3 presents the theoretical as well as the experimental aspects of novel PTR methods for liquids and the studies on PDLCs.

The second part of this manuscript deals with polymer thermoelectric materials and their thermal studies. The energy consumption [24] and thus the loss of energy, particularly in the form of heat, are increased in this modern era. Since the efficiency stays roughly less than 50% for most of the energy conversion systems (eg. automotive engines [25]), the necessity to improve performance is a major concern for the entire world. This is not only due to the scarcity and running out of the energy sources but also because of its contribution towards the global warming[26]. These threats lead researchers to perform studies on improving the efficiency of various energy converters [27, 28] and waste heat energy recovery [29, 30] possibilities.

Recently, the research on heat energy to electricity converters, which are called as thermoelectric generators (TEG), are more intensified. Thermoelectric energy harvesting could be an additional solution for the energy crisis in the near future. Since these materials are solid state converters, electricity is generated without any mechanical movements, their developments are much promising. Though various kinds of semi conducting or metallic TEGs are already available in the market, their wide applications are restricted due to the insufficient efficiency. So the researchers are working by relying on various theoretical concepts in order to develop high efficiency TEGs.

Polymer TE materials are also introduced after the findings of electrically conducting polymers. Until now, these materials are showing lower efficiencies than metallic or semiconducting TEGs. But these materials are potentially interesting because of their low cost, easiness in processing, light weight and flexibility.

Thermal properties of TEGs are involved in controlling material's energy conversion efficiency. Usually the classical thermal characterization methods like 3ω, photothermal techniques, hotwire methods etc. have been using to find their thermal properties. Since all these measurement techniques use a separate sensor, the results are prone to be erroneous due to factors such as deviations in sensor's thermal properties, interface thermal resistance of sample-sensor assembly in contact methods etc.

In order to overcome such errors and to carry out measurements in a much more reliable way, we introduce a novel thermal characterization technique for TE samples in which the TE sample itself serves as the sensor. Here the seebeck voltage generated by TE materials

upon absorbing an intensity modulated laser beam is used to find the thermal parameters of the irradiated TE sample. We present the thermal transport studies on certain polymer nanotube composite TE materials by this newly developed method, so called Photothermoelectric (PTE) technique, and validates the obtained results using classical PTR technique. Further, we present the use of PTE technique for the thermal characterization of solid and liquid samples while using TE materials as sensors as if pyro materials in PPE technique. Chapter 4 contains the developments, validation and application of novel PTE technique. It particularly compares the results from a set of polyaniline-carbon nanotube composites. These are prepared in a special chemical method in which the polymer is wrapped around nanotubes by in-situation polymerization process. The chapter ends by opening the potential use of TE sensors as photothermal sensors to characterize solid and liquid samples by presenting various experimental results.

Chapter 1

Photothermal Techniques:- An Overview

The studies on thermal transport properties of materials have extensive applications in diverse areas. Knowledge of thermal properties of materials give one to optimize the usage where he/she can find applications. In high functioning materials, for example electrically insulated and heat conducting coatings on copper windings in power transformers, a better knowledge of thermal properties of the coating material and the heat transfer at coating-substrate interfaces are important; since these properties are vital for the lifetime and functionality of transformers. On the other hand, by knowing the thermal properties, we can find the thickness of the coating layer on a substrate with high accuracy (inverse problem). Photothermal spectroscopy with a handful of flexible and accurate measuring methods give us the possibility of measuring thermal properties of matter in a non-destructive manner. This chapter gives an introduction about various photothermal methods.

1.1 Photothermal phenomena

The discovery of photoacoustic effect by Alexander Graham Bell in the nineteenth century was originally pioneered the field of thermal investigation of materials in an optically activated means. Bell's invention was first reported in 1880 of his work on the photophone (fig.1.1). Later he demonstrated that the strength of the acoustic signal strongly depends on the amount of incident light absorbed by the material in the cell [31]. Nevertheless, the

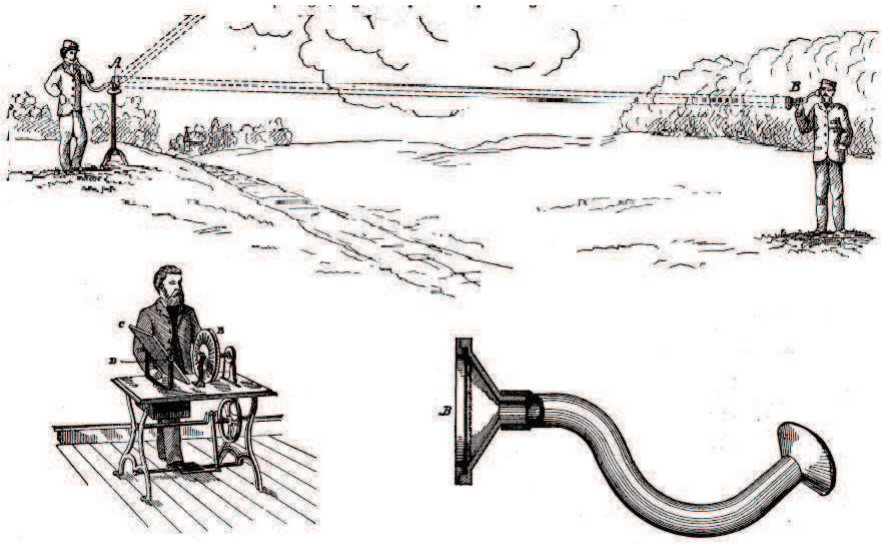

Figure 1.1: Bell's photophone and related experiments for sound transmission and reproduction by the aid of sunlight [31].

difficulty in quantifying the phenomenon, which was mainly due to the lack of detection mechanism (the investigator's ear was the detector), obstructed further developments until 1970s. Eventually after the findings of some measuring techniques, revived the research on photoacoustic effect and gave a rebirth to the field.

The word *'photothermal'* represents the process of absorption of photons in a material which accounts for the generation of heat and thus a temperature increase. This process gives rise to a number of physical phenomena including refractive index change (thermo refluctance) [32, 33], acoustic wave generation (thermoelastic effect) [34, 35], pyroelectric effect [36], infrared emission in a material sample under study. The common choice of the source for thermal excitation is a laser source with power ranging from micro watts to a few watts.

Figure (1.2) shows some of these signals generated inside a sample after the thermal excitation. More over, all of these following phenomena are material dependent and thus by measuring these physical changes may reveal us the thermal properties of material under investigation.

In the photothermal field, the existing techniques can be classified into two categories: contact and non-contact techniques. In contact techniques, a temperature or heat flux measuring sensor is placed in contact with a material sample, detects directly the thermal

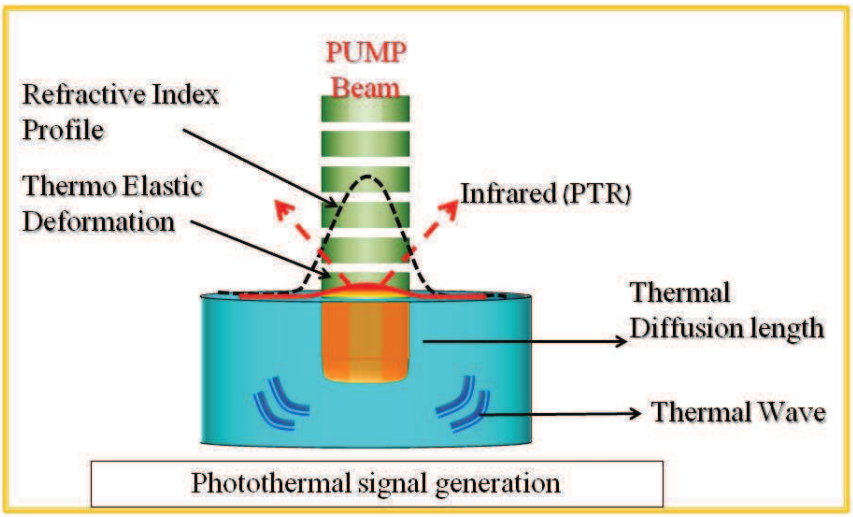

Figure 1.2: Photothermal signals generated by the thermal excitation on a sample material

variations in the sample (e.g., photopyroelectric spectroscopy). On the other hand, in non-contact techniques, the measurement is remote and thus, an induced temperature variation can be measured from various following physical phenomena like pressure variation (e.g., a photoacoustic cell detects the pressure variations in the surrounding air medium in contact with the sample due to the periodic heating), infrared emission (photothermal radiometry), refractive index changes (photothermal beam deflection) etc. which can be observed in and around a material sample upon thermal excitation. Some of these widely used techniques are described in this chapter under the classes of contact or non-contact photothermal techniques.

1.2 Contact Photothermal Techniques

Generally, contact techniques directly measures the dynamic temperature variations of a sample due to the periodical heating. Since it needs direct contact, any of them (the sample or the sensor), must have the property of sticking together without making any void space or air gap in between. So the applications are limited but can be overcome by the

help of suitable coupling fluids.

Photopyroelectric (PPE) technique is one of the well established contact photothermal technique based on pyroelectric properties of some materials. Because of its high accuracy and sensitivity PPE has been used widely. Another kind of similar technique uses piezoelectric materials instead of pyros for as sensors. Some other techniques in this category, but not based on photothermal effect, are transient hot wire (THW) methods [37, 38, 39] and 3ω techniques [40]. Here we are restricting our reviews only on techniques based on photothermal effect.

1.2.1 Photopyroelectric Technique (PPE)

Pyroelectric effect is based on the ability of a material to generate temporary voltage due to a change in heat flux through the material. The variation of temperature in the material produces a change in material's electrical polarization, which results in charge generation. In photopyroelectric technique (PPE), a modulated light source provides necessary temperature oscillations inside the sensor, directly or through the sample which is in contact with the sensor generate electrical signals. As generated photothermal signals contain both the thermal and optical properties of the sample-sensor assembly. Analysing these obtained signals with suitable theoretical model reveal the thermal properties of sample materials [41, 42, 43]. PPE techniques can be used to characterize solids [44], liquids [45] and gases [46]. The advantages of high sensitivity, large bandwidth (typically milli Hz to several kHz of dynamic response), high signal to noise ratio and simplicity to implement [36, 47] have attracted the researchers significantly to use PPE techniques widely.

Common pyroelectric sensors used to carry out PPE measurements are polyvinylidene difluoride (PVDF or PVF2) and $LiTaO_3$ single crystals. Normally, the pyro slabs are cut so that the permanent polarization fields are oriented in orthogonal direction with respect to the transducer surface. These polarization charges are coupled with the conducting electrode coatings on each surface of the transducer. When a temperature fluctuation comes, the thermal equilibrium looses and thereby a spontaneous polarization builds up. It produces the charge imbalance and opens the way to flow charges through the connected external circuitry. This charge flow in relation with the temperature fluctuations can be

written as:

$$q(t) = \frac{pA}{l_p}\int_0^{l_p} T(z,t)dz = pA\overline{T}(t) \tag{1.1}$$

where,

$t \Rightarrow$ time

$z \Rightarrow$ arbitrary direction

$l_p \Rightarrow$ thickness of pyro sensor

$A \Rightarrow$ area of the sensor

$T(z,t) \Rightarrow$ temperature

$p \Rightarrow$ pyroelectric coefficient

$\overline{T}(t) \Rightarrow$ spacially averaged temperature

Using eq. (1.1) we can find out the temperature fields of a sample-sensor stacked system and it gives the thermal properties of the sample.

1.2.2 Piezoelectric detection

An alternative technique in the photothermal field is based on the piezoelectric properties of certain materials used as sensors (such as a lead zirconate titanate (PZT) ceramic), to find thermal properties of samples [48, 49, 50]. Temperature fluctuations produce a usual spatially averaged thermal expansion on both surfaces and also a thermal decay along the thickness of the sample causes expansion of the front surface than the rear. The latter results in bending of the sample proportional to the average thermal gradient inside the sample. The net expansion on the sample surface caused by these two mechanisms produce a voltage between the two ends of the PZT sensor, which is in contact with the sample and thus the thermal properties can be found from these piezoelectric signals.

1.2.3 Photothermoelectric Technique (PTE)

This novel PT technique introduced as part of this thesis work [51] which is based on the Seebeck effect of certain materials (A property which produce electrical potential difference between the ends when it is subjected to a temperature difference between the same ends). The sensors are made of thermoelectric materials and this new method can be used efficiently to find thermal transport properties of thermoelectric materials directly by considering the sample itself as sensor. PTE technique is also capable of characterizing materials thermally in a similar manner as PPE works. The temperature dependent potential difference from the sensor is given by:

$$\Delta V = S \int_{T_{z=l}}^{T_{z=0}} dT \tag{1.2}$$

where,

$l \Rightarrow$ thickness of thermo sensor $\qquad$ $S \Rightarrow$ Seebeck Coefficient

An elaborate theoretical and experimental details are added in the later chapters of this manuscript.

1.3 Non-Contact Photothermal Techniques

Non-contact photothermal spectroscopy contains a wide variety of techniques. In these, each one of them stands out for their own distinctiveness in measuring ability or application possibility. The advantage of non-contact probing opens more applicability than the contact techniques (e.g., nano-meter thick film characterization, dealing with hazardous or highly reacting materials). Some of these widely using photothermal techniques are mentioning hereafter.

1.3.1 Photoacoustic Spectroscopy (PA)

Photoacoustic phenomena is based on the acoustic wave generation in materials due to the absorption of photons. The revival of photothermal techniques based on photoacoustic effect was experimentally and theoretically pioneered by the works of Kreuzer [52] and Rosencwaig [53]. Typically, a dedicated microphone detects the pressure variations near to a sample under light induced periodical thermal excitations. These detected signals from the microphone, contains the thermal information about the sample specimen under investigation. PA techniques have been gained a great acceptance even from its beginning and rapidly expanded [54] with successful methods to characterize different types of material samples and under different process conditions (e.g., under magnetic field). Even though the poor bandwidth, restricts the applicability of this technique. Its sensitivity and non-contact investigation possibility are major advantages.

1.3.2 Photothermal Beam Deflection (PBD)

Photothermal Beam Deflection spectroscopy based on the mirage effect, was introduced by Boccara, Fournier, and Badoz [55, 56]. A sample under periodical thermal excitation produce thermal perturbation in the gas medium in contact with the heating surface. These thermal perturbations produce a refractive index change in the medium. If a second probe beam passing in parallel to the sample surface, through the gas phase where the refractive index changes happened, can get deflected in proportion to the temperature rise in the sample specimen. These deflected probe beams, can be detected by using position-sensitive diode detectors, contain the thermal properties of the sample under investigation. Using proper theoretical models, one can find the thermal properties of the sample in relation with the detector output.

1.3.3 Impulsive Stimulated Scattering

Impulsive stimulated scattering (ISS) is a time domain experimental technique which has the advantage to measure directly the density dynamics on subnanosecond to millisecond time scales [57]. In this technique [58], an impulsive stimulated scattering of probe laser beam crossing the bulk of a (semi-) transparent sample (in transmission mode) gives the thermal as well as acoustic information about the sample. The scattering was induced by photothermal and photoacoustic excitation of the sample by a pulsed laser with pico-second pulse duration. Practically, in the case of a heterodyne type of detection, both the pump and probe laser beams are split in two diffraction orders by means of a phase mask, and recombined on the sample using a 2-lens telescope with a given magnification, which is essentially imaging the optical phase modulation induced by a phase mask with known grating space onto an equivalent light intensity pattern in the crossing region. Due to partial optical absorption of the pulsed pump laser, impulsive heating and thermal expansion occurs according to the intensity grating pattern. This launches two counter-propagating acoustic wave packets with the same spatial periodicity as the optical grating, on top of the thermal expansion grating, which is slowly washing out due to thermal diffusion between the hot (illuminated) and cold (dark) parts of the grating. The spatially periodic dynamic density changes resulting from both the thermal expansion and acoustic wave evolution results in proportional diffraction of the probe laser beams, which, by virtue

of the symmetry of the optical configuration, are automatically mixed with their reference counterparts, as depicted in fig. 1.3.

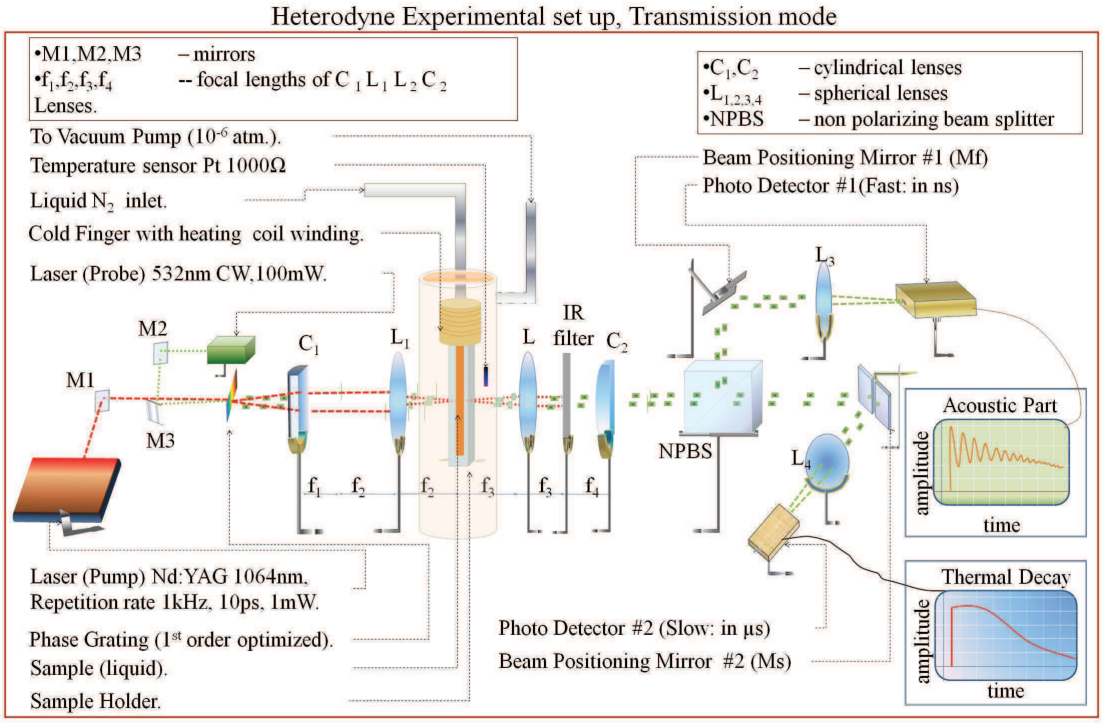

Figure 1.3: Heterodyne Detection set-up for thermal and acoustic wave propagation

This heterodyne mixing allows to optically amplify the light intensity modulation of both light beams on the photodetectors. By tuning the optical phases of these light beams by means of a glass slide or wedge in the optical path of one or both probe beams in between the lenses, the heterodyned signal components can be made opposite in sign. Differential detection of both probe beams then results in a signal in which the total heterodyne component has a double magnitude, while the dc components of the reference beams, as well as the homodyne components, are removed from the signal. It allows to find the thermal and acoustic responses of a sample. ISS by heterodyne diffraction used in such transmission configuration allows to accurately determine on one hand the longitudinal speed of acoustic waves by determining the frequency f_{signal} of the periodical part of the signal (induced by the propagating acoustic wave density grating), and calculating the corresponding acoustic velocity as cL=λf_{signal}, with λ, the spatial period of the optical grating, which can be controlled by choosing the spatial periodicity of the phase mask, and the optical magnification factor of the lens telescope. On the other hand, the decay of the

thermal expansion grating evolves exponentially according to exp(-$q^2\alpha_{th}t$), with $q=2\pi/\lambda$, the wave number of the grating, and α_{th}, the thermal diffusivity of the sample. By analyzing the periodic and decaying components of the signal ISS thus allows to simultaneously determine the longitudinal velocity and thermal diffusivity of materials [59, 60, 61].

1.3.4 Photothermal Radiometry (PTR)

Photothermal Radiometry or Photothermal Infrared Radiometry is an extensively using non-contact PT technique mainly for the thermal characterization of coating materials. The technique is based on the detection of infrared radiation, which comes out of the sample specimen due to the periodical thermal excitation by laser absorption. It posses a broad frequency response range, typically from mHz to a few MHz depending on the detection mechanism, and accuracy to find thermal properties of samples having thickness down to sub-micron scales [62]. Generally, the PTR experiments are less complex and experimental requirements can be easily fulfilled in comparison with many other non-contact techniques, e.g., PA technique needs an air tight photoacoustic cell. Since PTR is the major part of this thesis work, more details in the theoretical and experimental point of view can be found in the subsequent chapters of this manuscript.

The field of photothermal calorimetry contains a variety of experimental techniques and methods mentioned other than here. One can find a broader review on these topics from different resources [54, 63, 64, 47, 65].

1.4 Summary

In this chapter, we have given an overview of photothermal phenomena and different photothermal techniques. All the techniques have been described under two main categories: contact, and non-contact. The applicability of different techniques and the sensing mechanisms are also being described qualitatively.

Chapter 2

Theory of Heat Transfer Through Multi-layered Systems

Introduction

The fashion of adjusting a body to its surrounding temperature changes depends on its thermal properties such as: specific heat (C, the amount of heat per unit mass required to raise the temperature by one degree Celsius, unit: $\mathrm{Jkg^{-1}K^{-1}}$), Thermal Diffusivity (α, a parameter which describes how far the thermal diffusion modulation travels away from the source, unit: $\mathrm{m^2s^{-1}}$), Thermal Conductivity (κ, a parameter which describes how efficiently it conducts heat through its body, unit: $\mathrm{Wm^{-1}K^{-1}}$), Thermal Effusivity (e, square root of thermal inertia, unit: $\mathrm{JK^{-1}m^{-2}s^{-1/2}}$) etc. On the process of irradiating an opaque homogeneous isotropic sample, heat diffuses from its surface to interior, undergoes damping and phase shift. The mechanism of heat transfer also depends on the time period of irradiation (modulation frequency) and thermal properties of the surrounding media. Fourier law of heat transfer defines how the heat diffuses inside a material in the form of differential equations. Thus, by solving the heat diffusion equation with clearly defined experimental boundaries, one can quantitatively find the process of heat transfer in a material.

This chapter gives the theoretical background necessary for the investigation of thermal transport properties of various material samples studied in this thesis.

2.1 Heat transfer through multi layered Systems

Heat transfer inside a medium is basically a diffusion process rather than wave motion. A. Salazar gave a comprehensive view on classical Fourier law of heat diffusion and proposed relation between first derivative of the temporal component with the second derivatives of spatial terms which satisfies parabolic heat transfer equation, in comparison to electromagnetic wave equation which satisfies a hyperbolic relation. Nevertheless, we can assume that the heat propagation posses wave properties even though, unlike electromagnetic waves, heat waves do not carry energy i.e., the average intensity over a period is zero [66].

Heat diffusion equation governs the heat transfer through a material specimen. Let us consider an infinitesimally small volume dV of homogeneous isotropic medium in space with dimensions dx, dy and dz in the arbitrary X, Y and Z directions respectively, as in fig. (2.1). Now, when a heat flux, q_z, allowed to pass through this volume in the Z direction, can produce a change in its thermodynamic state of equilibrium if the energy is absorbed by the specimen. As gained extra energy will in turn completely stored or partly stored and dissipates the remaining, over the course of time. The complete description of such situation based on the principle of conservation of energy may include four processes: the amount of energy received into the specimen, the amount of energy generated inside the specimen, the amount of energy stored in the specimen and the amount of energy flown out of the specimen. The heat diffusion equation derives from these physical processes.
In the following section, the four previously mentioned physical processes are described mathematically in order to derive the heat diffusion equation [65, 67].

2.1.1 Heat Diffusion Equation

1. Energy Received: The entrance (or travel) of energy in the form of heat into the unit volume specimen can be: by conduction, by convection, by radiation or by the combination of either two or three of these phenomena. In our experimental conditions, it is reasonable to assume that the heat transfer is only via conduction because of the contributions via convection or radiation are negligibly smaller since the induced temperature changes are smaller than a few milli Kelvin and each measurement lasts only for a short period of time (usually upto milli seconds). Thus, the **heat flux**, q_i (where i can be x, y or z depending on the direction of heat flux), entered into a unit volume via convection in arbitrary X, Y,

and Z directions, can be expressed by the aid of Fourier's law as:

$$q_x = -k\frac{\partial T}{\partial x}\Big|_x dydz \qquad q_y = -k\frac{\partial T}{\partial y}\Big|_y dzdx \qquad q_z = -k\frac{\partial T}{\partial z}\Big|_z dxdy \tag{2.1}$$

where, κ is the proportionality constant known as thermal conductivity of the medium. The negative sign is because of the heat transfer is in the direction of decreasing temperature. The total energy received by the system from all the three directions can be expressed as,

$$E_r = q_x + q_y + q_z \tag{2.2}$$

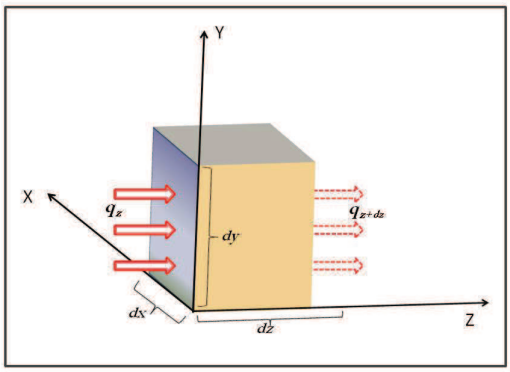

Figure 2.1: Heat transfer model

2. Energy Generated: Let us consider a periodically heating laser source having peak intensity, I_0, travelling in the z direction with angular frequency $\omega = 2\pi f$,

$$I(z) = I_0 \cos(\omega t - \psi) \tag{2.3}$$

where, f is the frequency of modulation, t is the time (sec) and ψ is the phase shift. Without loosing generality, further we can consider $\psi = 0$ and since the incident laser intensity only contribute to sample's periodical heating (and hence the generated heat wave is completely in the positive upper axis), we can rewrite the above equation as,

$$I(z) = \frac{1}{2} I_0 [1 + \cos(\omega t)] \tag{2.4}$$

and in polar form (generally the imaginary sinusoidal term can be ignored),

$$I(z) = \frac{1}{2} I_0 \left(1 + e^{i\omega t}\right) \tag{2.5}$$

The incident laser beam (photons) on materials produce thermal excitation via light absorption. This generation of heat depends on material's optical absorption coefficient (β) and the efficiency of conversion of absorbed light into heat (η) by non radiative excitation at a particular wavelength. Thus, the heat density generated at any point z because of the incident radiation can be written as:

$$E_g = \beta e^{\beta z} \eta \frac{I_0}{2} \left(1 + e^{i\omega t}\right), \qquad (z \leq 0) \tag{2.6}$$

Inverse of optical absorption coefficient is known as the optical absorption length or penetration depth (μ_β). Equation (2.6) has a frequency dependent dynamic part and also a stationary part. Apparently we are interested only in the dynamic part of E_g.

3. Energy Stored: Considering the energy received in the system completely redistributed as the kinetic energy, then the stored energy can be identified as the rate of temperature change, $\partial T/\partial t$ (T is the temperature and t is time), of the specimen and which depends on its density (ρ) and the specific heat (C). Then the stored energy can be represented as:

$$E_{st} = \rho C \frac{\partial T}{\partial t} dx\, dy\, dz \tag{2.7}$$

4. Energy flown out: The heat flux leaving the system is the space derivative of the flux entering into the volume. Tailor expansion of the heat flux over the space gives the amount of heat flux exiting the specimen and is given by, omitting the higher order terms,

$$\begin{aligned} E_f =& q_{x+dx} + q_{y+dy} + q_{z+dz} \\ =& q_x + \frac{\partial q_x}{\partial x} dx + q_y + \frac{\partial q_y}{\partial y} dy + q_z + \frac{\partial q_z}{\partial z} dx \end{aligned} \tag{2.8}$$

Combining four of these above mentioned contributions of heat energy [eqs. (2.2), (2.6), (2.7), (2.8)] in unit volume, dV, we obtain the complete picture of heat propagation in dV, which is given by:

$$E_r + E_g - E_{st} - E_f = 0 \tag{2.9}$$

which gives:

$$q_x + q_y + q_z + E_g - \left[q_x + \frac{\partial q_x}{\partial x} dx + q_y + \frac{\partial q_y}{\partial y} dy + q_z + \frac{\partial q_z}{\partial z} dx\right] - \rho C \frac{\partial T}{\partial t} dx\, dy\, dz = 0 \tag{2.10}$$

Simplifying and rearranging eq. (2.10) gives:

$$\boxed{\frac{\partial^2 T}{\partial x^2} + \frac{\partial^2 T}{\partial y^2} + \frac{\partial^2 T}{\partial z^2} + \frac{E_g}{\kappa} = \frac{\rho C}{\kappa} \frac{\partial T}{\partial t}} \tag{2.11}$$

Equation (2.11) is known as the "Heat Diffusion Equation" in three dimensions.

Dealing with the heat diffusion equation in three dimensions is more complex and needs much computational tasks. So we are only dealing with the one-dimensional form of heat propagation in all our experimental and theoretical studies. This assumption is quite valid and reasonable if the direction of heat transfer is only in one direction (say, in the Z direction) and there is no heat diffusion ($\Delta T = 0$) in the other two directions (towards X and Y directions).

2.1.2 Solution of 1-Dimensional Heat Diffusion Equation for Periodically Varying Temperature Field

One dimensional heat equation having heat propagation only in the Z direction can be written as:

$$\frac{\partial^2 T}{\partial z^2} = \frac{1}{\alpha}\frac{\partial T}{\partial t} - Q \tag{2.12}$$

where, $Q = E_g/\kappa$, is the source term and $\alpha = \kappa/\rho C$ is the thermal diffusivity. The periodically oscillating temperature field as a function of angular frequency (ω) and time (t), similar to eq. (2.5) for the oscillating intensity, can be written as, excluding the stationary part:

$$T(\omega, t) = T_0 e^{i\omega t} \tag{2.13}$$

where, T_0 is the peak value of the temperature oscillations. Equation (2.12), in the form of partial differential equation can be solved by the ***separation of variable*** method (see Appendix of this chapter).

Hence, a proposed solution for the 1-Dimensional heat transfer equation (2.12) for periodically oscillating temperature field and including the transient part of the source term (Q) explicitly, is given by:

$$T(z, t) = \left(A e^{\sigma z} + B e^{-\sigma z} - E\beta e^{\beta z}\eta \frac{I_0}{2\kappa} \right) e^{i\omega t} \tag{2.14}$$

where, A, B and E are constants which can be found by solving the equation using proper boundary conditions and σ is the complex **wave number**.

Solving eq. (A-6) for finding σ gives:

$$\sigma^2 F = i\omega \frac{F}{\alpha} \tag{2.15}$$

$$\therefore \sigma = \sqrt{\frac{i\omega}{\alpha}} = (1+i)\sqrt{\frac{\pi f}{\alpha}} \tag{2.16}$$

$$= (1+i)\frac{1}{\mu_s} \tag{2.17}$$

here, μ_s is known as the **thermal diffusion length**.

2.1.3 Temperature Field for Different Layers

In the last subsection 2.1.2, we have derived the general solution for the temperature field of a sample specimen with a heat flux flowing in the z direction. This can be extended for any number of layers. In most of our experiments, we are dealing with a system of three layers in which each of them having its own thermophysical properties.

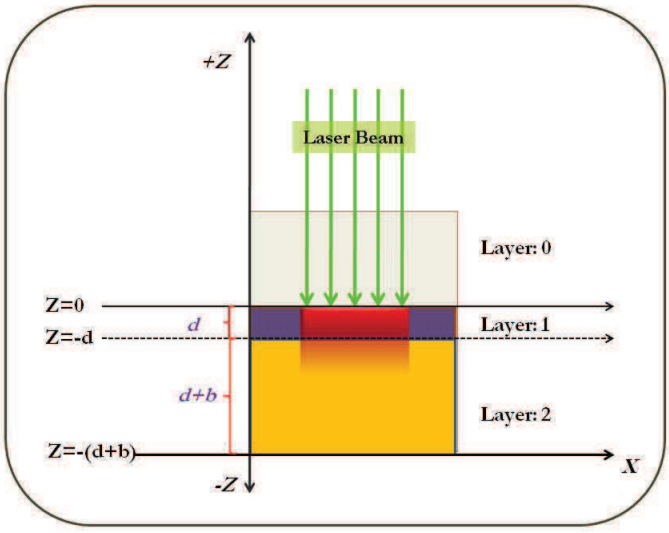

Figure 2.2: A three layer system

Figure 2.2 represents such a model of system in which a periodically modulated laser beam is allowed to fall at the top of *layer-1*, at $z = 0$, provided that the *layer-0* is transparent to the laser beam (e.g., air or quartz). The laser absorption and thereby the thermal excitation inside the sample depends on the material characteristics and which can be expressed by the eq. (2.6). Considering no laser absorption is happening in the *layer-0* and the incident laser beam is completely absorbed or blocked by the *layer-1*, then

the equations for the temperature fields T_0, T_1 and T_2 corresponding to *layer-0, layer-1* and *layer-2* respectively, can be written as:

$$T_0 = \left(A_0 e^{\sigma_0 z} + B_0 e^{-\sigma_0 z}\right) e^{i\omega t} \qquad (z \geq 0) \tag{2.18}$$

$$T_1 = \left(A_1 e^{\sigma_1 z} + B_1 e^{-\sigma_1 z} - E\beta e^{-\beta z}\eta \frac{I_0}{2\kappa_1}\right) e^{i\omega t} \qquad (0 \geq z \geq -d) \tag{2.19}$$

$$T_2 = \left(A_2 e^{\sigma_2 z} + B_2 e^{-\sigma_2 z}\right) e^{i\omega t} \qquad (z \leq -d) \tag{2.20}$$

The eq. (2.19) contains both the heat conduction part and the source term. The coefficient E in the source term is determined by forcing function and it is given by the eq. (2.24). So the constant part (*i.e.*, the term excluding $e^{\beta z}$ and $e^{i\omega t}$) of the source term (further calls by 'ϵ') is given by:

$$\epsilon = \frac{\beta \eta I_0}{2\kappa_1(\beta^2 - \sigma_1^2)} \tag{2.21}$$

By substituting eq. (2.14) in eq. (2.12) we obtain:

$$\sigma_1^2\left(T_1 + E\frac{\beta e^{\beta z}\eta I_0}{2\kappa_1}e^{i\omega t}\right) - \beta^2 E\frac{\beta e^{\beta z}\eta I_0}{2\kappa_1}e^{i\omega t} = \frac{i\omega}{\alpha_1}T_1 - \left(\frac{\beta e^{\beta z}\eta I_0}{2\kappa_1}\right)e^{i\omega t} \tag{2.22}$$

$$\sigma_1^2\left(T_1 + E\frac{E_g}{\kappa_1}\right) - \beta^2 E\frac{E_g}{\kappa_1} = \sigma_1^2 T_1 - \frac{E_g}{k_1} \tag{2.23}$$

$$\therefore E = \frac{1}{\beta^2 - \sigma_1^2} \tag{2.24}$$

Certainly the eqs. (2.18, 2.19, 2.20) have unknown coefficients and need to be solved against proper boundary conditions in order to find out its values. Before that, It is also reasonable to assume that the coefficient A_0 in eq. (2.18) is zero since the temperature at infinity is zero. Also in the same way, the coefficient B_2 in eq. (2.20) becomes zero. While looking for the boundary conditions, we can assume that the heat flux is continuous and the temperatures are same at the *layer-layer* interface. These can be written as:

$$\kappa_0\frac{\partial T_0}{\partial t} = \kappa_1\frac{\partial T_1}{\partial t}, \qquad T_0 = T_1, \qquad (z = 0) \tag{2.25}$$

$$\kappa_1\frac{\partial T_1}{\partial t} = \kappa_2\frac{\partial T_2}{\partial t}, \qquad T_1 = T_2, \qquad (z = -d) \tag{2.26}$$

Now we have three equations for the temperatures with four unknowns and four boundary conditions. Applying the boundary conditions into the eqs (2.18, 2.19) at $z = 0$ gives:

$$-b_{01}B_0 - A_1 + B_1 = -\frac{\beta}{\sigma_1}\epsilon \tag{2.27}$$

$$B_0 - A_1 - B_1 = -\epsilon \tag{2.28}$$

Similarly, by applying boundary conditions to the eqs. (2.19, 2.20) at $z = -d$ gives:

$$A_1 e^{-\sigma_1 d} - B_1 e^{\sigma_1 d} - b_{21} A_2 = \frac{\beta}{\sigma_1} \epsilon e^{-\beta d} \tag{2.29}$$

$$A_1 e^{-\sigma_1 d} + B_1 e^{\sigma_1 d} - A_2 = \epsilon e^{-\beta d} \tag{2.30}$$

Here, b_{01} and b_{21} are given by:

$$b_{01} = \frac{k_0 \sigma_0}{k_1 \sigma_1} = \frac{e_0}{e_1} \tag{2.31}$$

$$b_{21} = \frac{k_2 \sigma_2}{k_1 \sigma_1} = \frac{e_2}{e_1} \tag{2.32}$$

where, e_0, e_1 and e_2 are the thermal effusivities of *layer-0, layer-1* and *layer-2* respectively. Equations (2.28, 2.28, 2.30, 2.30) in matrix form is given by:

$$\begin{bmatrix} -b_{01} & -1 & 1 & 0 \\ 1 & -1 & -1 & 0 \\ 0 & e^{-\sigma_1 d} & -e^{\sigma_1 d} & -b_{21} \\ 0 & e^{-\sigma_1 d} & e^{\sigma_1 d} & -1 \end{bmatrix} \begin{bmatrix} B_0 \\ A_1 \\ B_1 \\ A_2 \end{bmatrix} = \begin{bmatrix} -\frac{\beta}{\sigma_1} E \\ -E \\ \frac{\beta}{\sigma_1} E e^{-\beta d} \\ E e^{-\beta d} \end{bmatrix} \tag{2.33}$$

Using Cramer's rule, one can solve the above matrix and the unknowns are given by:

$$B_0 = \epsilon \frac{\left[(1+b_{21}) e^{\sigma_1 d} \left(\frac{\beta}{\sigma_1} - 1 \right) + (1-b_{21}) e^{-\sigma_1 d} \left(\frac{\beta}{\sigma_1} + 1 \right) + 2 e^{-\beta d} \left(b_{21} - \frac{\beta}{\sigma_1} \right) \right]}{(1+b_{01})(1+b_{21}) e^{\sigma_1 d} - (1-b_{01})(1-b_{21}) e^{-\sigma_1 d}} \tag{2.34}$$

$$A_1 = \epsilon \frac{e^{\sigma_1 d} (1+b_{21}) \left(b_{01} + \frac{\beta}{\sigma_1} \right) + e^{-\beta d} (1-b_{01}) \left(b_{21} - \frac{\beta}{\sigma_1} \right)}{(1+b_{01})(1+b_{21}) e^{\sigma_1 d} - (1-b_{01})(1-b_{21}) e^{-\sigma_1 d}} \tag{2.35}$$

$$B_1 = \epsilon \frac{e^{-\beta d} (b_{01}+1) \left(b_{21} - \frac{\beta}{\sigma_1} \right) + e^{-\sigma_1 d} (1-b_{21}) \left(b_{01} + \frac{\beta}{\sigma_1} \right)}{(1+b_{01})(1+b_{21}) e^{\sigma_1 d} - (1-b_{01})(1-b_{21}) e^{-\sigma_1 d}} \tag{2.36}$$

$$A_2 = \frac{\epsilon}{\sigma_1} \frac{\left[-e^{\sigma_1 d - \beta d} (1+b_{01}) \left(\sigma_1 + \frac{\beta}{\sigma_1} \right) + e^{-\sigma_1 d - \beta d} (1-b_{01}) \left(\sigma_1 - \frac{\beta}{\sigma_1} \right) + 2\sigma_1 \left(b_{01} + \frac{\beta}{\sigma_1} \right) \right]}{(1+b_{01})(1+b_{21}) e^{\sigma_1 d} - (1-b_{01})(1-b_{21}) e^{-\sigma_1 d}} \tag{2.37}$$

Substituting these eqs. (2.34, 2.35, 2.36, 2.37) in the eqs. (2.18, 2.19, 2.20) for temperature fields give:

$$T_0 = \epsilon \frac{\left[(1+b_{21}) e^{\sigma_1 d} \left(\frac{\beta}{\sigma_1} - 1 \right) + (1-b_{21}) e^{-\sigma_1 d} \left(\frac{\beta}{\sigma_1} + 1 \right) + 2 e^{-\beta d} \left(b_{21} - \frac{\beta}{\sigma_1} \right) \right]}{(1+b_{01})(1+b_{21}) e^{\sigma_1 d} - (1-b_{01})(1-b_{21}) e^{-\sigma_1 d}} e^{-\sigma_0 z} e^{i\omega t}, \quad (z \geq 0) \tag{2.38}$$

$$T_1 = \epsilon \left[\frac{e^{\sigma_1 d} (1+b_{21}) \left(b_{01} + \frac{\beta}{\sigma_1} \right) + e^{-\beta d} (1-b_{01}) \left(b_{21} - \frac{\beta}{\sigma_1} \right)}{(1+b_{01})(1+b_{21}) e^{\sigma_1 d} - (1-b_{01})(1-b_{21}) e^{-\sigma_1 d}} e^{\sigma_1 z} + \right.$$
$$\left. \frac{e^{-\beta d} (b_{01}+1) \left(b_{21} - \frac{\beta}{\sigma_1} \right) + e^{-\sigma_1 d} (1-b_{21}) \left(b_{01} + \frac{\beta}{\sigma_1} \right)}{(1+b_{01})(1+b_{21}) e^{\sigma_1 d} - (1-b_{01})(1-b_{21}) e^{-\sigma_1 d}} e^{-\sigma_1 z} - e^{\beta z} \right] e^{i\omega t}, \qquad (0 \geq z \geq -d) \tag{2.39}$$

$$T_2 = \frac{\epsilon}{\sigma_1} \frac{\left[-e^{d(\sigma_1-\beta)}\left(1+b_{01}\right)\left(\sigma_1+\frac{\beta}{\sigma_1}\right)+e^{d(-\sigma_1-\beta)}\left(1-b_{01}\right)\left(\sigma_1-\frac{\beta}{\sigma_1}\right)+2\sigma_1\left(b_{01}+\frac{\beta}{\sigma_1}\right)\right]}{\left(1+b_{01}\right)\left(1+b_{21}\right)e^{\sigma_1 d}-\left(1-b_{01}\right)\left(1-b_{21}\right)e^{-\sigma_1 d}} e^{\sigma_2(z+d)} e^{i\omega t}, \quad (z \leq -d) \quad (2.40)$$

Equations (2.38, 2.39, 2.40) represent the complete solution in order to find the temperature fields at different depths of a three layer system. Even though all these equations seem to be lengthier and consists of many parameters, usually the case studies make it smaller and much more interesting.

2.2 Special Cases and Approximations

Thermal characterisation of materials needs different modes of experimentations depending on the sample of interest. For example, a transparent glass needs an absorbing layer for the incident laser beam while a steel sample not; a semitransparent sample allows the laser radiation upto a longer depth and thereby the point of heat generation also stretch forth, which means that the condition for volume absorption is met. The plausibility to determine the thermal parameters is also depending on the physical dimensions of the sample, because, the thermal diffusion length governs the depth upto where a thermal wave can travel. So the experimental situations can differ according to the sample's optical, physical, dimensional or thermal properties. Here we are mentioning only a few special cases that suits to our experiments. A more broader study about different special cases can be found in literatures [67, 68, 36].

2.2.1 Optically Opaque Sample (A Surface Absorption Model)

Let us consider a situation at which the intensity of the laser excitation for heat generation is attenuated by a factor of $1/e$ inside a sample layer (say, *layer-1*), then the optical absorption length ($\mu_\beta = \beta^{-1}$), inverse of the optical absorption coefficient, is smaller than the sample thickness, d, and thus the sample is optically opaque. Again, if the penetration depth, μ_β, is much lesser than the thermal diffusion length of the sample layer, then the material is optically opaque and the criterion for 'surface absorption' is also met. Thus the

condition for optically opaque sample with surface absorption is given by:

$$\mu_s \gg \mu_\beta, \qquad \text{Surface absorption}$$

$$d > \mu_\beta, \qquad \text{Optically opaque}$$

Under these conditions and at nominal experimental frequency range, it is pretty reasonable to assume that:

$$e^{-\beta d} \approx 0$$

$$\beta/\sigma_1 \pm 1 \approx \beta/\sigma_1$$

$$\beta^2 - \sigma^2 \approx \beta^2$$

The incident light to heat conversion efficiency, η, is usually considered as one. All these approximation can be applied to eqs. (2.38, 2.39, 2.40). We are mainly interested in temperature fields at the top and bottom surfaces of *layer-1*, at $z = 0$ and $z = -d$. Thus rewriting eq. (2.38) at $(z = 0)$ for *layer-1* gives:

$$T_0(\omega, z = 0) = \frac{I_0}{2\sigma_1 k_1 (1 + b_{01})} \left(\frac{1 + \Re_2 e^{-2\sigma_1 d}}{1 - \Re_0 \Re_2 e^{-2\sigma_1 d}} \right) e^{i\omega t} \tag{2.41}$$

where, $\Re_0$ and $\Re_2$ are given by:

$$\Re_0 = \frac{1 - b_{01}}{1 + b_{01}} \qquad \Re_2 = \frac{1 - b_{21}}{1 + b_{21}} \tag{2.42}$$

The quantities b_{01} and b_{21} are the ratios of effusivities of adjacent layers given by eqs. (2.31 and 2.32). It represents the thermal mismatch between the layers. While measuring single layered solid samples, the top and bottom surrounding layers are air, having a lowest effusivity of 5.7 $\mathrm{JK^{-1}m^{-2}s^{-1/2}}$ [69]. This makes the effusivity ratios become much smaller than one. Again, if it is the case of liquid samples, the top and bottom layers could be of glass or similar type of materials which will be chosen in such a way that the thermal mismatch is minimized in order to obtain highest accuracy[44, 70], resulting, b_{01} and b_{21} are much smaller in comparison to the quantity β/σ_1. So the eq. (2.39) at $(z = -d)$ can be approximated and rewritten as:

$$T_1(\omega, z = -d) = \frac{I_0 e^{-\sigma_1 d}}{2\sigma_1 k_1 (1 + b_{01})(1 + b_{21})} \left(\frac{2}{1 - \Re_0 \Re_2 e^{-2\sigma_1 d}} \right) e^{i\omega t} \tag{2.43}$$

Or in another form,

$$T_1(\omega, z = -d) = \frac{I_0}{2\sigma_1 k_1(1 + b_{01})} \left(\frac{(1 + \Re_2)\, e^{-\sigma_1 d}}{1 - \Re_0 \Re_2 e^{-2\sigma_1 d}} \right) e^{i\omega t} \tag{2.44}$$

Now the equations of temperature fields look fairly simple compared to the full equations and yet valid. Further we can neglect also the temporal term, since the experiments are conducted in frequency domain.

2.3 Summary

This chapter principally contains the necessary theoretical descriptions which suits to the chosen photothermal experiments those have been used in this thesis work. It started by deriving the heat diffusion equation and then solving it for one dimensional heat transfer for a three layer system. Later the solutions are being treated under practical circumstances by special cases and approximations, under which, theoretical models can be developed for measuring liquid and solid samples.

Chapter 3

Polarisation Field Effects on Heat Transport in PDLCs- Investigations Using Improved Photothermal Radiometry Techniques

Introduction

This chapter deals with the theoretical and experimental results obtained by photothermal radiometry (PTR) technique to measure thermal properties of liquid samples with novel approaches. The chapter primarily gives the underlying theory for analysing signals from PTR experiments and secondly, it deals with the development of two novel PTR methods which give high accuracy on results than the existing PTR methods for thermal characterization of liquids. In addition, the chapter also contains the validation experiments on thermal investigation of some common liquids as well as temperature dependent phase transition studies and electric field (EF) dependent thermal transport studies of 5CB (4-Cyano-4'-pentylbiphenyl) liquid crystal (LC).

Finally, it presents the studies on polarization field effects on the thermal properties of Polymer Dispersed Liquid Crystal (PDLC) samples using the newly developed PTR techniques. Experiments on PDLC samples have been mainly aimed for the investigation on the variation of their thermal properties as a function of frequency of the applied

electric field. Our observations are confirming this thermal dependence on frequency (of the applied electric field) due to the presence of polarization field effects, which is also known as Maxwell-Wagner-Sillars (MWS) effect. The obtained results are modelled against existing theories on MWS effect for finding the elastic and electrical properties of PDLC samples from their thermal informations.

3.1 Photothermal Infrared Radiometry (PTR)

Photothermal Infrared Radiometry[71, 68] (PTR) is an efficient and accurate non-destructive technique able to find the thermal properties of materials. As the name specifies, it uses the infrared radiation coming out of the material under investigation and gives us the advantage of investigating materials in a non contact manner. Because of the non-contact ability of PTR, it is mainly used to characterize solid materials, where the contact techniques can produce errors due to the contact resistance at the sample-sensor interface. Considering the thermal investigation capability of layered systems [72, 73, 74], thin films [75], liquids [76, 77] etc., PTR has its own space in the field of thermal characterisation of materials.

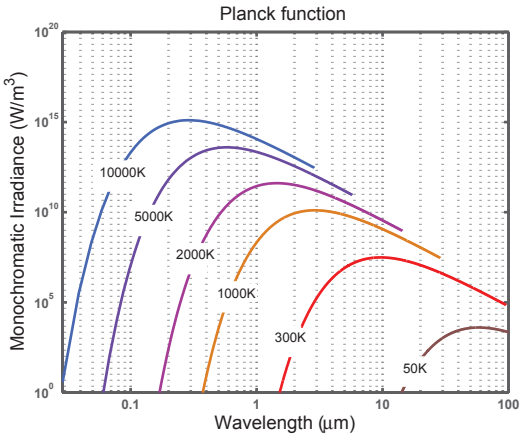

Figure 3.1: Black body radiation

According to the concept of Black body radiation, a perfect black body emits electromagnetic radiation when its temperature is above absolute zero. Planck's work gave the first indication of quantum nature of light and the atom. He derived Stefan-Boltzmann law and the Wien law which relates the temperature of a body and the wavelength of the emitted radiation. Thus black body curves are called as Planck's Curves. Even though the irradiating samples are not perfect black bodies, still we can apply the formula involved in the Planck Curves given by:

$$W(\lambda, T) = \frac{2hc^2\lambda^{-5}}{e^{\frac{hc}{\lambda k_B T}} - 1} \tag{3.1}$$

where, c is the speed of light (3×10^8m/s), h is the Planck's constant ($6.62606957 \times 10^{-34}$ Js) and k_B is the Boltzmann constant ($1.3806488 \times 10^{-23}$ JK^{-1}. λ, T are the wavelength in μm and absolute temperature in K respectively. Agreeing to the above mentioned theories of black body radiation, objects having temperature around 2000 K emit radiation with maximum intensity in the wavelength of red color. Thus, for materials at room temperature ($\sim$ 300 K), emit radiations mainly in the Infrared (IR) region of the electromagnetic wave spectrum corresponding to the ro-vibrational energy transition (see fig (3.1)).

3.1.1 Thermal Parameters from Radiometry signals

Dealing with the experimental data and retrieving back the thermal informations is an important part of thermal analysis. Usually the data consists of frequency dependent amplitude and phase measured and recorded by a lock-in amplifier represented by the complex relation:

$$\mathbb{V}(z, \omega) = \mathbb{Z}(\omega)\Gamma(z, \omega) \tag{3.2}$$

Here, $\mathbb{Z}(\omega)$ represents the instrumental transfer function and $\Gamma(z, \omega)$ contains the thermal information of the sample. Due to the difficulty in quantifying the frequency dependent instrumental transfer function, the experimental analysis needs normalization of the data obtained by dividing two separate frequency scans:

- a usual sample scan and a reference scan with different material in exactly identical experimental conditions.
- a sample scan followed by a reference scan on the same sample using different experimental configuration.

This normalised signal, free from the instrumental transfer function and contains only the thermal parameters of the sample and the reference material. By analytically solving or numerically fitting this normalised signal against proper equation(s) derived for the temperatures in the last section 2.2, unveils the thermal properties of the sample.

3.1.2 Measuring Liquid Samples Using Photothermal Radiometry (A Novel Approach)

Generally measuring liquid samples need proper holder or encapsulation because of its flowing nature. As a result it increases the experimental difficulties also. In order to reduce

the complexity of the data analysis and thereby increasing the accuracy and certainty of the measured thermal properties, a three layer system with liquid sample at the centre of two transparent semi infinite windows has been considered in this novel approach [78], as shown in the fig. 3.2. The possibility of irradiating the sample from the top, at the interface of *layer-0* and *layer-1*, as well as from the bottom, at the interface of *layer-1* and *layer-2*, has been used for these measurements.

Since the experimental signal is in the infrared (IR) region ($\lambda \sim 10\mu$m) and since the signal detection is from the top of the sample, a visible - infrared (VIR) transparent CaF_2 upper window (*layer-0*) was chosen. At the bottom, we have used visible transparent glass. Consequently a laser absorbing coating at the liquid interface side of both of the windows has been accomplished in order to completely block the laser beam at each of the sample boundaries and to provide necessary thermal excitation.

3.1.2.1 Back-Front PTR (BF-PTR) :- For Finding Absolute Thermal Diffusivity

Similar to the self normalisation procedure used to find the thermal diffusivity of solids [79], one can obtain the absolute thermal diffusivity of the liquid sample employing this configuration. Since it is a self normalisation procedure, the results posses high precision and are independent of the thermal parameters of the surrounding layers. One needs to know only the thickness of the sample accurately, to determine the thermal diffusivity and vice versa. The experimental configuration is depicted as in fig. 3.2 with back by front normalisation. In the front frequency scan, the laser heating and the signal generation are at the CaF_2-sample interface. For the back frequency scan, the laser heating is at the backing-sample interface and the signal is detected from the CaF_2-sample interface. Since the back signal propagates through the sample, it posses very high sensitivity to its thermal properties. At the same time, because of the heavily damped nature of the heat waves during its propagation towards the point of detection, we are bounded to some finite extend of the modulation frequency range, determined both by the thermal parameters of the sample and by the thickness of the sample cavity. Above this range the signal to noise ratio becomes much lower.

The normalized signal for the BF-PTR configuration is obtained by dividing eq. (2.43)

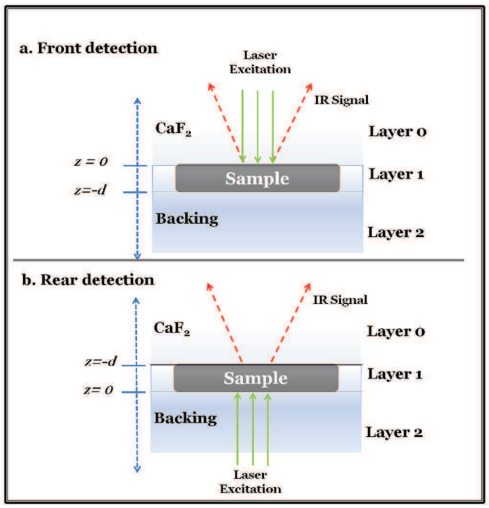

Figure 3.2: Theoretical model for liquid measurement using photothermal radiometry. (a) Front detection. (b) Rear (back) detection.

with eq. (2.41) and it can be written as:

$$\Gamma_{BF}(\omega) = \frac{T_1(\omega, z=-d)}{T_0(\omega, z=0)} = \frac{I_b 2\kappa_1\sigma_1}{I_f 2\sigma_1\kappa_1}\left(\frac{2e^{-\sigma_1 d}}{1+\Re_2 e^{-2\sigma_1 d}}\right) \tag{3.3}$$

where, I_b and I_f are the peak intensities of the laser radiation for the back and front excitation respectively. Doing further simplification one can arrive at:

$$\Gamma_{BF}(\omega) = A_f e^{-\sigma_1 d}\left(\frac{1}{1+\Re_2 e^{-2\sigma_1 d}}\right) \tag{3.4}$$

with,

$$A_f = 2\frac{I_b}{I_f(1+b_{21})}, \qquad \Re_2 = \frac{(1-b_{21})}{(1+b_{21})}, \qquad b_{21} = \frac{e_2}{e_1}$$

Further, at higher modulation frequencies, the term $\exp(-2\sigma_1 d)$ in eq. (3.4) can be approximated to zero. Thus the equation for the BF-PTR configuration can be written as:

$$\boxed{\Gamma_{BF}(\omega) = A_f e^{-\sigma_1 d}} \tag{3.5}$$

Figure 3.3(c, d) shows the percentile error in amplitude, phase and thermal diffusivity (α) from each, while using approximated model, eq. (3.5), instead of the full model, eq. (3.4), simulated with water as the sample and thickness, d=100μm. The plots show the valid frequency domain of the approximated model for conducting experiments. This domain will change according to the material properties and the sample thickness. But

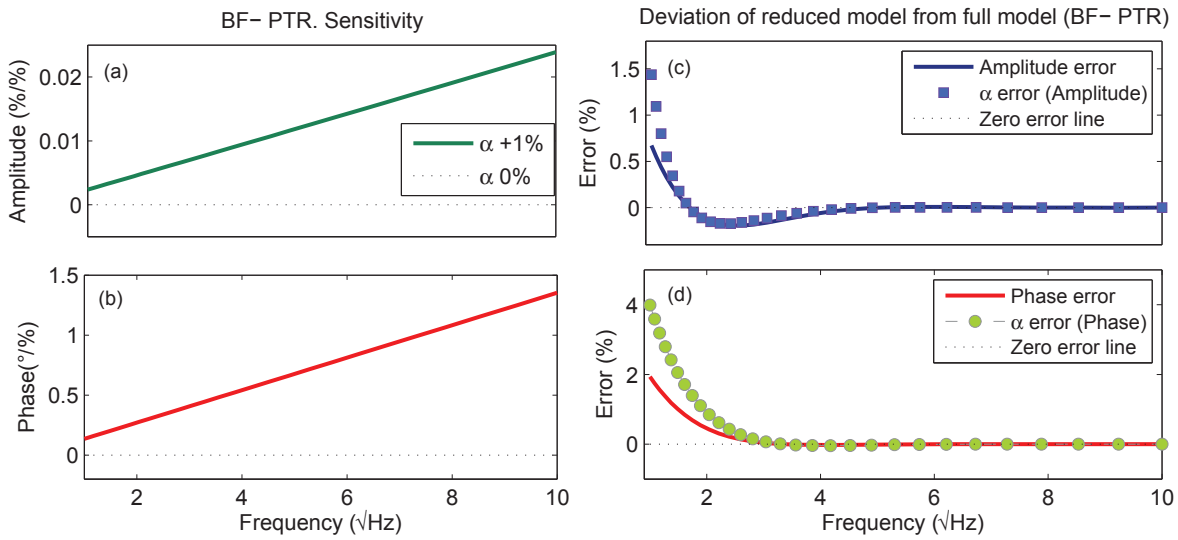

Figure 3.3: BF-PTR sensitivity plots (a and b) depicts the percentage change in sensitivity vs. square root of frequency for a 1% increase in diffusivity of sample. Plots (c) and (d) show the percentile error vs. square root of frequency in amplitude (line) and α error from amplitude (squares), phase (line) and α error from phase (circles), showing deviation of the reduced model (eq. 3.5)from full model, (3.4) in BF-PTR. Simulated with water as the sample and d =100μm.

still it is evident that the experiment can be realised in a well extended frequency domain. From eq. (3.5), we can find the absolute thermal diffusivity of the sample layer. Though the term A_f contains the effusivity of the sample and the substrate, it remains undetectable and just acts as an offset for the amplitude.

Equation (3.5) is particularly useful due to its rather direct and only exponential term to find sample's thermal diffusivity evolution as a function of time, temperature or electric field. The sensitivity to the thermal diffusivity of the sample increases with the modulation frequency as shown in fig. 3.3(a, b). So it is advisable to conduct the measurements in the high sensitive experimental region at which the sample becomes quasi thermally thick. Here, both the amplitude and phase independently carry the information about the thermal diffusivity. So relation for finding thermal diffusivity analytically is:

$$\text{from amplitude,} \qquad \alpha_1 = \pi f \left[\frac{d}{\ln\left(A_f/A\right)}\right]^2 \tag{3.6}$$

$$\text{from Phase,} \qquad \alpha_1 = \pi f \left[\frac{d}{\theta}\right]^2 \tag{3.7}$$

where, A and θ are the experimental amplitude and phase respectively. Both equations (3.7 and 3.7) reveal us that the thermal diffusivity can be calculated from any single frequency and it depends only on the thickness of the sample.

3.1.2.2 Back PTR (B-PTR) :- For Simultaneous Detection of Diffusivity and Effusivity

Alike back photopyroelectric (BPPE) technique [36, 80], the so called Back-PTR (B-PTR) configuration posses high sensitivity and allows simultaneous detection of thermal diffusivity and effusivity of the sample. As in the case of BF-PTR, here also we are bounded to some maximum range of modulation frequency. As shown in figure 3.2(b), the heat is generated at the backing-sample interface and the signal detection is from the CaF_2-Sample interface for both scans, the sample and reference scans. The normalized equation derived from eq. (2.43) is given by:

$$\Gamma_B(\omega) = \frac{T_1(\omega, z=-d)}{T_1'(\omega, z=-d)} = \frac{e_1'}{e_1}\frac{\left(1+b_{01}'\right)\left(1+b_{21}'\right)e^{\sigma_1' d}}{\left(1+b_{01}\right)\left(1+b_{21}\right)e^{\sigma_1 d}}\left[\frac{1-\Re_0'\Re_2' e^{-2\sigma_1' d}}{1-\Re_0\Re_2 e^{-2\sigma_1 d}}\right] \tag{3.8}$$

The variables with prime show the thermal parameters of the reference material and without prime represent the sample.

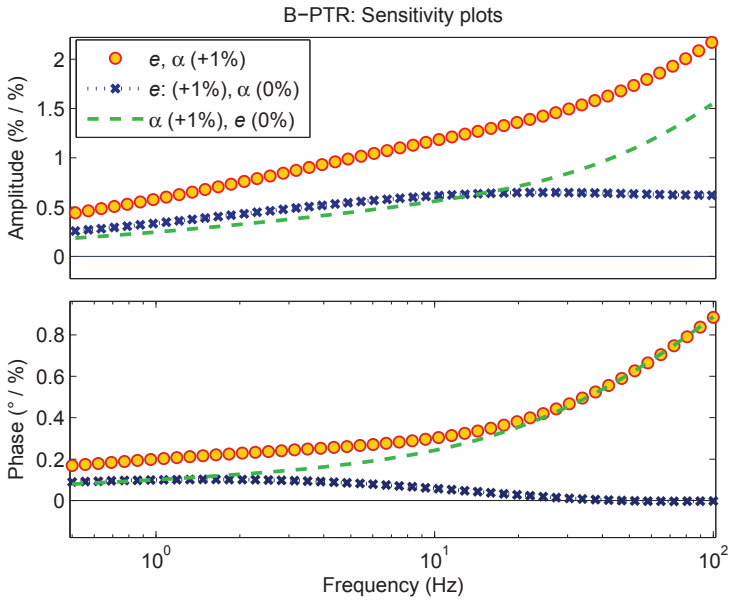

Figure 3.4: Simulated plots of frequency dependent amplitude and phase of a typical liquid sample (α_1 =1.48 $\times 10^{-7}$m^{2}s^{-1}, e_1 =650 Jm^{-2}K^{-1}s$^{-1/2}$, d= 50μm) showing the percentile change in amplitude (upper plot) and phase (lower plot) with +1% change in α_1 and e_1, (circles); +1% change in e_1 keeping 0% change in α_1 (dotted line with cross) and +1% change in α_1 keeping 0% change in e_1 (dashed line).

Figure 3.4 contains the simulations using equation (3.8) for the percentage variation of the frequency dependent normalized amplitude and phase plotted with +1% change in

Table 3.1: Thermal parameters used for simulations.

	Diffusivity (m^2s^{-1})	Effusivity ($Jm^{-2}K^{-1}s^{-1/2}$)	Conductivity ($Wm^{-1}K^{-1}$)
CaF_2	3.58×10^{-6}	5135	9.71 [a]
Quartz	8.4×10^{-7}	1590	—
Water[b]	1.43×10^{-7}	—	0.598

[a] Data sheet, Crystran Ltd. [b] Ref.[81] water at 20 ^{0}C.

thermal diffusivity and effusivity of a typical liquid sample (circles) (α_1=1.48 $\times 10^{-7} m^2 s^{-1}$, e_1 =650$Jm^{-2}K^{-1}s^{-1/2}$) having thickness, $d = 50\mu m$, sandwiched between CaF_2 top layer and bottom glass substrate (table 3.1). The dotted line with cross shows a change in thermal effusivity (e_1) by +1% keeping original diffusivity (α_1, 0%) while the dashed line represents +1% change in diffusivity and original effusivity (e_1, 0%).

The trends of these plots demonstrate that the sensitivity towards thermal diffusivity of the sample is monotonically increasing with the increase in modulation frequency for both the amplitude and phase. It is also evident that the amplitude is sensitive to the thermal effusivity in the entire frequency range while the phase is sensitive only at the lower frequency region. Apparently, for such measurements which needs a physical replacement of the sample with a reference material, a varying proportionality factor (A_f) may be needed to consider in the fitting domain in order to nullify the offset that can come in the signal amplitude because of many reasons, restricts the use of amplitude alone for finding thermal parameters. Thus, in this case, an effusivity sensitive phase data in the lower frequency region is needed to determine both of the thermal parameters from eq. (3.8).

Further more, B-PTR gives the advantage of finding thermal diffusivity and effusivity simultaneously from a single frequency for those measurements in which A_f is kept fixed (means: no physical sample-reference replacement). This is the case when the used reference material is the sample itself in a particular condition (ambient temperature, zero applied electric field etc.) where its thermal parameters are known. It helps to avoid time consuming frequency scans while preserving better accuracy. Sample's thermal diffusivity can be calculated from the phase and the effusivity from the combined amplitude and phase signals. The analytical expression for sample's thermal diffusivity, α_1, and effusivity, e_1, are

given by equations (3.9) and (3.10) respectively. Both of these equations are derived from equation (3.8) considering that the sample is at quasi thermally thick ($\mu_s \approx d$) frequency regime and thus the negative exponential term has negligible contribution ($e^{-2\sigma_1 d} \approx 0$).

$$\alpha_1 = \left(\frac{d\sqrt{\alpha_r \pi f}}{d\sqrt{\pi f} - \theta\sqrt{\alpha_r}} \right)^2 \tag{3.9}$$

$$e_1 = -\frac{1}{2}\left\{ L - R + \sqrt{(L-R)^2 - 4J} \right\} \tag{3.10}$$

where,

$$R = \frac{\exp(\theta)}{e_r A}\left(e_r^2 + e_r L + J\right) \qquad L = e_0 + e_2 \qquad J = e_0 e_2$$

A is the normalized amplitude and θ is the normalized phase. α_r and e_r are thermal diffusivity and effusivity of the reference material respectively. f represents the modulation frequency and d is the sample thickness.

3.1.2.3 Front-PTR (F-PTR)

Rather easier but less sensitive than the rear detection involved models, this, so called front-PTR configuration is depicted as in Fig. 3.2(a). The laser excitation and the signal detection are from the same side (CaF_2 face), at the interface between CaF_2 (*layer: 0*) and Sample (*layer: 1*), of the sample cell assembly for both the sample and reference scans. The temperature field at the sample surface ($z = 0$) is described by the eq. (2.41) which is obtained from the surface absorption model. To avoid the use of a second reference material and thereby minimizes errors due to possible distortions in the experimental setup due to the sample-reference replacement and also uncertainties on the reference material's thermal properties, we have carried out the reference scan with the same sample with semi infinite thickness. Hence it gives better accuracy on the results and provides the possibility of measuring the absolute values of sample thermal parameters. The equation for F-PTR model with sample of known thickness, d, normalised with same semi infinite sample is obtained from eq. (2.41) and can be written as:

$$\Gamma_F(\omega) = \frac{1 + R_2 e^{-2\sigma_1 d}}{1 - R_0 R_2 e^{-2\sigma_1 d}} \tag{3.11}$$

Figure 3.5 shows the frequency dependent procentile sensitivity variations of the normalised amplitude and phase for 5% change in thermal diffusivity and effusivity, one by

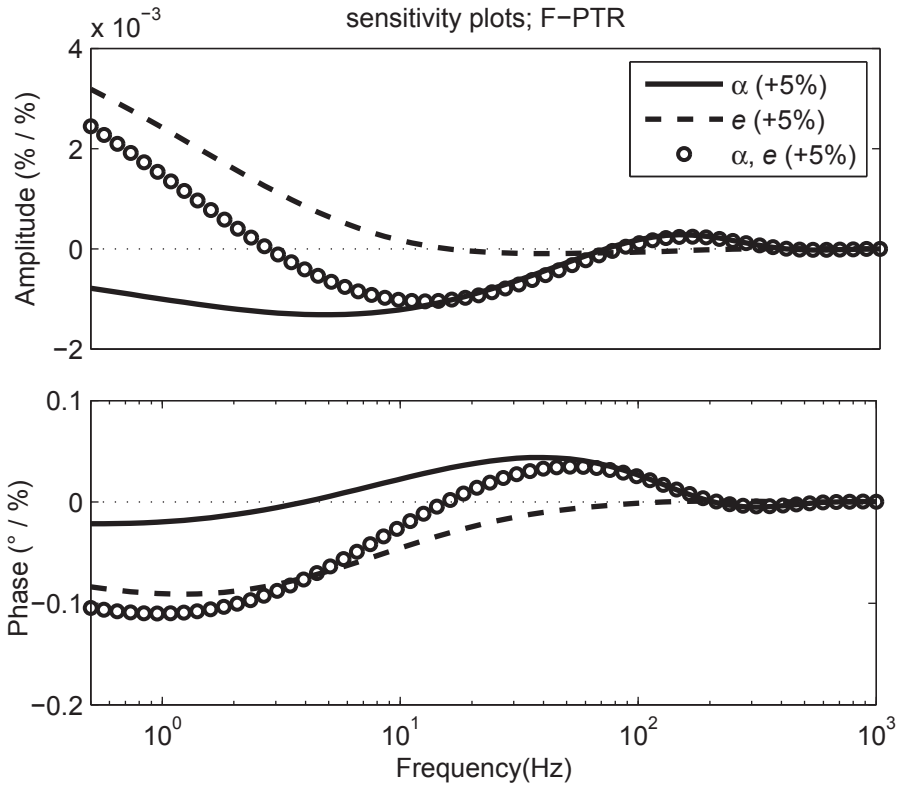

Figure 3.5: Frequency dependent sensitivity plots of the F-PTR model for the percentage change in amplitude (upper plot) and phase (lower plot) for percentage change in thermal parameters. The solid line represents a +5% change in sample thermal diffusivity without varying effusivity while the dashed line corresponds to a change of +5% in effusivity keeping diffusivity same as reference. The circles represents a change of +5% in both α and e. The simulation has been done for liquid sample with typical thermal parameters (α_1 =1.48×10^{-7} m^{2}s^{-1}, e$_1$ =650 Jm^{-2}K^{-1}s$^{-1/2}$) and d =30 μm with steel as backing and CaF_2 as the top layer. The normalisation has been done with the same sample while making it semi infinite.

one and together, for a typical liquid sample having distinctive values of thermal parameters (α_1 =1.48×10^{-7} m^{2}s^{-1}, e$_1$ =650 Jm^{-2}K^{-1}s$^{-1/2}$). The sample is sandwiched between a CaF_2 window (layer-0) and a steel substrate (layer-2) holding thermal parameters as in the table 3.1. Here the choice of steel substrate is because of its high thermal effusivity that improves the sensitivity via the increased thermal mismatch between the sample and backing. This configuration allows one to find out the thermal diffusivity and effusivity of a liquid sample simultaneously knowing the thermal parameters of the surrounding layers and the sample thickness. The zero crossing method [82] is also valid for finding the thermal diffusivity of the sample from the normalised phase knowing only the thickness (d) and zero crossing frequency ($f_{(\theta=0)}$) and is given by:

$$\alpha_1 = \frac{4d^2 f_{(\theta=0)}}{\pi}, \; n = 1, 2, 3... \tag{3.12}$$

3.1.3 Photothermal Radiometry Experimental Set Up

The general procedure for conducting PTR experiments is relatively simple [65]. Like other photothermal techniques [63], the sample under investigation is heated periodically at a frequency, $f = \omega/2\pi$, where ω is the angular frequency, using an intensity modulated laser beam. These heat pulses diffuse into the sample layers and produce periodic temperature variations, thus emitting infrared (IR) waves. These emitted IR signals are collected by the aid of proper optical arrangements and focused into an IR detector. A lock-in amplifier locked at the same modulation frequency of excitation quantify the output from IR detector. As obtained signal contains both the thermal parameters of the sample layers and the contribution from instrumental transfer function which comes from the underlying electronic circuitry. A proper normalisation procedure allows one to filter out the signal that depends only on thermal parameters of the sample layer system. Figure 3.6 shows the schematic representation of a classical PTR set up.

3.1.3.1 From Laser Excitation to Infrared Detection

Laser source:- Laser beam of wavelength (λ =532 nm) corresponding to the green color in the electromagnetic spectrum has been used as the source (manufacturer Laser Quantum, He-Ne, Ventus HP 532, 1.4 mm spot size).

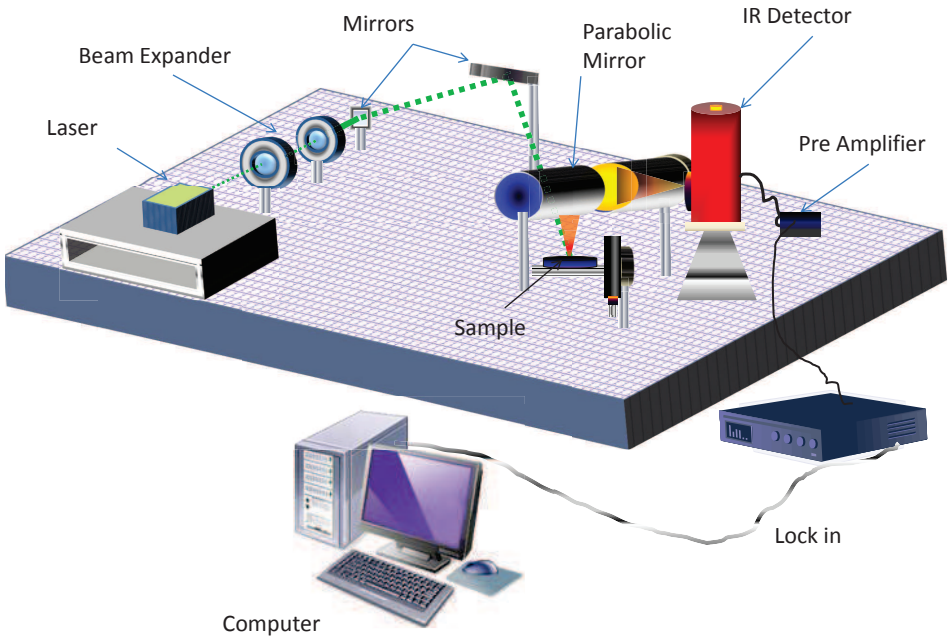

Figure 3.6: Photothermal infrared Radiometry set up

Acousto-optic Modulator:- The laser module contains an internal modulator with a maximum modulation frequency of about 10 kHz. For intensity modulations above this frequency range, a separate acousto-optic modulator (IntraAction, AOM-40) was used.

Optical arrangements:- The Infrared signal coming out of the sample surface was collected and focused by two parabolic gold coated mirrors (Edmund Optics, 90 DEG Off Axis Parabolic, M2 R184613-10140). A telescopic lens arrangement with a magnification factor of six has been used to make the spot size (8.4 mm) big enough to avoid three dimensional effects at the experimental range of frequencies.

IR Detector:- A liquid nitrogen cooled HgCdTe Infrared detector (Judson Technologies, Model: J15D12-M204-S01M-60; bandwidth: DC - 250 kHz) was used. Photograph from an experiment showing the sample, detector and optical arrangements are displayed in fig. 3.7

3.1.3.2 Electronic Circuitry and Signal Recording

The detector signal was converted to voltage and pre amplified by PA 300 pre-amplifier. This amplified signal was then connected to a Lock-in amplifier (SIGNAL RECOVERY,

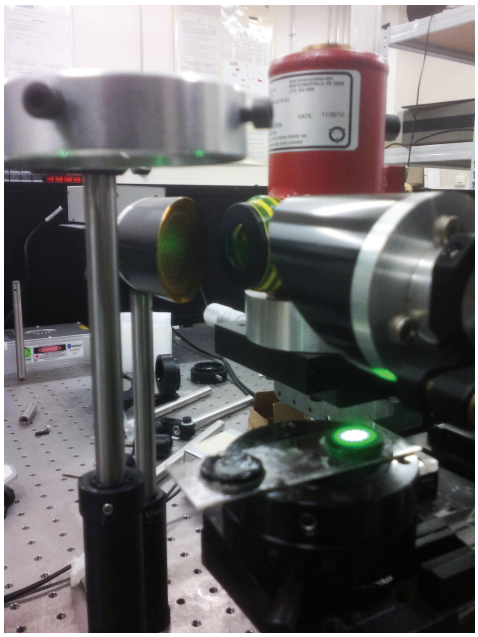

Figure 3.7: A photograph of the experimental setup

model: 7260, maximum oscillator frequency: 250 kHz). The Lock-in was connected to a personnel computer via Agilent GPIB (General Purpose Interface Bus) card. The complete experiment was automatized using LabVIEW software from National Instruments (NI). Figure 3.8 is the LabVIEW front panel for controlling and recording the experiments automatically.

3.1.3.3 Temperature Controlling

A home made heater powered by a programmable power supply (Instek, PSS-2005, 0-20V, 0-5A) was used for heating the sample cell. This helped to conduct experiments under constant temperature as well as to carry out measurements under varying temperature. As used temperature controller, controlled by a computer based PID (Proportional Integral Derivative) controller, had the ability to regulate temperature better than 10 mK inside the sample cell.

3.1.3.4 Electric Field Varying Experiments

For electric field varying measurements (e.g., liquid crystal re-orientation), signal from a function generator (RIGOL, DG2021A) was amplified with a $\times 20$ Voltage amplifier (model:F20A) and applied to the sample cavity.

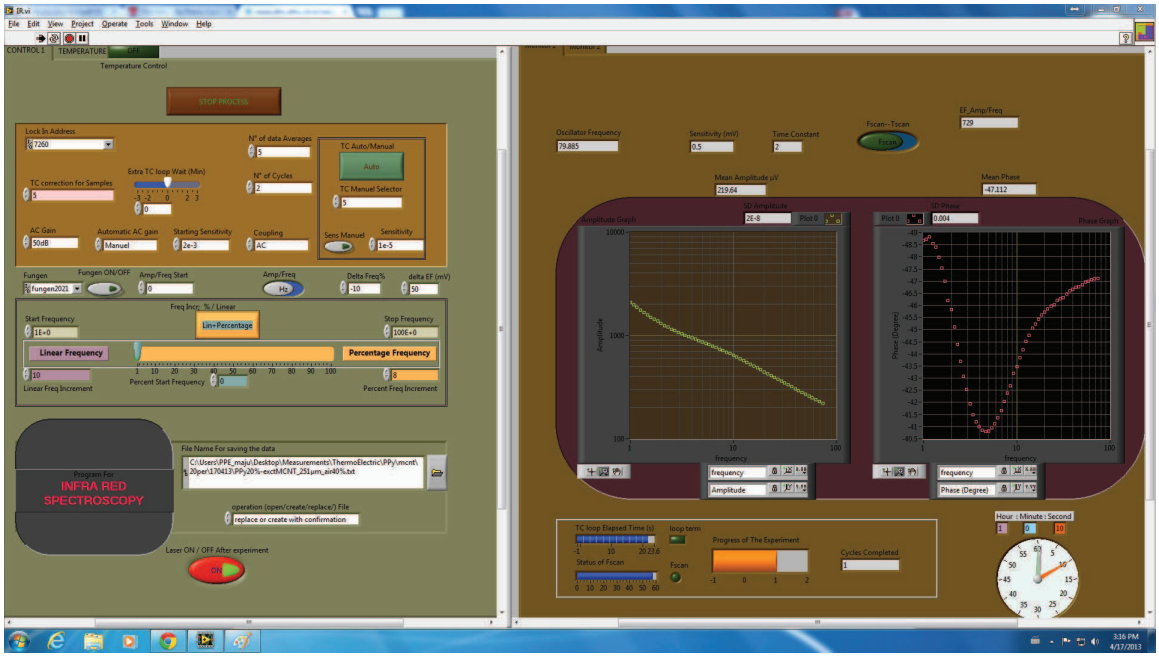

Figure 3.8: Front panel of the LabVIEW program used for the automation of experiments.

3.1.3.5 Cell for Liquid Samples

A 2.mm thick (24.mm diameter) CaF_2 window (from Crystran, UK) having good infrared transmission range (λ = 300nm to 10μm) was used as the top semi-infinite layer for all the front and back experiments. While for the backing we have chosen special quartz cuvettes (cells with detachable windows, type: QS 124, sample space thickness error $\leq$ $\pm$5%, from Hellma analytics), which in principle serves as the sample holder and gives excellent accuracy over the sample thickness.

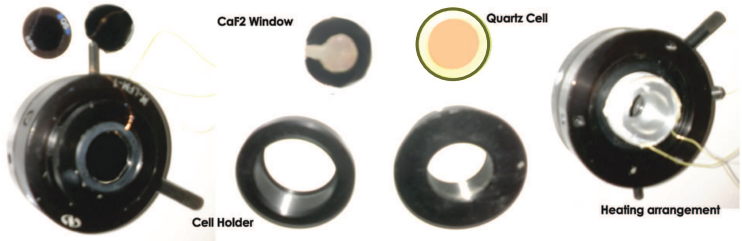

Figure 3.9: Photograph of the cell assembly used for liquid measurements using PTR technique

For all liquid measuring methods, sample heating by the laser absorption was achieved by making thin opaque metallic coatings at both of the interfaces; sample-CaF_2 and sample-backing interfaces. These metallic coatings were also served as electrodes for the electric field varying experiments. The thickness of these coatings were typically a few hundreds of

nanometers and assumed to have no effect on the normalized signal because these coatings are thermally very thin in our experimental frequency range. It was also insured that no incident laser beam was transmitted through the opaque coatings at the interfaces validating the surface absorption model. Figure 3.9 shows the cell windows used for the liquid experiments. The CaF_2-Sample-backing assembly was mounted inside a 25 mm holder and tighten together in order to maintain the sample thickness unchanged.

3.2 Validation Experiments on PTR Methods for Measuring Thermal Properties of Liquid Samples

Verification of the PTR methods for thermal characterization of liquids described in section 3.1.2 has been investigating firstly using water and glycerol as samples, which are having well known thermal parameters. All the experiments were carried out at ambient temperatures (20-22 ^{0}C). Experimental setup and the cell arrangements for liquid sample encapsulation are described in section 3.1.3. The thermal parameters of the surrounding layers and reference materials used for the normalisation procedure are given in table 3.2.

Table 3.2: Thermal parameters used as input data for fitting.

Material	Diffusivity (m^2s^{-1})	Effusivity ($Jm^{-2}K^{-1}s^{-1/2}$)	Conductivity ($Wm^{-1}K^{-1}$)
CaF_2	3.58 $\times 10^{-6}$	5135	9.71 [a]
Quartz	8.4 $\times 10^{-7}$	1506	1.38
Water[b]	1.43$\times 10^{-7}$	1581	0.598
Steel	–	7535	–

[a] Data sheet, Crystran Ltd., [b] Ref.[81] water at 20 ^{0}C.

3.2.1 Results obtained with BF-PTR configuration

3.2.1.1 BF-PTR experiment with water

The normalized experimental amplitude and phase for water sample plotted as a function of square root of modulation frequency is shown in figure 3.10. A least square fitting has been done on the experimental amplitude, phase and complex (fitting amplitude and phase data together simultaneously) data against theoretical model described in eq. (3.5) in order to extract the thermal diffusivity of the sample under investigation. The best fitting results corresponding to lowest χ^2 values are given in table 3.3 together with other literature values for comparison. The agreement of the results with the thermal diffusivity values from literature support the validity of the method. The precision cells helped to minimize the errors due to thickness uncertainties and which are neglected in the calculations.

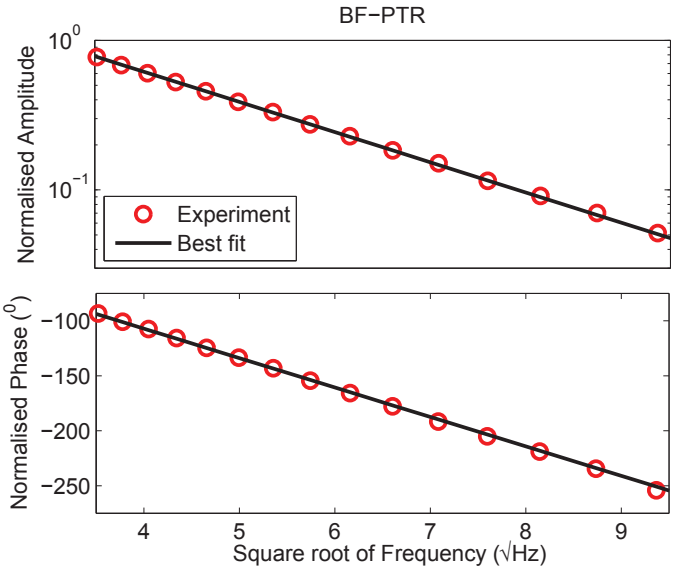

Figure 3.10: Normalized BF-PTR signal amplitude (upper plot) and phase (lower plot), plotted as a function of square root of the modulation frequency for water sample (d =100μm). The circles are from the experimental data and the full line represents the best fit. CaF_2 window is used as the top layer and quartz cell as the backing.

Least Square Analysis and Error Calculation :

In table 3.3, the best fit values and their statistical uncertainties (σ_p) for diffusivity (α_1) (one of the fitted parameter) calculated from each type of experimental signals (amplitude, phase and complex) are presented. The χ^2 cost function is calculated by:

Table 3.3: Thermal Diffusivity from BF-PTR.

Sample	BF-PTR			Literature
	Amplitude fitting	Phase fitting	Complex fitting	
	$10^{-7}(m^2s^{-1})$			$10^{-7}(m^2s^{-1})$
Water	1.441±0.005	1.435± 0.006	1.436± 0.006	1.437±0.008[a] , 1.43[b]
E.G	0.926±0.006	0.924±0.007	0.922±0.009	0.918±0.002[c]
Lanolin	0.50±0.02	0.49±0.02	0.53±0.03	—

[a][45] at 25^{0}C; [b][81] at 20 ^{0}C; [c][83].

$$\chi^2 = \frac{1}{N}\sum_{j=1}^{N}\left[\Gamma_{exp}\left(\omega_j\right) - \Gamma_{theory}\left(\omega_j, \mathbf{p}\right)\right]^2 \tag{3.13}$$

with N, the number of summed quadratic differences of the experimental and theoretical values; $\omega_j (j = 1...N)$, the experimentally available frequencies; $\Gamma_{exp}\left(\omega_j\right)$, is the normalized experimental signal; $\Gamma_{theory}\left(\omega_j, \mathbf{p}\right)$, corresponding theoretical normalized signal. $\mathbf{p}$ is the set of fitting parameters. Least square analysis finds best set of fit parameters by varying all of them (fit parameters) so that a lowest χ^2 value is achieved. Then the fitting uncertainty σ_p for each fit parameter, e.g. α_1, is calculated by varying its value around the best fit while keeping all other parameters constant.

$$\sigma_p = \sqrt{\frac{2}{(N-P)\,\frac{\partial^2}{dp^2}\left(\chi^2(\mathbf{p})/\chi^2(\mathbf{p}_0)\right)}} \tag{3.14}$$

Here, $\mathbf{p}_0$ is the optimised set of fitted parameters corresponding to the lowest χ^2 value obtained from the least square analysis and $\mathbf{p}$ is the set of parameters containing the varying parameter for which the uncertainty to be calculated. In eq. (3.14), the second order partial derivative of χ^2 function was obtained by fitting a parabola through $\chi^2(p)$, where p is the varying parameter during the χ^2 analysis. The steepness of this parabola is inversely proportional to the fit parameter's uncertainty.

Interestingly the small values of the uncertainties comparable with the PPE measurement results represent the high sensitivity of the method and quality of the experimental

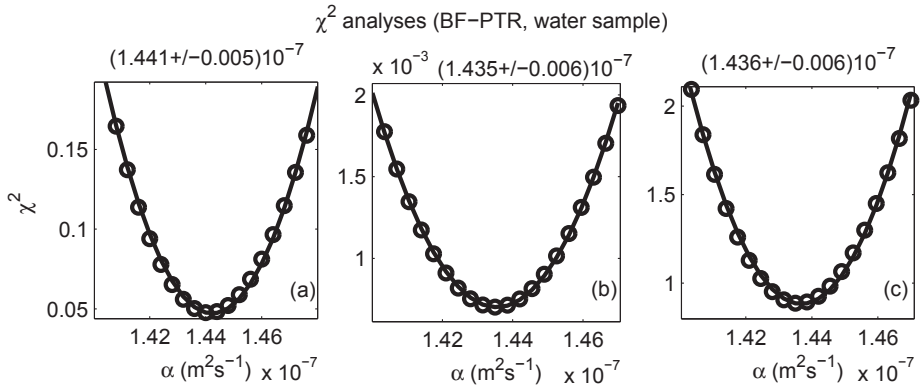

Figure 3.11: χ^2 analyses in the neighbour hood of its minimum for calculating the statistical uncertainty. Analyses on amplitude (a); phase (b); and on complex (c) data.

signal. The experimental results on ethylene glycol (E.G) and lanolin (wool wax)[84] are also included in table 3.3.

3.2.1.2 BF-PTR experiment on 5CB with varying electric field

Liquid Crystals and their Physical Characteristics :

Liquid crystal (LC) compounds are special class of materials exhibiting crystal ordering in liquid state. Because of such unique property, LCs unfolded improved class of optical devices which are thin, light in weight and even foldable. Thermodynamically, this liquid crystalline phase exists in between the melting point and the isotropic clearing temperature of material. Ordinarily, LCs may display one or more mesophases depending on the molecular symmetry and three major classes of these mesophases are: nematic, smectic and cholesteric. The differences between these mesophases are coming from their lattice order parameter.

Nematic liquid crystals tend to align themselves parallel to one another along an arbitrary principle axis (n). While cholesteric phase happens when there is a "twisting" of the nematic director between consecutive layers, usually in helix form. In smectic phase, the molecules align parallel to one another within a layer and inter layer translational movements are restricted. Figure 3.12 schematically explains these LC phases.

Liquid crystals in its crystalline phase are opaque and turbid fluid to our naked eye but it shows characteristic optical textures due to its strong birefringence property when looking through a polarizing microscope. In normal form, direction of the director, n,

can be in any arbitrary direction within the mesophase. Interestingly, these directions and thereby their properties can be controlled by different ways, e.g, rubbing or surface treatment of the material in contact, applying electric or magnetic field etc. These unusual optical properties and the possibility to control it have attracted the scientific world to use it in various areas.

Here, we have studied the variations of 5CB liquid crystal thermal diffusivity under varying electric field (EF) (sinusoidal electric field of fixed frequency (f_e)= 1kHz was chosen to avoid polarization field effects at LC-electrode boundaries). Figure 3.13 shows a schematic representation of liquid crystal molecular alignment before and after the application of an applied electric field. When the LC sample is sandwiched between the cell walls, all the molecules take the direction parallel to the cell wall. This alignment depends on the surface characteristics of the cell surface in contact with LC. Different chemical and physical treatments governs the LC molecular alignment. Since the thermal transport properties are anisotropic in LC materials, the heat transport is maximum in the direction of the molecular alignment axis or director (n). So, if n is parallel to the cell wall (like in fig. 3.13(a)), the thermal conductivity normal to the cell wall (normal to n) is lower than that in the parallel direction. Now, upon the application of a sufficiently strong electric field, the LC molecules try to align in the direction of EF, normal to the cell walls. Thus the thermal conductivity also increases in this direction.

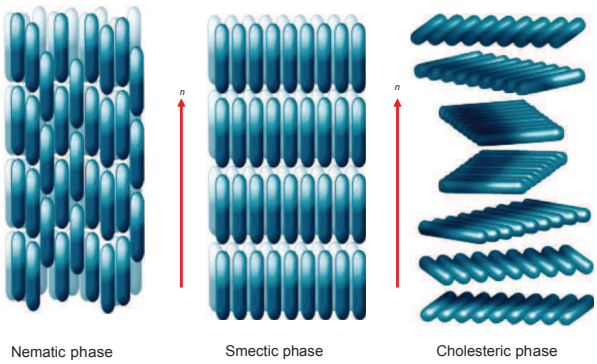

Figure 3.12: Three of the main liquid crystal phases.

Experimental Results on 5CB Liquid Crystal :

Laser intensity modulated frequency scans for different applied electric fields on LC sample were conducted for finding thermal parameters. Normalisation for each back frequency scan has been done with the corresponding front frequency scan. The results were obtained by fitting the normalized experimental signals using equation (3.5). In practice,

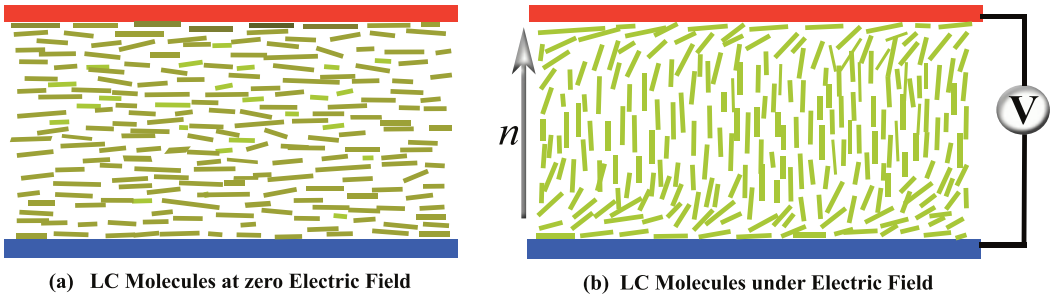

Figure 3.13: LC molecules under zero and an applied electric field.

a single front frequency scan serves the purpose as the normalisation signal for all the back scans because, the front signals are less sensitive to the variation of the sample's thermal parameters and thus resulting in similar or same amplitude and phase values in all the front scans. It is also worthy to mention that the scans were done near to sample's quasi thermally thick regime, where the experimental signal is most sensitive to the sample's thermal diffusivity. The experiment has been carried out around $\sim 28\ ^0$C (nematic phase: 25 ^{0}C - 35 ^{0}C). The LC is dropped into the sample holder and heated above 35 ^{0}C, until its clearing temperature, before closing the cell for the experiment. Our results on the electric field dependent thermal diffusivity of 5CB are shown in figure 3.14.

The thermal diffusivity variation is about 9% without doing any pre surface treatments which is necessary to obtain high degree planar alignment and thereby increased thermal parameter contrast [85]. This behaviour of the thermal diffusivity of 5CB as a function of electric field is similar to the one obtained with PPE in reference [23].

3.2.2 Results obtained with B-PTR configuration

3.2.2.1 B-PTR experiment on glycerol

Back-PTR (B-PTR) method has the advantage of getting thermal diffusivity and effusivity of liquid samples simultaneously with high certainty. Figure 3.15 shows the frequency dependent experimental result on glycerol (sample) normalized with water (reference). The thermal parameters used for the reference liquid are from table 3.2. The experimental data (amplitude, phase and complex) have been fitted with equation (3.8) to obtain the thermal diffusivity and effusivity. The results obtained for the best fitting values of glycerol

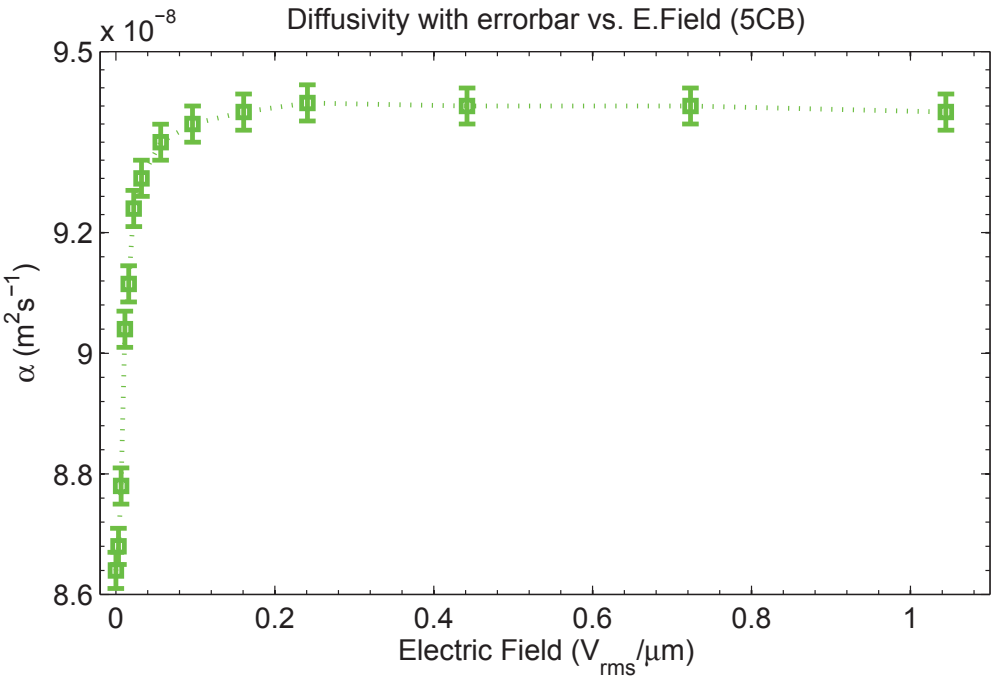

Figure 3.14: Variation of thermal diffusivity of 5CB liquid crystal (at 28 ^{0}C) vs. varying electric field (sinusoidal, 1kHz) from the BF-PTR experiment.

with statistical uncertainties are shown in table 3.4 and these results are in good agreement with the already reported values. For checking if the obtained set of values having any pair wise fitting dependency, we have performed a contour map for the χ^2 cost function vs. α and e as in figure 3.16(a). It shows closed curves around the best fitting pair of values which confirms the absence of any interdependency between the two thermal parameters.

Most Squares Inversion and Multi-Fold Degeneracy :

Assessment of two fold degeneracy (between any two fitting parameters) can be brought out by plotting contour plots but a three fold or higher (multi fold) degeneracy cannot be viewed in 2-D plots. Here a third fitting parameter called proportionality factor (A_f) which comes from the sample-reference replacement (A_f has effect only on the amplitude and not on the phase. A possible reason for including A_f is coming from the small changes in absorbed laser intensity due to the sample cell rearrangements which can alter the amount of photothermal heat generation) may introduce the chances to have a three fold degeneracy (same results for different sets of input parameters) between the three unknown fitting parameters (α, e and A_f). It can be brought out by doing so called "Most Squares

Table 3.4: B-PTR and F-PTR Experimental results on Glycerol.

Method		Diffusivity $\times 10^{-8}(m^2s^{-1})$	Effusivity $(JK^{-1}m^{-2}s^{-1/2})$
B-PTR	Amplitude fit	9.45 ± 0.02	958 ± 2
	Phase fit	9.425 ± 0.007	940 ±10
	Complex fit	9.43 ± 0.02	945 ± 3
F-PTR	Complex fit	9.5 ± 0.3	945 ±11
Ref.[81] (25^0C)		9.99	923

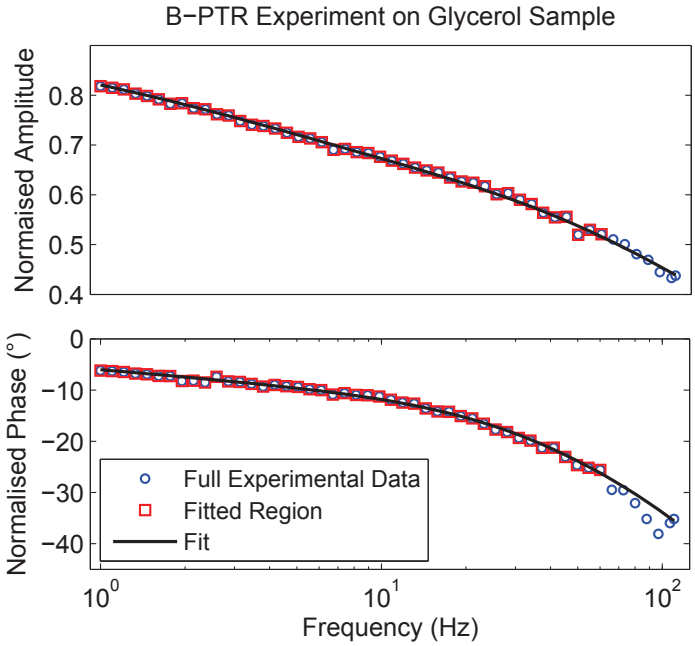

Figure 3.15: Experimental result on glycerol (sample) normalized with water (reference) plotted as a function of f. Amplitude (upper plot) and phase (lower plot) are fitted simultaneously. The symbols show the experimental curve and the full line represents the best fit (d=50μm).

Inversion" [45, 86]. In classical least-squares error analysis procedure (described in section 3.2.1.1), each parameter vary around its best fit value keeping all other parameters fixed unambiguously and calculates the error. While in the case of most squares error analysis, each chosen value of a selected parameter (e.g., α) around its best fit is optimized by varying all other fitted parameters until minimizing the χ^2 cost function. So, for each value of the selected parameter, an additional least square analysis by minimizing the χ^2 cost function is being carried out in order to optimize the full set of fit parameters. The results from the most squares analysis can be analysed as in the following way. If the analysis shows a single minimum, which means that the obtained set of values are unique. On the other hand if it shows a flat line, it indicates a multi-fold degeneracy which means that the fit parameter set satisfies more than one solution for the same experimental data. Figure 3.16(b, c) shows the least square and most-squares analysis for the thermal diffusivity and effusivity. The parabolic shape of the plots indicate the absence of degeneracy with all other fitting parameters for each of these thermal quantities. The sharpness of the parabola is a proof of lower statistical uncertainty and high accuracy of the experimental method. From fig. 3.16(b, c) it can be noted that the most squares curves are broader than the χ^2 curves. This is because the most squares analysis take into account of covariance with the other fitting parameters.

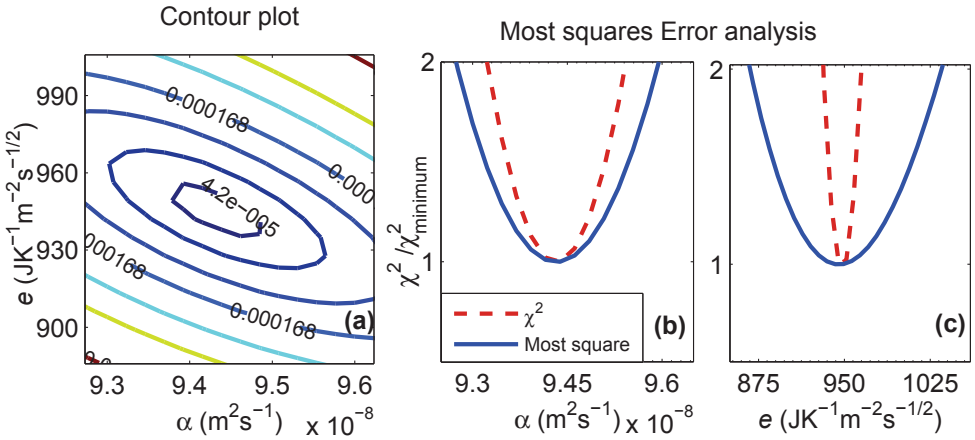

Figure 3.16: Contour plot (a) showing the closed curves with χ^2 minima around the best fitting values of α and e confirms the absence of degeneracy. Most square error analysis (full line) plotted along with the least-square (dashed line) for thermal diffusivity (b) and effusivity (c) confirming that the results are unique. The statistical uncertainty is inversely proportional to the sharpness of the parabolic minima. The analysis is for the B-PTR experiment (fig. 3.15) with glycerol as sample and water as the reference.

3.2.2.2 B-PTR experiment on 5CB with varying electric field

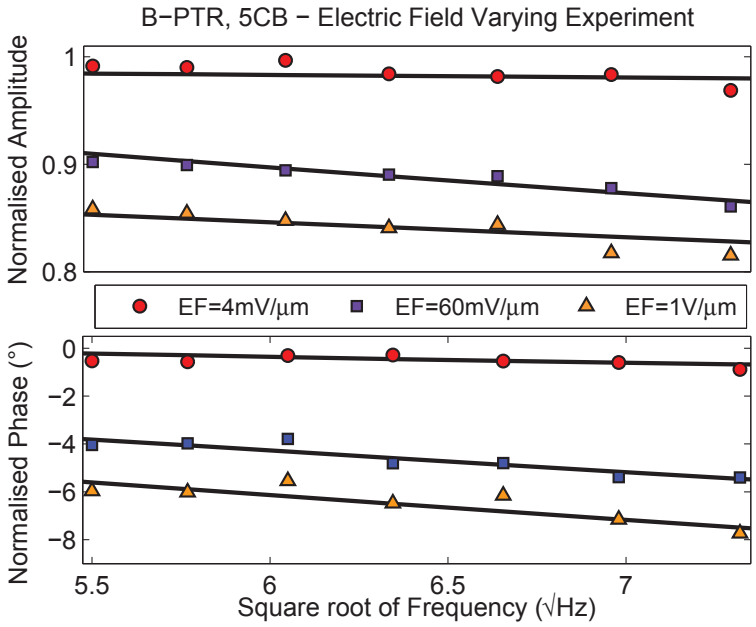

Figure 3.17: Normalized experimental signals (symbols) and the best fits(lines) are plotted vs. laser modulation frequency for 5CB liquid crystal sample under three different electric fields. Signals are fitted to obtain α and e keeping A_f fixed. The reference signal was from the sample at zero electric field.

Employing B-PTR experimental method, we have also investigated the variations of α and e for 5CB liquid crystal sample with varying electric field. The obtained results are from the scans performed at high sensitive frequency region, where the sample was in quasi thermally thick regime. The frequency scan at zero electric field was taken as the reference signal for normalisation for all other signals with applied electric field, thus the A_f kept fixed. The reference thermal parameters for the 5CB at zero electric field for thermal diffusivity was from the BF-PTR result on 5CB and for the effusivity was from reference[23]. Figure 3.17 shows the typical normalized experimental signals as a function of frequency for three different electric fields. The normalized signals were fitted using equation (3.8) and figure 3.18 shows the obtained thermal diffusivity and effusivity values plotted as a function of applied electric field.

3.2.2.3 B-PTR experiment on 5CB with varying temperature

Depending on the temperature, liquid crystal materials show different phases such as crystalline (C), smectic (Sm), nematic (N), isotropic (I) etc. So the thermal transport prop-

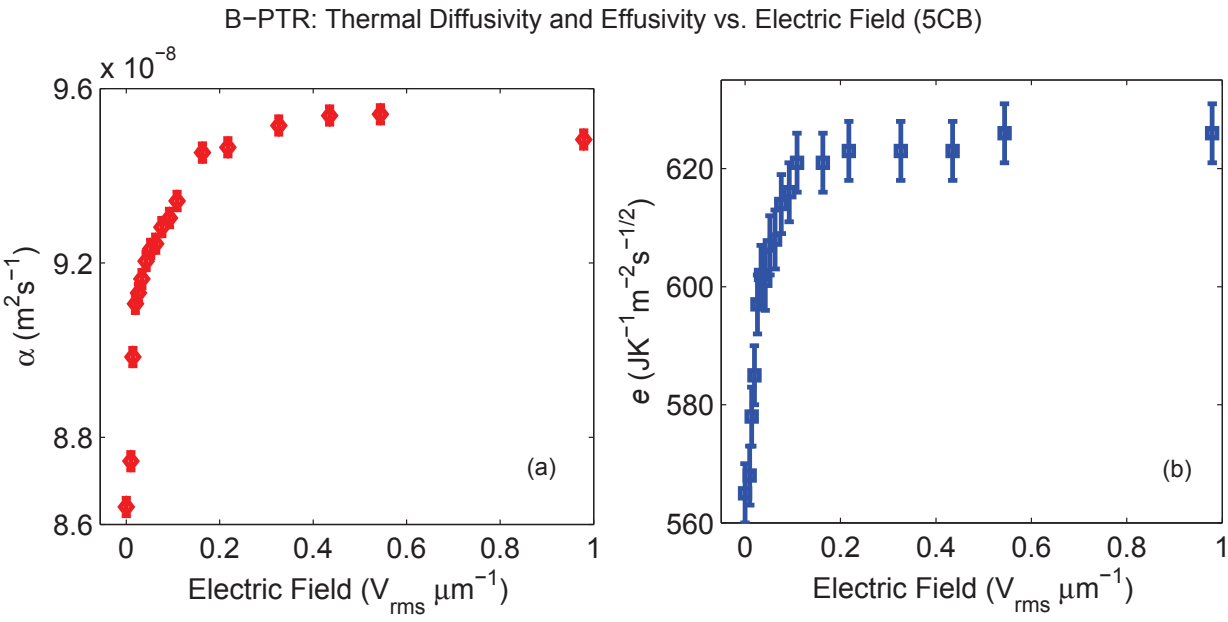

Figure 3.18: Variation of thermal diffusivity,(a) and thermal effusivity,(b) with error bar of 5CB liquid crystal as a function of electric field. Results from B-PTR experiments done at 28 ^{0}C.

erties are also different in these phases. Moreover, on the transition from one phase to another, different transport properties show continuous or discontinuous transitions due to the change in its molecular order parameter. Here, we are investigating the widely studied temperature dependent N-I transition in 5CB for validating B-PTR method.

Since B-PTR has the advantage of finding thermal diffusivity and effusivity simultaneously from a single frequency for those measurements in which A_f is kept fixed, it helps to avoid time consuming frequency scans while preserving better accuracy. Sample's thermal diffusivity can be calculated from the phase and the effusivity from the combined amplitude and phase signals considering the sample is at quasi thermally thick ($\mu_s \approx d$) frequency regime where the negative exponential term in equation (3.8) can be approximated to zero ($e^{-2\sigma_1 d} \approx 0$). The analytical expression for α and e are given by:

$$\alpha_s = \left(\frac{d\sqrt{\alpha_r \pi f}}{d\sqrt{\pi f} - \theta\sqrt{\alpha_r}} \right)^2 \tag{3.15}$$

$$e_s = -\frac{1}{2}\left\{ L - R + \sqrt{(L-R)^2 - 4J} \right\} \tag{3.16}$$

where,

$$R = \frac{\exp(\theta)}{e_r A}\left(e_r^2 + e_r L + J\right) \qquad L = e_c + e_b \qquad J = e_c e_b$$

and A is the normalized amplitude and θ is the normalized phase. e_r, e_s, e_c and e_b are the thermal effusivities of reference, sample, CaF_2 window and backing respectively. α_s and α_r are the thermal diffusivities of sample and reference respectively. f represents the modulation frequency and d is the sample thickness. Figure 3.19 shows the variation of thermal diffusivity, effusivity and conductivity (calculated from α and e) vs. temperature for the 5CB liquid crystal. The temperature dependent experimental signal was normalized with the signal at the isotropic phase and the reference values were chosen from reference[85]. The experiment has been done with a single stage temperature controller with temperature resolution better than 10 mK.

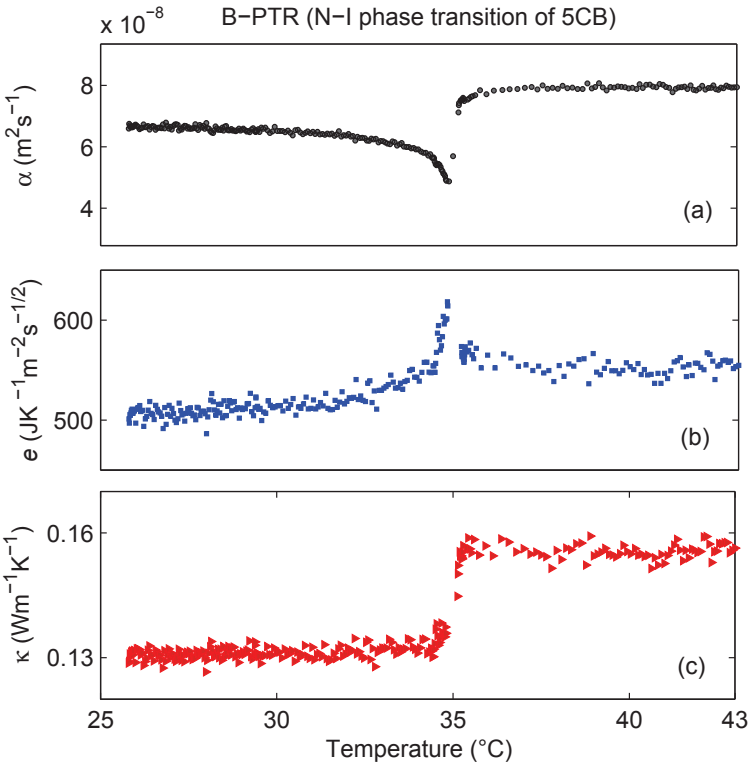

Figure 3.19: Experimental results on variations of thermal diffusivity (a), thermal effusivity (b) and thermal conductivity (c) from the temperature varying B-PTR experiment around the Nematic - Isotropic (NI) phase transition of 5CB. The experiment has been done at f =32Hz (laser modulation frequency) and d =36μm. The thermal conductivity has been calculated from e and α.

3.2.3 Results obtained Using F-PTR configuration

In order to validate F-PTR method, we have measured thermal diffusivity and effusivity of glycerol. The experiment has been conducted as described in section 3.1.2 and the

normalisation has been done with the same semi infinite sample. The results on glycerol as the sample are included in table 3.4. The sample is sandwiched between the CaF_2 window, which acts as the semi infinite top layer, and a highly effusive steel backing in order to obtain better sensitivity to sample's thermal parameter changes. The sample space is created by an O-ring shaped mica film and placed in between the top layer and the backing. The thickness of the sample space has been calibrated using water as the sample having known thermal parameters as indicated in table 3.2. The normalised experimental amplitude and phase plotted as a function of modulation frequency, as shown in fig. 3.20, are fitted using eq. (3.11).

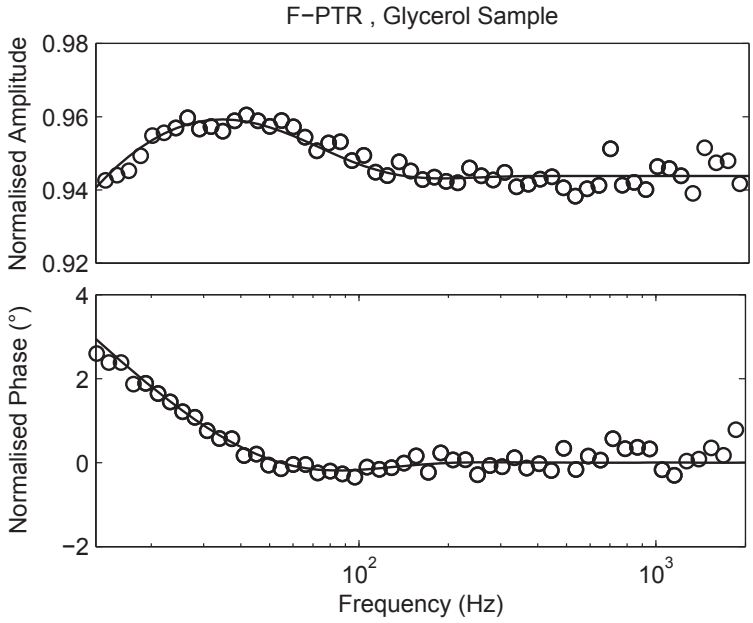

Figure 3.20: Normalized experimental signal for Glycerol sample (d =38μm) using F-PTR plotted as a function of laser modulation frequency. Normalisation has been done with semi infinite sample. Circles show the experimental data and the full line represents the best fit.

The obtained results from our experiments are in good agreement with the already reported values and also with the results obtained with B-PTR experiments. The uncertainties in the experimental results, obtained from the least squares error analysis by minimizing the χ^2 cost function, for each thermal parameters, are also included in table 3.4. Since this configuration has less sensitivity towards sample's thermal parameters, the results have bigger uncertainties than the results from BF-PTR or B-PTR configurations.

3.2.4 Plausibility of PTR Methods for Characterizing Liquid Sample's Thermally

Until now, the most used method for liquids thermal characterization is probably the PPE calorimetry. The main advantage of this method compared to other PT techniques is its simplicity: it measures directly the temperature variation of the sample with the special feature for liquids of a perfect liquid/pyroelectric sensor thermal contact. In this work, we propose the PTR technique as an alternative calorimetry. Concerning the accuracy of the investigations, in both techniques, when using sandwiched detection cells, it was demonstrated [70, 44] that it is connected with the values of the thermal parameters of the layers of the detection cell; more exactly, the accuracy is increased when the values of the thermal effusivity of the liquid and backing layers are close. In the PTR configurations proposed in this work, the backing layer is glass with a thermal effusivity rather close to the typical liquids, so the experiment is optimized in order to obtain high accuracy. While considering the signal to noise ratio, PPE outperforms PTR, which limits the temperature resolution granted by the PTR in highly resolved temperature dependent measurements. Some recent advances in IR detection technologies promising us improved sensing possibilities [87] which in principle allows to perform experiments at extremely low laser powers than it requires now. The requirement of IR transparency of the first layer of the proposed PTR detection cell can be easily fulfilled, a lot of commercially available materials satisfying this criterion.

3.3 Thermal Transport Studies in Polymer Dispersed Liquid Crystals (PDLC) Under Frequency Dependent Electric Field

Polymer Dispersed Liquid Crystals (PDLCs) are the subject of study in our lab for the past few years. Until now only the different aspects governing the thermodynamic of the phase separation and the electro-optical performances (transmission properties, drive voltage, switching times, etc.) of these materials have been extensively investigated. The studies on thermal transport properties of PDLC samples can be very interesting in this

heterogeneous material composite. We have used the PTR technique developed for liquid studies to determine the thermal behaviour of the PDLC systems under applied electric field.

PDLCs are modified edition of the conventional LC technology. These are made up of micron or sub-micron sized LC droplets encapsulated inside a polymer matrix. One of the usual procedure of preparation is in-situation polymerization of host polymer matrix in the presence of LC proceeded by phase separation. This manufacturing procedure is especially simple and avoids the requirements of surface aligning or cell filling and sealing which are needed in the case of twist cells. Conventional LC (super twist cells, twisted nematic (TN) cells, π-cell) needs the use of polarisers while PDLC's do not require any polarisers. It particularly reduces the power loss due to the absence of polarisers (polarisers absorb $\sim 50\%$ incident light in LC cells) and thereby increases the device efficiency. Moreover, in high temperatures, polarisers often degrade or peel off. Sturdy environmental properties, fast switching time and low production costs are other attractions of PDLC technology. Some of its electro-optical applications are: flexible displays [88, 89, 90], window shutters, projection displays [91], optical switches [92], focus tunable lenses [93] etc.

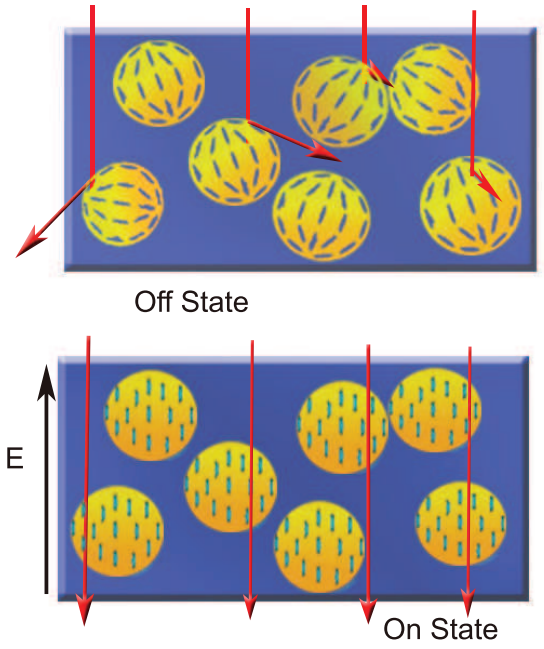

Figure 3.21: PDLC before and after applying electric field E. The downward arrows showing the light path.

The principle of operation is based on the electric field-controlled optical transmission properties of the composite materials sandwiched between two transparent conducting electrodes. Light is efficiently scattered in the initial off-state (zero field) because of the refractive index mismatch between the droplets and the matrix. Application of electric field causes the LC molecules to orient within the droplets and if the ordinary refractive index of the LC matches that of the matrix a high degree

of transparency can be achieved (fig. 3.21). Upon removal of the voltage, the droplets return to their original random orientation inducing light scattering.

3.3.1 Maxwell-Wagner-Sillars Effect

Polymer dispersed liquid crystal assembly is a heterogeneous mixture of LC and polymer. Because of the difference in dielectric characteristics (ability to hold charges) and electrical conductivities in these material mixture components, an additional charge polarisation occur at each LC-polymer boundaries upon the application of an EF as in fig 3.22. At lower frequencies, the blocking inner charges at the boundaries start to build up and produce reduction in the equivalent applied EF strength. This interfacial polarisation effect, also known as Maxwell-Wagner-Sillars (MWS) effect [94, 95] in a multiple phase mixture, vanishes at sufficiently high frequencies of applied EF at which the movement of charges become frozen out and the development of depolarisation field interrupts.

Since this effect crucially affects electro-optical properties of such heterogeneous systems, a clear understanding of such properties are important in the application point of view. Several authors have studied this interfacial effects and its consequences in electro-optic properties are reported [96, 97, 98]. Boussoualem *et al* [99, 100] conducted differential scanning calorimetry (DSC), dielectric spectroscopy and electro-optic studies on polystyrene PS/ (4,4'-octylcyanobiphenyl) 8CB and PS/5CB dispersed systems and reported frequency dependent behaviour attributed to the MWS effect in such mixtures. Their electro-optic studies were showing the variation of light intensity vs. frequency ($f_e = \omega_e/2\pi$) of the applied electric field and which were explained in terms of MWS effect by considering the self consistent field approximation for calculating the electric field (E_{drop}) inside a spherical

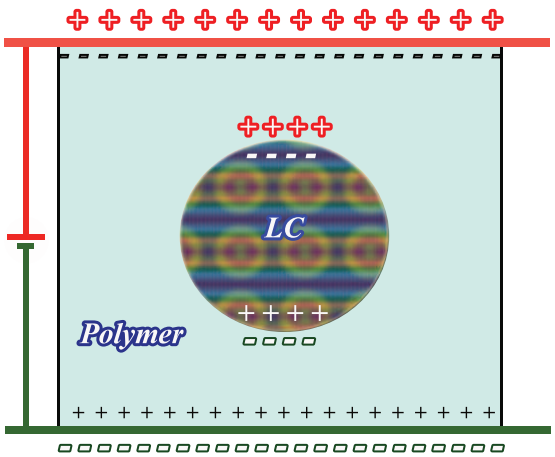

Figure 3.22: Maxwell-Wagner-Sillars effect in a heterogenious medium

droplet under sinusoidal field [101, 102], which is given by:

$$E_{drop}(\omega_e) = \frac{3\epsilon^\star_M}{\epsilon^\star_{\mathrm{LC}} + 2\epsilon^\star_M - \phi_{\mathrm{LC}}\left(\epsilon^\star_{\mathrm{LC}} - \epsilon^\star_M\right)} E_a e^{-i\omega_e t} \tag{3.17}$$

and,

$$\epsilon^\star_M = \epsilon'_M - i\frac{\sigma_M}{\omega_e \epsilon_0} \tag{3.18}$$

$$\epsilon^\star_{\mathrm{LC}} = \epsilon'_{\mathrm{LC}\|} - i\frac{\sigma_{\mathrm{LC}\|}}{\omega_e \epsilon_0} \tag{3.19}$$

where,

ϕ_{LC} $\Rightarrow$ Phase separated LC fraction.

E_a $\Rightarrow$ Magnitude of the applied electric field.

ϵ'_M $\Rightarrow$ Dielectric permittivity of polymer matrix

$\epsilon'_{\mathrm{LC}\|}$ $\Rightarrow$ Dielectric permittivity of LC aligned with E_a

$\sigma_{\mathrm{LC}\|}$ $\Rightarrow$ Electrical conductivity of LC in the direction of E_a

σ_M $\Rightarrow$ Electrical conductivity of Polymer matrix in the direction of E_a

Inside PDLC, a part of the LC dissolves into the polymer. The amount of LC which dissolves into the polymer is defined as solubility limit (β) and it can be found by doing DSC measurements. The undissolved part will form droplets. Knowing β and the amount of LC added to the polymer, x, one can calculate the phase separated LC fraction (ϕ_{LC}) using [103, 104, 105]:

$$\phi_{\mathrm{LC}} = \frac{100}{x}\frac{x-\beta}{100-\beta}, \qquad x \geqslant \beta \tag{3.20}$$

where, all the quantities are in weight percentage. Value of β is about 55% at room temperature has been used to calculate ϕ_{LC} using eq. (3.20) for finding the amount of LC droplet phase separated inside the polymer matrix.

In this section, we are analysing the MWS effect on dynamic thermal properties of PS/5CB composites and model it using eq. (3.17). Since the improved PTR methods for measuring liquid samples are capable of measuring thermal parameters with enough resolution, we have chosen B-PTR method (section 3.2.2) for experimental characterisation of the PDLC system. Because of the non-contact capability of the PTR technique, the measured thermal informations are free from electric field induced errors compared to contact techniques, for which, the signal can be affected by the electric field applied to the PDLC and making the measurements more tricky.

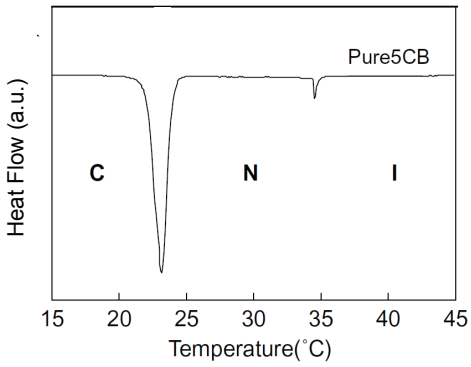

Figure 3.23: Thermogram of pure 5CB, showing crystalline (C) , Nematic (N) and Isotropic (I) phases of 5CB liquid crystal. Figure obtained from reference [20]

3.3.2 Thermophysical, Electrical and Dielectric Properties

Polymer Dispersed Liquid Crystal (PDLC) samples were prepared using polystyrene (PS) (Aldrich, molecular weight of 44000 g/mol as the polymer matrix and 5CB (Merck) as inclusion with two different volume ratios of LC:PS (85:15 and 73:27). Some of the advantages of PS compared to other thermo- plastic compounds are: very low ac conductivity ($\sigma_{\text{ac}} \approx 10^{-9}$ S/m), uniform dielectric permittivity ($\epsilon_M^{'} \sim 2.5$) in both temperature (25^0C - 80^0C) and frequency [106, 81].

The density (ρ) of PS and 5CB are ≈ 1 ($\rho_{\text{PS}} = 1.047$ kg/m^3 and $\rho_{\text{5CB}} = 1.008$ kg/m^3). Dielectric permittivity and ac electrical conductivity of 5CB are: $\epsilon_{\text{LC}\parallel}^{'} = 10$ and $\sigma_{\text{LC}\parallel} = 10^{-8}$ S/m [107, 108]. Figure 3.23 shows the phase diagram of pure 5CB and displaying the temperature range of nematic phase between 23^0C to 35^0C. Thermal conductivities of PS ($\kappa_m = 0.11$ W/mK) and 5CB aligned in parallel ($\kappa_{\text{LC}\parallel} = 0.24$ W/mK) and perpendicular ($\kappa_{\text{LC}\perp} = 0.12$ W/mK) used are taken from references [109, 85]

3.3.3 Chemical Synthesis

PDLC was prepared by dissolving liquid crystal and polymer in solvent and evaporating the solvent completely afterwards. 5CB and PS monomers in required amounts were dissolved in equal amount of chloroform firstly. After completely dissolving both 5CB and PS in chloroform, the mixture was placed in an oven and allowed for a complete evaporation of chloroform for more than 24 hours to obtain a final PDLC sample. Upon the solvent

evaporation, LC-PS phase separation happens and 5CB droplets of the order of micron or sub-micron size develops throughout entire polymer matrix. Micrographs of as prepared PDLCs for the two different samples are shown in fig. 3.24. The pictures are taken using a polarising microscope with crossed polarisers.

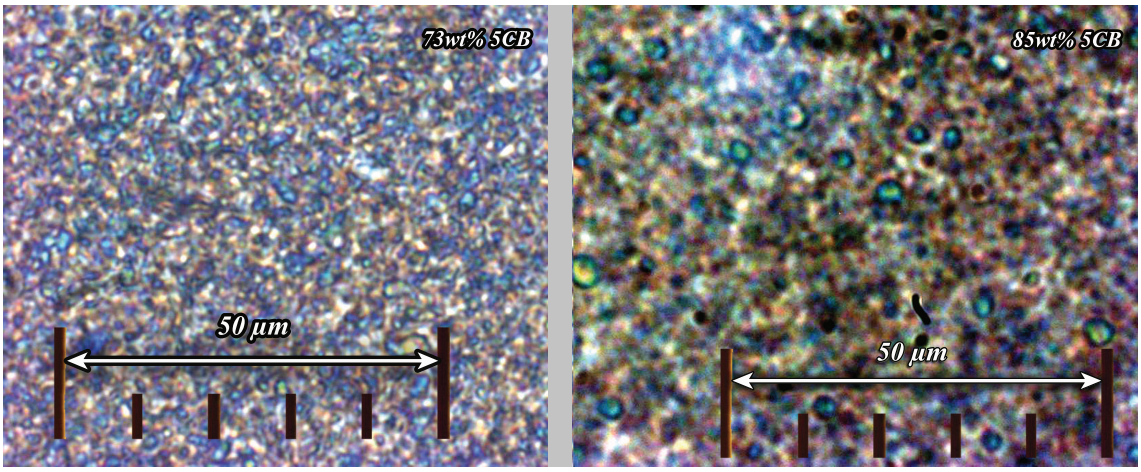

Figure 3.24: PDLC micrographs taken on a polarising microscope with crossed polarisers. Images of PS:5CB=27:73 (73% LC) (left) and PS:5CB=15:85 (85% LC) (right).

For the PTR experiment, required amount of PDLC sample was cast onto a quartz cell, prearranged with electric contacts for the electro-thermal measurements (see section 3.1.3 for the experimental procedure), using a spatula and heated it up above LC clearing temperature and closed the cell. The measurements were carried out by keeping the sample temperature constant at $\sim 28^0$C in order to avoid temperature dependent thermal property changes. Sample holder cell thickness used was $50\pm2\mu$m.

3.3.4 PDLC Under Varying Electric Field

We are interested on thermal properties of PDLCs under varying electric field is because of these composites offer the opportunity to modify the thermal characteristics of the inclusions (LC droplets) without changing physical properties of the system (same number, size and dispersion of inclusions). This is due to the fact that electric field reorients the molecules of liquid crystal in the droplets thereby change their thermal properties. In this manner, one can study and evaluate the contribution of the inclusions to the effective heat transport in the films.

Since the interfacial thermal resistance between different constituent phases in a com-

posite can play a critical role in the thermal behaviour of composite systems, the effect of this thermal resistance on the effective thermal conductivity of PDLC with different liquid crystal concentrations has been studied.

Firstly, we have investigated the variation of thermal parameters of both PDLC samples, (85% LC and 73% LC) under varying electric field at constant frequency ($f_e = 1$ kHz) and the results are depicted as in fig. 3.25.

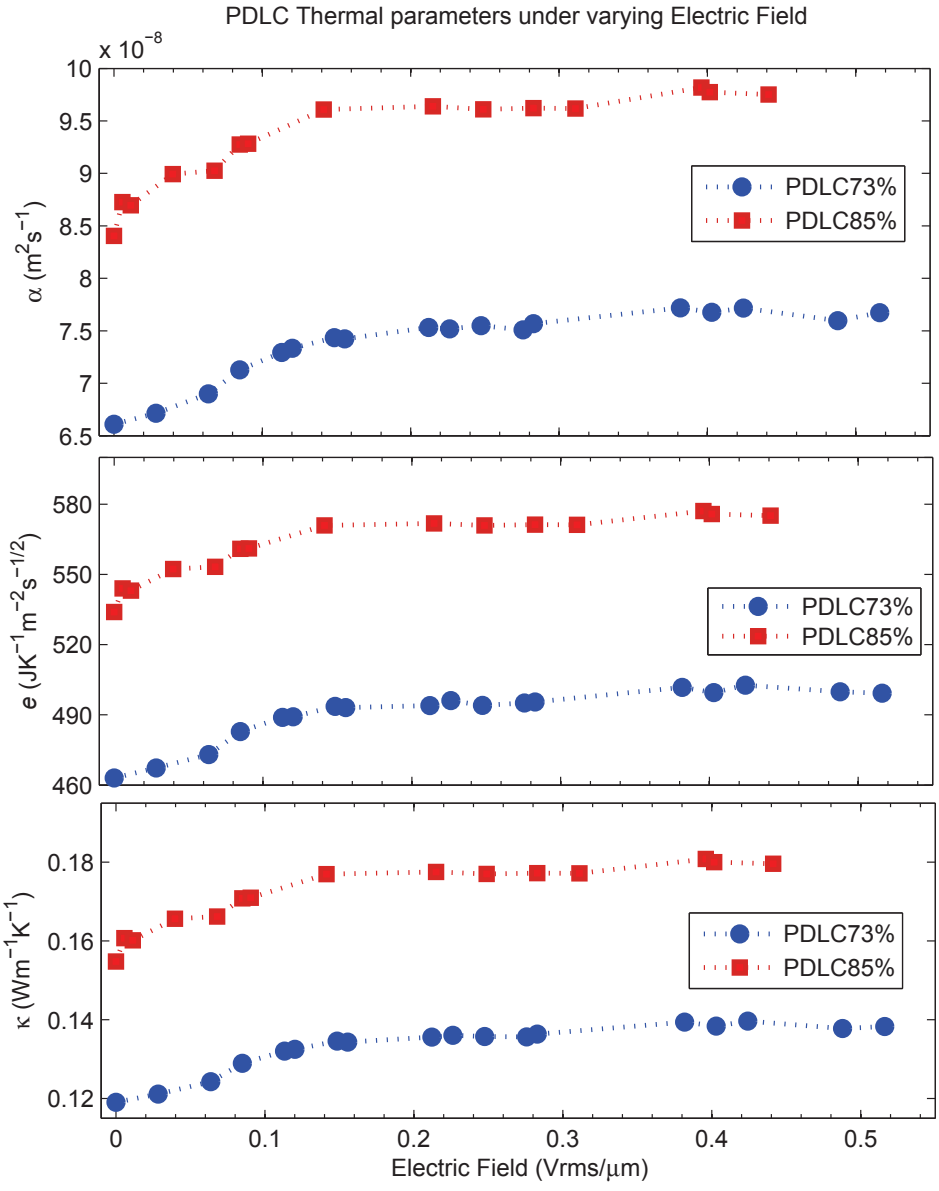

Figure 3.25: Variation of thermal diffusivity (top) , thermal effusivity (middle) and thermal conductivity (bottom) vs. varying electric field (at constant frequency (f_e), 1kHz) for PDLC samples (85% LC and 73% LC).

The PTR experiments were conducted by fixing the laser modulation frequency, f =

18Hz, at which the sample is in quasi-thermally thick regime, and varying EF strength successively. The displayed results are from the mean of three consecutive EF scans. We have also made an additional filtering by plotting volumetric heat capacity ($\rho C = e/\sqrt{\alpha}$) and by taking data points lie within ±1% or ±0.55% (depending on the population of experimental data points) from the linear fit value of ρC as shown in fig. 3.26. Here, the behaviour of ρC is independent of the applied electric field as expected. The molecular reorientation in LC do not make any contributions towards ρC and hence it stays unchanging. Nevertheless, liquid crystal concentration changes produce difference in ρC values.

The behaviour of the thermal conductivity (fig. 3.25) is intimately linked with the reorientation of molecules in LC droplets. At zero field, the symmetry axis of each LC droplet in the nematic phase varies randomly and for the heat entering the film, the effective thermal conductivity is reduced. At high fields, each droplet's symmetry axis is aligned with the external field which is parallel to the heat flow. The thermal conductivity of the droplets increases leading to an increase of the effective thermal conductivity of the PDLC film.

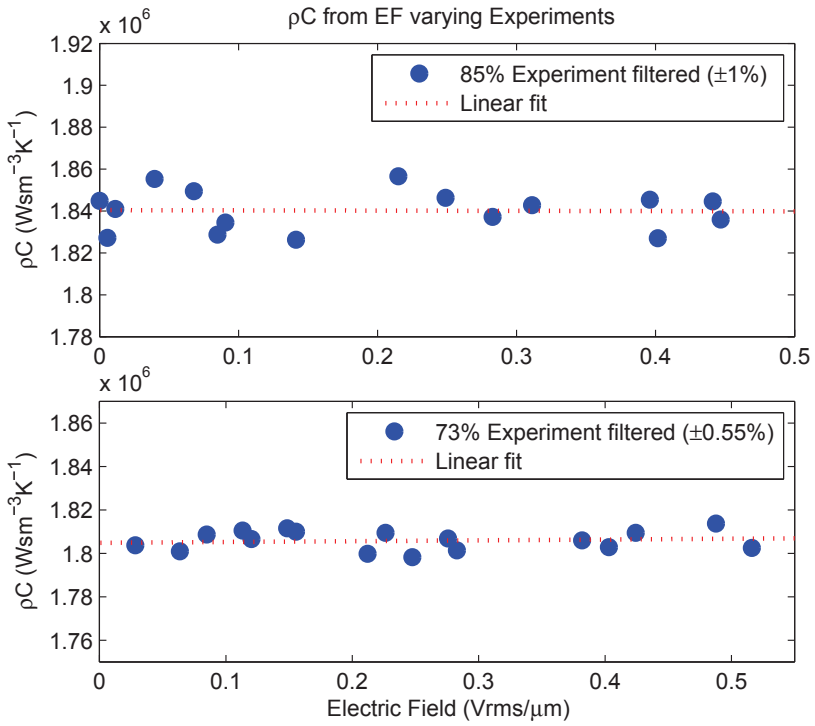

Figure 3.26: ρC plotted as a function of EF for both concentrations of PDLCs. Experimental data points shown are within ±1% for 85% LC and ±0.55% for 73% LC from the mean value of ρC.

3.3.4.1 Effective Medium Theory and Interfacial Thermal Resistance:

In all heterogeneous mixtures, thermal transport is hindered by interfacial boundaries. Nan *et al* [110] has given an estimation of effective thermal conductivity (κ_{PDLC}) of such heterogeneous mixtures with spherical inclusions on the basis of effective medium approach by taking into account of interfacial thermal resistance:

$$\kappa_{\mathrm{PDLC}} = \kappa_m \frac{\kappa_{\mathrm{LC}}(1+\gamma) + 2\kappa_m + 2\phi_{\mathrm{LC}}\left[\kappa_{\mathrm{LC}}(1-\gamma) - \kappa_m\right]}{\kappa_{\mathrm{LC}}(1+\gamma) + 2\kappa_m - \phi_{\mathrm{LC}}\left[\kappa_{\mathrm{LC}}(1-\gamma) - \kappa_m\right]} \tag{3.21}$$

where, $\gamma = r_k/r_d$, is the ratio of Kapitza radius (r_k) and mean droplet radius (r_d). κ_m and κ_{LC} are thermal conductivities of polymer matrix and LC respectively.

γ is a dimensionless parameter which compares the Kapitza radius r_k to the droplet radius r_d. The Kapitza radius is related to thermal interfacial resistance and describes the transition when interfaces begin to play a significant influence on the effective thermal conductivity of PDLC. When $\gamma \ll 1$ the influence of the interfaces may be ignored but if $\gamma > 1$ the contribution of the interfaces to the effective thermal conductivity becomes more important than that of the volume of the inclusions.

By knowing the thermal conductivities of polymer matrix and LC as well as by experimentally finding κ_{PDLC} and ϕ_{LC} (eq. (3.20)), one can calculate γ by rearranging eq. (3.21), which is given by:

$$\gamma = \frac{\frac{\kappa_m}{\kappa_{\mathrm{PDLC}}}\left(\kappa_{\mathrm{LC}} + 2\kappa_m + 2\phi\kappa_{\mathrm{LC}} - 2\phi\kappa_m\right) - \kappa_{\mathrm{LC}} - 2\kappa_m + \phi\kappa_{\mathrm{LC}} - \phi\kappa_m}{2\kappa_{LC} + \phi\kappa_{\mathrm{LC}} + 2\frac{\kappa_m\kappa_{\mathrm{LC}}}{\kappa_{\mathrm{PDLC}}}(\phi_{\mathrm{LC}} - 1)} \tag{3.22}$$

Equation (3.22) allows to compute r_k, once we know the mean radius of the droplets. Apparently, fig. 3.24 may not be sufficient to calculate the size of the droplets precisely. However, a rough estimation of droplet diameters lie around 1 to 5μm for 85% LC and 0.5 to 2μm for 73% LC, from the figure.

Nematic droplets in our system possess the bipolar configuration, at zero field the nematic is aligned tangentially at the droplet wall (fig. 3.27.a). Upon application of the field, the nematic within the center of each droplet aligns quickly with the field. This process leads to a droplet where the bulk of the nematic is aligned with the applied field, but near the wall of the droplet the nematic molecules are still aligned tangentially to the droplet surface (fig. 3.27.b). The orientation of the molecules along the surface of

the droplets remaining unchanged in the presence and in the absence of the electric field brought us to consider that the thermal interfacial resistance is constant and independent of the electric field. For calculating γ, we have used thermal conductivities when the LC molecules aligned in the direction parallel to the EF, at which $\kappa_{\mathrm{PDLC}} = \kappa_{\mathrm{PDLC}\|}$ and $\kappa_{\mathrm{LC}} = \kappa_{\mathrm{LC}\|}$.

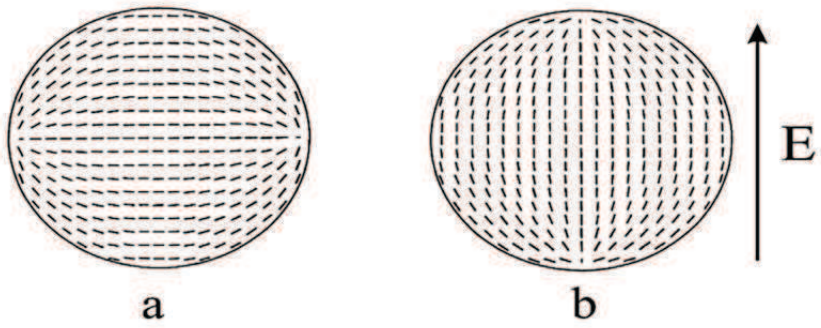

Figure 3.27: Schematic of nematic alignment in bipolar droplets (a) at zero field and (b) high field state.

Table 3.5: Physical properties of PDLC samples derived from EF varying experiments.

LC volume% (x)	$\kappa_{\mathrm{PDLC}\|}$	$\kappa_{\mathrm{LC}\|}$	ϕ_{LC}	γ	r_d (μm)
85%	0.18	0.24*	0.78	0.079	0.5/2.5
73%	0.138	0.24*	0.55	0.178	0.25/1

* Reference [85]

Table 3.5 contains the thermal conductivity values used for calculations and the results obtained for γ values. These values, less than unity, are indicating that the volume of the LC droplets are involved in the thermal transport. Moreover it is less prominent in 73% LC sample where γ shows higher value than 85% LC sample. Apparently, due to the reduction in droplets' sizes at lower LC concentrations, increase the ratio, γ, for the same Kapitza radius values. Interestingly, these values are comparable to the one found previously for PS-5CB composites [23].

Above results are indicating the thermal transport inside PDLCs are influenced both by the applied electric field and the average droplet size. It is also noteworthy that, both the other dynamic thermal parameters, diffusivity and effusivity, shows the same trend as

the thermal conductivity does, thus giving an opportunity to study the thermal behaviour of these samples by finding any one of these thermal parameters.

3.3.5 PDLC Under Frequency Varying Electric Field

3.3.5.1 Experimental Results on PDLCs as function of Frequency

Subsequently, we have investigated the polarization field effects in PDLC samples due to interfacial polarisation at polymer-LC boundaries.

Figure 3.28 shows the variation of thermal parameters of PDLC sample with 85% LC as a function of f_e at constant EF of 0.127 V/μm. The results are obtained from the mean of four f_e scans (upper plots), done at 18, 20, 22 and 30 Hz of laser modulation frequencies. In order to smooth the obtained results, we have plotted volumetric heat capacity (ρC) (fig. 3.29) and took the points lie within $\pm$0.65% from the mean value. The parameter, ρC is not affected by the orientation of the LC molecules. So the EF as well as the the frequency dependent EF do not change the volumetric heat capacity of the samples.

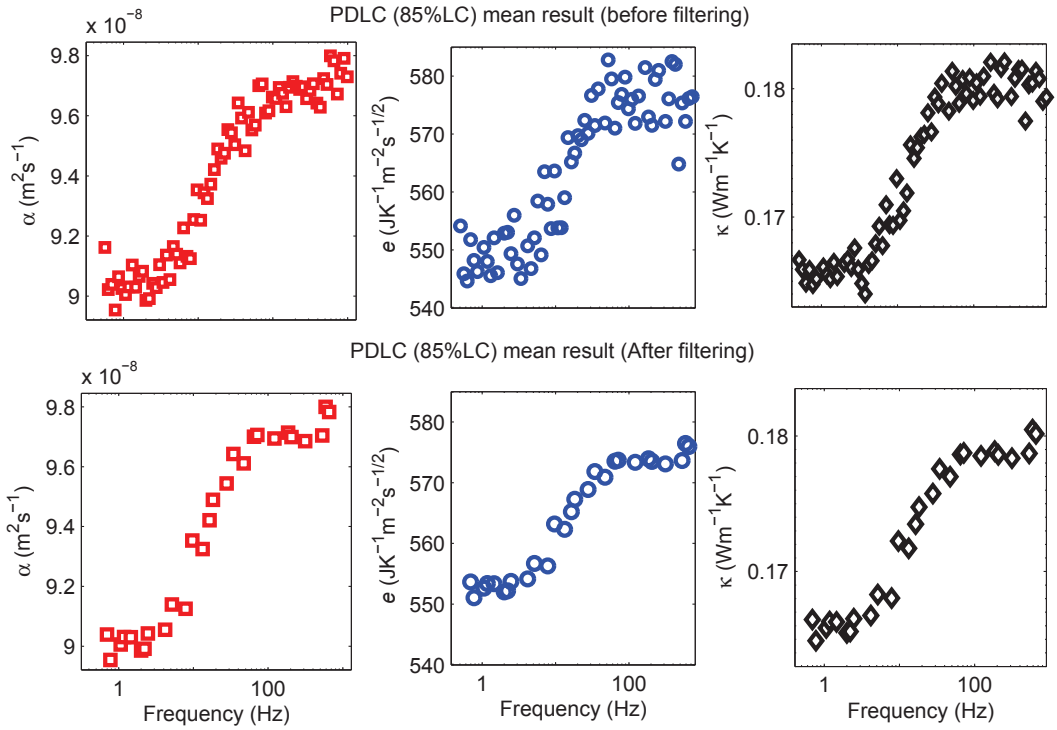

Figure 3.28: PDLC thermal diffusivity (left), effusivity (middle) and conductivity (right) vs. f_e. Results obtained from the mean of four f_e scans (upper plots), done at 18, 20, 22 and 30 Hz laser modulation frequencies and at constant electric field of 0.127 V/μm. These are further filtered (lower plots) by plotting ρC and taking points within $\pm$0.65% from the mean value.

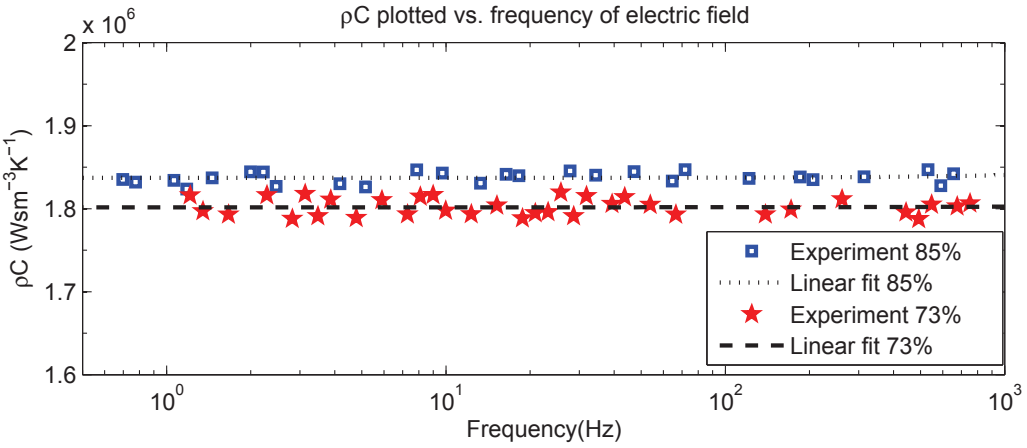

Figure 3.29: ρC plotted for both PDLC samples vs. frequency of applied electric field.

Results on thermal parameters as a function of f_e for PDLC with 73% LC are displayed in fig. 3.30. Here the results are obtained by taking the mean of three f_e scans at same laser modulation frequency and further plotted the volumetric heat capacity (fig. 3.29) and filtered out the points lie outside $\pm 0.9\%$ of the ρC mean value. Results on 73% LC samples are also consistent with the behaviour of ρC as expected.

Both results, from 73% and 85% PDLC samples, are clearly showing the frequency dependence of the dynamic thermal properties of PDLC samples. At higher frequencies, the charge accumulation at the LC-polymer interfaces due to the mobility of free charges (conductivity effect) are interrupted and the effect of depolarisation field vanishes. This makes the molecules better aligned in the direction of the EF and hence the thermal transport also increases and reaches its maximum. On the other hand, at lower frequencies, the dominant depolarisation field diminish the electric field inside the droplets (E_{drop}) and it worsen molecular alignment which lower the heat flow normal to the surface of the PDLC material [102].

Figures 3.30 and 3.28 are evidencing for the first time to the best of our knowledge the MWS effect via the thermal properties of PDLC materials.

3.3.5.2 Effective Thermal Conductivity of LC Droplets

Originally, the change in effective thermal conductivity of PDLCs come from the reorientation of the liquid crystal droplets inside the PS matrix. Therefore, using eq. (3.21), one

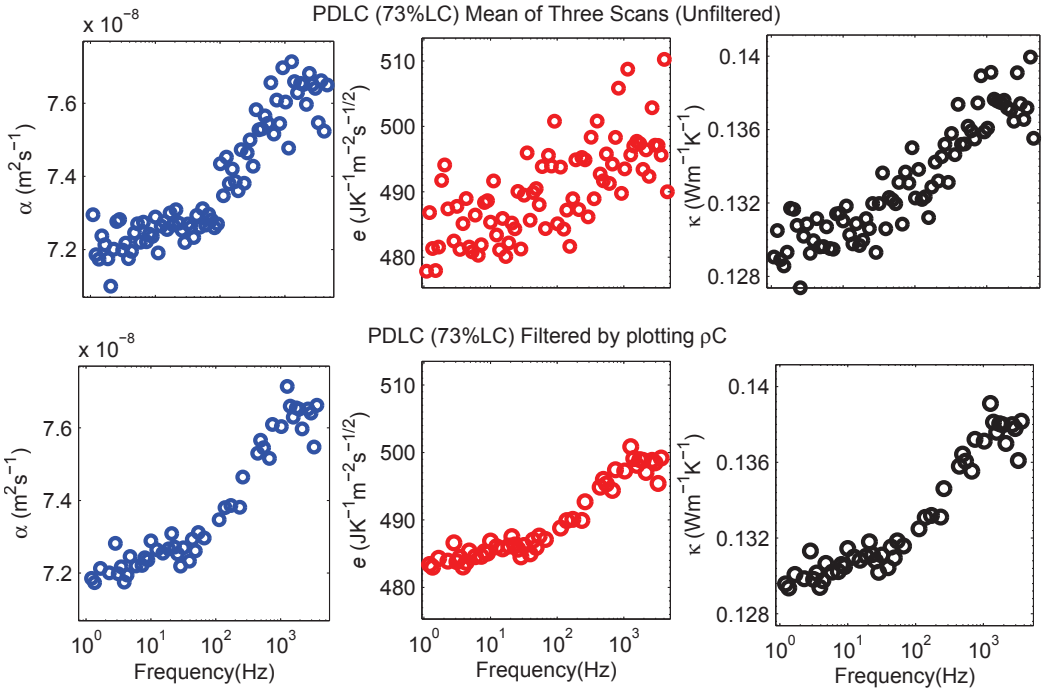

Figure 3.30: PDLC thermal diffusivity (left), effusivity (middle) and conductivity (right) vs. Frequency of electric field. Results are obtained from the mean of three scans (upper plots), done at 18 Hz laser modulation frequency and at constant electric field of 0.18 V/μm. Filtered results (lower plots) are obtained by plotting ρC and taking points within $\pm 0.9\%$ from the mean value.

can estimate the mean thermal conductivity of LC droplets, given by:

$$\kappa_{\mathrm{LC}} = \frac{\kappa_m \left[2\kappa_m \left(1-\phi\right) - \kappa_{\mathrm{PDLC}} \left(2+\phi\right)\right]}{\kappa_{\mathrm{PDLC}} \left[\left(1+2\gamma\right) - \phi\left(1-\gamma\right)\right] - \kappa_m \left[1+2\gamma+2\phi\left(1-\gamma\right)\right]} \tag{3.23}$$

Evolution of the mean thermal conductivity of LC droplets, κ_{LC}, for PDLC samples of 73%LC and 85% LC are shown in fig. 3.31. Calculations are done using the previously obtained γ and ϕ_{LC} values from table 3.5.

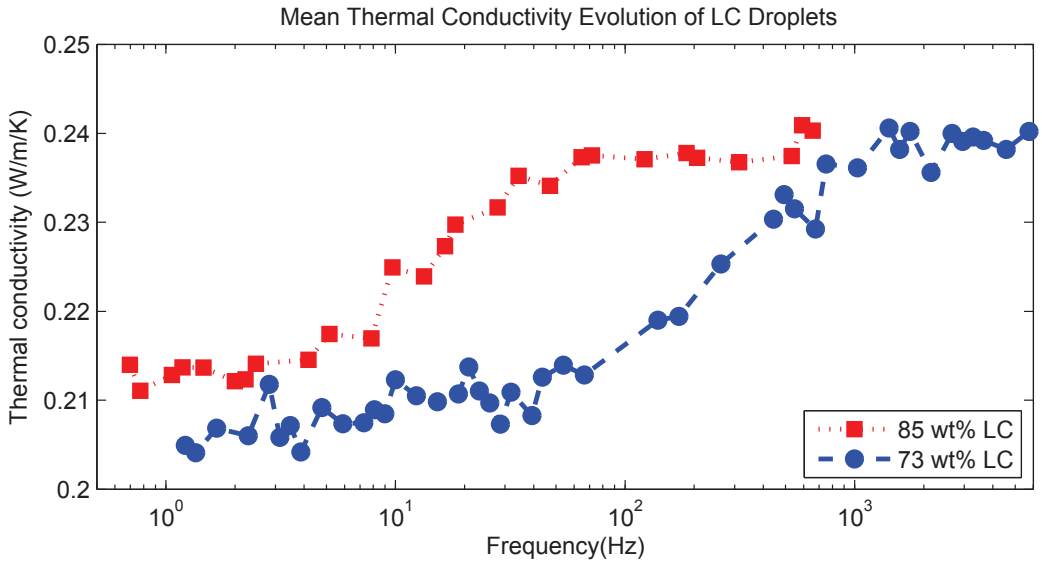

Figure 3.31: Thermal conductivity of the confined liquid crystal as a function of frequency of the applied electric field. Squares are showing the results on 85% LC and circles represents 73% LC.

Considering $\kappa_{\mathrm{LC}\perp}$ and $\kappa_{\mathrm{LC}\parallel}$ the thermal conductivity perpendicular to or along the molecular long axis, and θ- the angle between this long axis and a given direction (fig. 3.32), the thermal conductivity along this direction may be express as:

$$\kappa_{\mathrm{LC}} = \kappa_{\mathrm{LC}\parallel}\cos^2\theta + \kappa_{\mathrm{LC}\perp}\sin^2\theta \tag{3.24}$$

Using the values of $\kappa_{\mathrm{LC}\parallel}$ and $\kappa_{\mathrm{LC}\perp}$, the variation in orientation angle, θ, can be extracted from the thermal conductivity experimental data:

$$\theta = \mathrm{asin}\sqrt{\frac{\kappa_{\mathrm{LC}} - \kappa_{\mathrm{LC}\parallel}}{\kappa_{\mathrm{LC}\perp} - \kappa_{\mathrm{LC}\parallel}}} \tag{3.25}$$

Figures 3.33 and 3.34 are showing the variation of equilibrium angle of the directors, θ, of LC droplets for both samples as a function of frequency of the applied electric field. Evaluating the evolutions of θ in conjunction with the variations of κ_{LC} (fig. 3.31) reveal

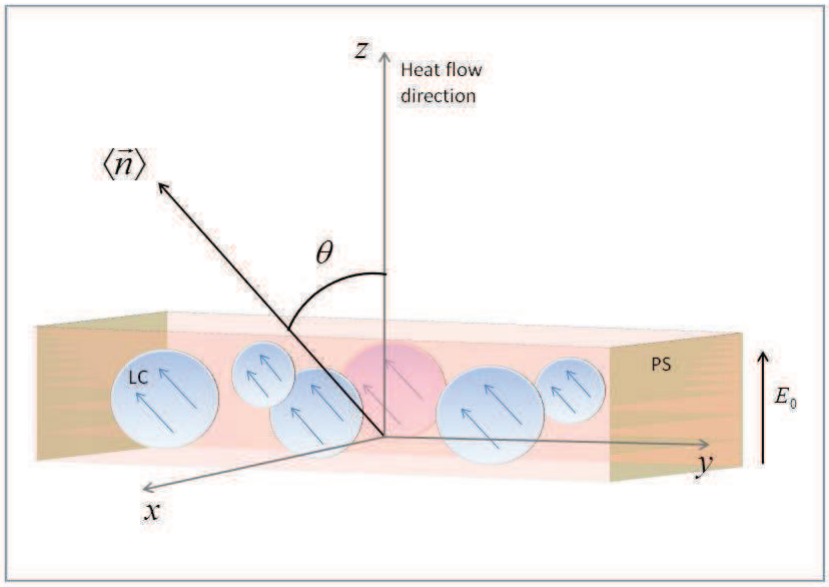

Figure 3.32: Orientation of LC droplets inside PDLC. θ is showing the average orientation of LC molecule long axis with respect to the heat flow direction.

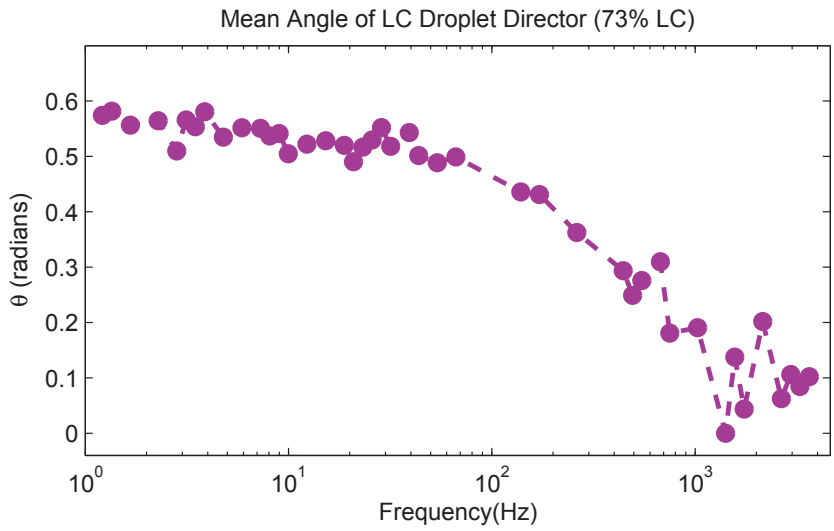

Figure 3.33: Angle (in radian) of the director with respect to heat flow direction as a function of frequency of the applied electric field for 73% LC sample.

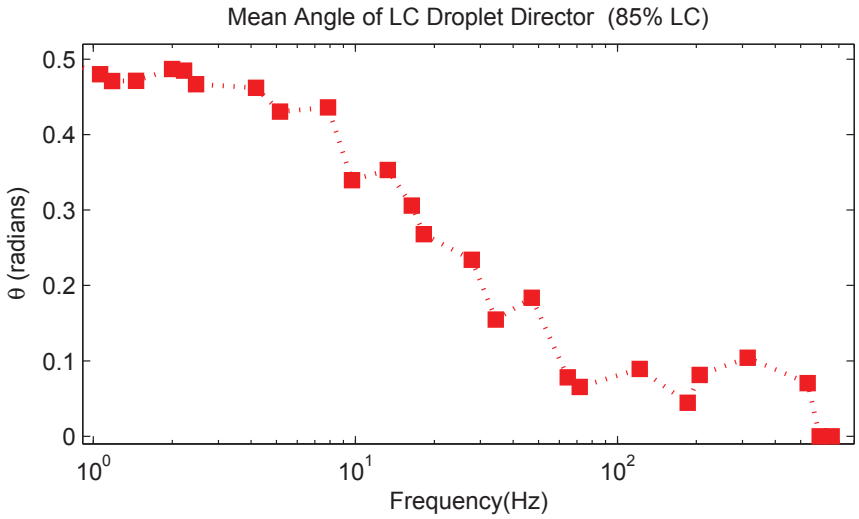

Figure 3.34: Angle (in radian) of the director with respect to heat flow direction as a function of frequency of the applied electric field for 85% LC sample.

the stamped down variations of thermal conductivity values in both samples.These frequency behaviour of PDLC contains informations on several physical phenomenon. In the subsequent sections, we have used the obtained results on θ and κ_{LC} for finding different physical parameters.

3.3.5.3 Frequency Dependent Thermal Conductivity and MWS Effect

The relation between droplet electric field, E_{drop}, and the angle of molecular orientation, θ, is given by[102] :

$$2\cos^2\theta = 1 + \frac{e^2 - 1 + 2\cos^2\psi}{\sqrt{(e^2-1)^2 + 4e^2\cos^2\psi}} \tag{3.26}$$

where, ψ is the equilibrium angle of the droplet directors at zero electric field obtained from EF varying experiments (values are displayed in table 3.6), e is the reduced field parameter and which can be expressed as: $e = E_{drop}/E_0$ and E_0 is the threshold reorientation electric field. E_0 can be defined as the electric field necessary to reorient LC molecules in its direction (threshold electric field). Its value depends on the droplet radius (r_d), elastic constant (K) and the dielectric anisotropy ($\Delta\epsilon$) of the LC material. ϵ_0 is the permittivity of free space (8.85×10^{-12} F/m). The relation for E_0 is given by [102]:

$$E_0 \approx \frac{1}{r_d}\sqrt{\frac{K}{\epsilon_0\Delta\epsilon}} \tag{3.27}$$

In order to determine the effective thermal conductivity variations of PDLCs as a function of frequency of the applied electric field, one can insert the equation for $E_{drop}(f_e)$ (eq. (3.17)) into the equation for the angle of reorientation (θ, eq. (3.26)), the resultant then put into the expression for LC droplet thermal conductivity (κ_{LC}, eq. (3.24)) and finally to the expression for $\kappa_{\mathrm{PDLC}}(f_e)$ (eq. (3.21)), as shown below:

$$E_{drop}(f_e) \overset{\text{Eq. (3.17)}}{\rightarrow} \theta \overset{\text{Eq. (3.26)}}{\rightarrow} \kappa_{\mathrm{LC}} \overset{\text{Eq. (3.24)}}{\rightarrow} \kappa_{\mathrm{PDLC}}(f_e)$$

The outcome of the above relation for $\kappa_{\mathrm{PDLC}}(f_e)$ can be used to model the frequency dependent effective thermal conductivity results of PDLC samples (figures 3.30 and 3.28) to find electrical parameters of LC and polymer matrix as well as the threshold electric field E_0.

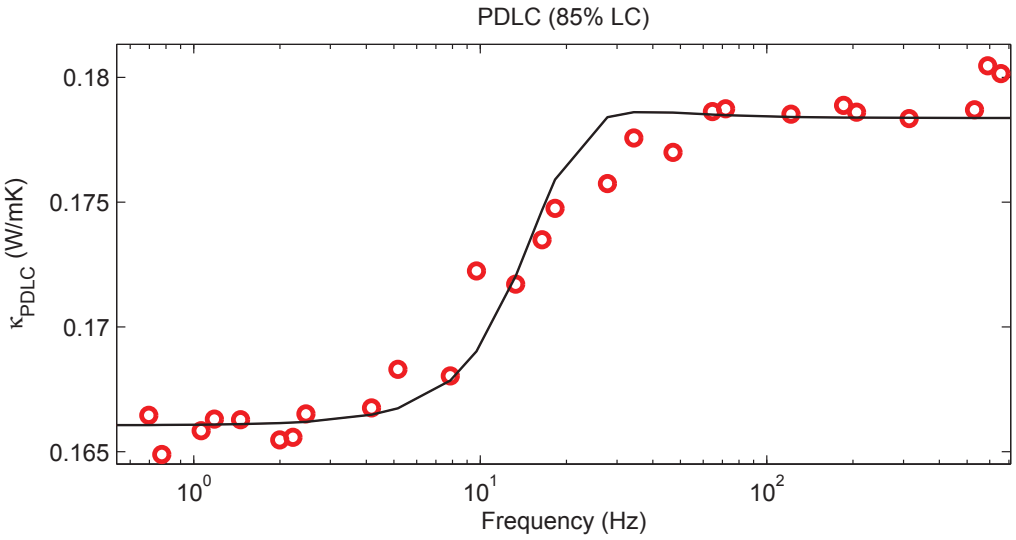

Figure 3.35: PDLC 85% LC experimental data (circle) and theoretical fit (full line).

Table 3.6: Electrical parameters of PDLC samples from MWS fit.

x	ψ (rad.)	σ_M (S/m)	σ_{LC} (S/m)	E_0 (V/m)	f_0(Hz)	E_a (V/m)
85%	0.6	$(1.27\pm0.09)\times10^{-9}$	$(4.9\pm0.3)\times10^{-8}$	$(6.8\pm0.3)\times10^{4}$	21 ± 2	1.27×10^{5}
73%	0.9	$(3.5\pm0.1)\times10^{-8}$	$(4.8\pm0.1)\times10^{-7}$	$(7.2\pm0.1)\times10^{4}$	221 ± 5	1.80×10^{5}

Figures 3.35 and 3.36 are showing the experimental results (circles) and the best fits (full line) on effective thermal conductivity (κ_{PDLC}) variations of PDLC 85% LC and 73%

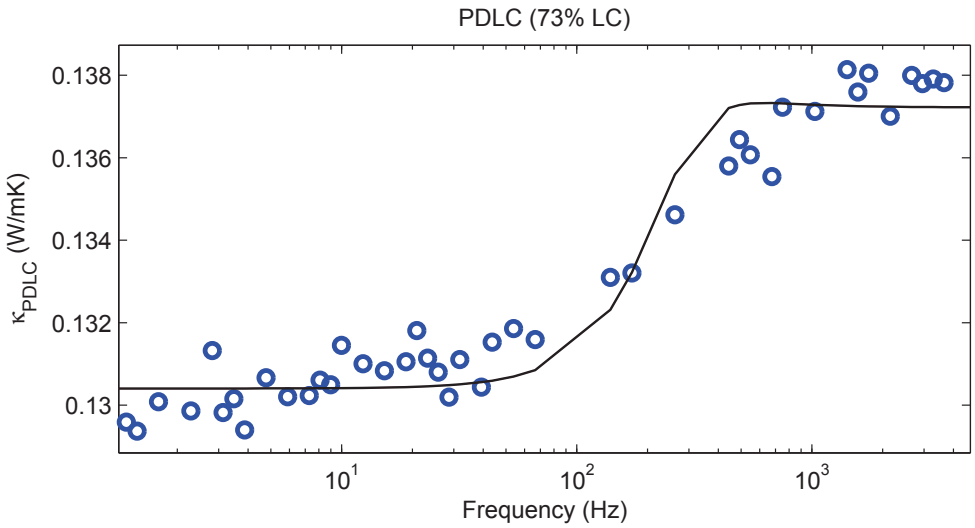

Figure 3.36: PDLC 73% LC experimental data (circle) and theoretical fit (full line).

LC respectively as a function of frequency. The values of the EF were chosen from a previous electric field scan (fig. 3.25) so that the LC molecules were aligned parallel to the EF at a frequency high enough to nullify the MWS effects. During the fitting procedure, E_0 as well as electrical conductivities of both the polymer matrix and LC were kept as free parameters. Values of the materials' dielectric properties were taken from literatures. The results obtained from fitting are displayed in table 3.6.

Figure 3.37 contains the simulated plots for 85% LC and 73% LC samples having the values used in or obtained from the theoretical fitting of the experimental data. These plots show the evolutions of E_{drop} and κ_{PDLC} for both samples. The threshold electric fields (E_0) and the corresponding frequencies (f_0) are also labelled inside the plots and also included in table 3.6. The electrical parameters for 85% LC found from fitting are in good agreement with the values found in literatures (ref. section 3.3.2). While for 73% LC sample, the results are showing relatively higher values than reported. One of the reasons for this difference could be due to the possible variations in the solubility limit of the LC. In addition, the system properties are vulnerable to change during the course of time, temperature and synthesizing conditions.

The main interesting parameter in our study is the threshold field (E_0)or frequency (f_0). These values are indicating the necessary field needed to align the LC molecules in the direction of the applied EF. Obviously, the values of these parameters increase with decreasing LC concentration. This behaviour is expected since the droplet size decreases

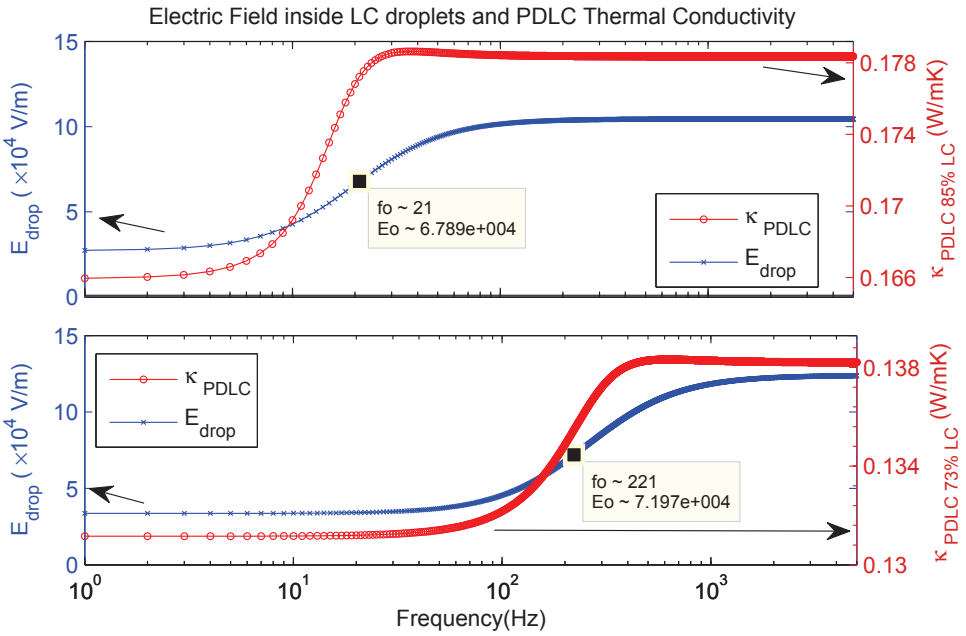

Figure 3.37: Simulations on E_{drop} and κ_{PDLC} with values used and obtained in fitting for PDLC 85% LC (upper plot) and PDLC 73% LC (lower plot).

with decreasing concentration and thus the field across the droplet must be higher for aligning the molecules. In the case of f_0, the depolarisation field increases with decreasing frequency thus the equivalent field acting on the droplets is linear to the applied frequency.

Table 3.7: Elastic constants for the PDLC samples.

x	$\Delta\epsilon$	$r_d(\mu\mathrm{m})$	E_0 (V/m)	K (N)
85%	10	0.5/2.5	$(6.8\pm0.3)\times10^4$	$9.4\times10^{-14}/2.8\times10^{-12}$
73%	10	0.25/1	$(7.2\pm0.1)\times10^4$	$2.8\times10^{-14}/4.7\times10^{-13}$

We can also deduce the elastic constant, K, knowing E_0 and the droplet radius using eq. (3.27). Values found for K for both of the PDLC samples are displayed in table 3.7. These effective values of elastic constants govern the interaction between the anchoring forces at the droplet-polymer boundaries, which make the droplet to be aligned in a particular direction, and the elastic forces acting in the bulk of the LC droplet. The studied samples are showing the values of K lower than that the value reported for bulk nematic 5CB ($4.1\mathrm{x}10^{-12}$) [111]. This is attributed due to the increased anchoring forces at the LC-polymer boundaries. Apparently, the K values are more closer and even similar for the

biggest droplets in the case of 85% LC to the reported bulk values, where the molecules available away from the boundaries are higher than 73% LC sample.

3.4 Summary of the Experimental Results on Liquid Samples

We have explored the ability of photothermal infrared radiometry for studying thermal properties of liquid samples and demonstrated its capability to give results with high accuracy. The two presented configurations are described theoretically followed by experimental results. BF-PTR gives the absolute thermal diffusivity of a sample knowing only the sample's thickness and also the result is independent of the thermal parameters of surrounding layers. B-PTR configuration has the potentiality of finding two thermal parameters simultaneously. Both the Back signal detection involved configurations, B-PTR and BF-PTR, posses high sensitivity to the thermal parameters of the sample and can yield results from a single modulation frequency. This is particularly helpful for finding thermal properties in temperature or time varying experiments. We have done experiments with known samples and found a very good agreement with already reported values of thermal parameters.

The newly developed PTR methods for thermal characterization of liquid samples are used to investigate the variation of thermal transport properties due to the polarization effects on PDLC samples. Results on thermal properties as a function of frequency dependent electric field on PDLC samples are clearly showing the polarization field effects on their thermal properties. These results are further analysed and modelled against existing MWS model and deduced their elastic and electrical properties from the experimentally found thermal informations.

Chapter 4

Thermal Characterization of Thermoelectric Polymer-Nano Composites using A Novel Photothermoelectric (PTE) Technique

4.1 Introduction

Certain materials produce an electrical potential difference when they are subjected to a temperature gradient [112]. This phenomenon is called Seebeck effect and these solid-state materials are called thermoelectric (TE) materials. Even though, at present, TE materials are less efficient than other energy harvesting systems like photovoltaic, they have attracted the scientific community over the past decades [29]. New interests on TE materials started since the theoretical predictions suggested that the thermoelectric efficiency could be strongly improved with nano-structuring [113, 114, 115, 116]. The performance depends mainly on the dimensionless quantity called figure of merit $ZT = \frac{S^2\sigma}{k}T$, where S, σ, κ, T are the Seebeck coefficient, electrical conductivity, thermal conductivity and the absolute temperature. Polymer thermoelectrics are new class of materials interestingly emerged out after the finding of electrically conducting doped polyacetylene [117]. Since

these materials are cost effective and easily processable than the conventional 'state of the art' metal/semiconductor composite materials [118], a renewed interests on polymer thermoelectrics arise to improve their efficiency.

Here, our experimental studies are focused on the investigation of thermal transport properties of thermoelectric materials, in which, the characterisation of Polyaniline (PANI) -Carbon Nanotube (CNT) nanohybrids, prepared using a novel approach called CNT-templated polymerization process, are being analysed. Carbon nanotubes used for experiments are either oxidized or unoxidized, single- or multiple-walled, and the as prepared hybrids exhibit cable-like morphology with CNTs as cores, wrapped by nanofibrous polyaniline (PANI) [22].

In this work, we introduce, for the first time, a novel application of the thermoelectric effect as a means to investigate the thermal properties of both TE and other materials by using TE materials as sensors. All the presented results, in this chapter, are obtained by the newly developed photothermoelectric technique (PTE), where the samples themselves serve as sensors. Results obtained from PTE measurements are then being compared with those retrieved from conventional photothermal radiometry (PTR) as a validation of the PTE technique.

Furthermore, we have used PTE technique for the thermal characterization of solid samples. Here, the TE material as a PT sensor operate under two configurations: (i) Front-PTE (FPTE), and (ii) Back-PTE (BPTE).

4.2 A Novel PhotoThermoElectric Technique (PTE)

The potential difference (ΔV) between two points of a thermoelectric material can be described by the following relation provided that the temperature fluctuations are weak:

$$\Delta V = S \int_{T_{z=d}}^{T_{z=0}} dT \qquad (z \leq 0) \tag{4.1}$$

with, d is the thickness of the sample in the negative z-direction, $T_{z=0}$ and $T_{z=d}$ are the temperature at the surface $z = 0$ and at thickness $z = d$ respectively. S is considered as constant for small temperature variations. Figure (4.1) depicts the experimental configuration. Upon integrating eq. (4.1) gives:

$$\Delta V = S\left[T(z=0) - T(z=d)\right] \tag{4.2}$$

Referring back to the derived expressions in chapter 2 for the temperature fields for an optically opaque sample of thickness d in contact with a semi-infinite substrate and air as the top layer (*layer-0*), excited by a modulated laser beam is given by, including the terms for convection heat transfer loss(H_1) [119]:

$$T(z,\omega) = \frac{I_0(1+H_1)}{4k_1\sigma_1}\left[\frac{1+\Re_2\exp(-2\sigma_1(d+z))}{1-H_1\Re_2\exp(-2\sigma_1 d)}\right]\exp(\sigma_1 z) \qquad (z\leq 0) \tag{4.3}$$

where I_0, k_1, $\Re_2$ and σ_1 are intensity of the incident radiation, sample's thermal conductivity, thermal wave reflection coefficient (eq. (2.42)) and the complex thermal wave number (eq. (2.17)) respectively, as mentioned earlier.

H_1 is a parameter depending on convection coefficient h_1, followed by the relation:

$$H_1 = \frac{k_1\sigma_1 - h_1}{k_1\sigma_1 + h_1} \tag{4.4}$$

It should be pointed out that h_1 can be neglected for a given sample for high frequency. In the following section 4.2.1 we have carried out simulations to show the suitable frequency range where h_1 can be neglected. By equating eq. (4.3) into eq. (4.2) and after rearranging, the potential difference between the two surfaces can be expressed as:

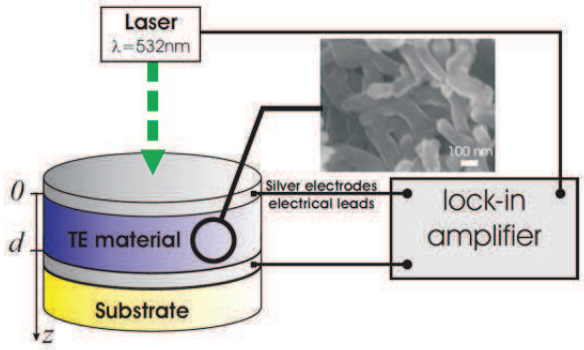

Figure 4.1: Investigated sample configuration

$$\Delta V = \frac{SI_0(1+H_1)}{4k_1\sigma_1}\left[\frac{1+\Re_2\exp(-2\sigma_1 d)-(1+\Re_2)\exp(-\sigma_1 d)}{1-H_1\Re_2\exp(-2\sigma_1 d)}\right] \tag{4.5}$$

The normalized signal is obtained by realising frequency scans with separate substrates, e.g., air and glycerol. When the substrate is air, $\Re_2$ becomes $\Re_0$ (eq. (2.42)) and the voltage difference is given by:

$$\Delta V_0 = \frac{SI_o(1+H_1)}{4k_1\sigma_1}\left[\frac{1+\Re_0\exp(-2\sigma_1 d)-(1+\Re_0)\exp(-\sigma_1 d)}{1-H_1\Re_0\exp(-2\sigma_1 d)}\right] \tag{4.6}$$

Further, considering that the thermal transport by conduction largely outweighs the thermal transport by convection, the real part of $k_1\sigma_1 \gg h_1$, then the quantity H_1 can be

approximated to 1 and also, since the air effusivity is too low $\Re_0 \approx 1$. Then the normalized voltage V_n, obtained by dividing ΔV with ΔV_0 is given by, after simplification:

$$V_n = \frac{\Delta V}{\Delta V_0} = 1 + \frac{(1 - \Re_2)\exp(-\sigma_1 d)}{1 - \Re_2 \exp(-2\sigma_1 d)}. \tag{4.7}$$

Apparently, the phase (normalized phase) from eq. (4.7) decreases with frequency and becomes zero for a first time at a value $d/\mu_1 = \pi$. Thus, the thermal diffusivity of the sample, α_1, can be extracted from, as previously reported for photopyroelectric techniques [120]:

$$\alpha_1 = \frac{d^2 f_0}{\pi}, \tag{4.8}$$

where, f_0 is the zero crossing frequency. Knowing α_1, the thermal effusivity can be obtained after some rearrangements of eq. (4.7):

$$e_1 = e_2 \frac{1 + \Re_2}{1 - \Re_2}. \tag{4.9}$$

where, $\Re_2$ is given by:

$$\Re_2 = \frac{(V_n - 1) - \exp(-\sigma_1 d)}{(V_n - 1)\exp(-2\sigma_1 d) - \exp(-\sigma_1 d)}. \tag{4.10}$$

Therefore, both thermal parameters of the TE sample (as sensor) can be determined either by a direct least squares fitting of eq. (4.7) to experimental data or analytically using eqs. (4.8), (4.9) and (4.10) provided that the effusivity of backing is known.

4.2.1 Simulations on Convection Effects and Sensitivity

Due to the poor thermal conductivity of polymers, the measurements need to be carried out at lower frequencies, meaning that convection effects can not be neglected. In order to take into account of this phenomenon, the influence of the convection effect on the PTE signal is investigated numerically.

Figure 4.2 shows the evolution of the normalized phase vs. reduced parameter d/μ_1, where μ_1 is the thermal diffusion length. h_1 is varied for values 0, 10 and 100 $\mathrm{Wm^{-2}K^{-1}}$ keeping $\Re_2$ fixed at -0.2. It is apparent that, above $d/\mu_1 = 1$, convection has little or no effect on the normalized signal, thus the eq. (4.7) without convection factor is valid for

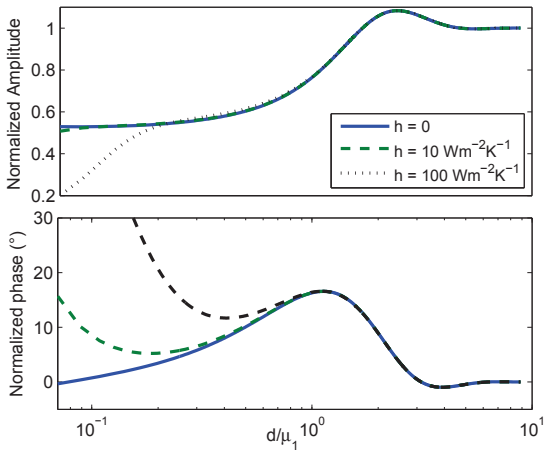

Figure 4.2: Dependence of normalized signal evolution vs. reduced thermal parameter d/μ_1 for different values of convection coefficient plotted with fixed $\Re_2$=-0.2. Upper plot showing the normalized amplitude and lower one is the phase difference

$d/\mu_1 \geq 1$. For $d/\mu_1 < 1$, convection cannot be neglected and the equation including H must be used.

Figures 4.3 -(a & b) are showing the sensitivity of experimental signal vs. d/μ_1 for various values of $\Re_2$ for a 1% change in thermal diffusivity. The sensitivity increases with decreasing $\Re_2$ value, indicating that a substrate with high effusivity need to be used for the determination of the thermal diffusivity. While in the case of sensitivity studies on effusivity variations, the best frequency range found is $0.5 \leq d/\mu_1 \leq 2$ (fig. 4.3 -(c & d) plotted with 1% change in e_1 around each $\Re_2$ values keeping zero percentage change in α_1). However, in order to avoid convection during experiments, the frequency scans are restricted to $d/\mu_1 \geq 1$, limiting the available frequency range to $1 \leq d/\mu_1 \leq 2$. As expected, sensitivity on thermal effusivity increases when the thermal effusivity contrast increases, means $\Re_2$ goes far from 0.

4.2.2 Experimental Results using PTE technique

4.2.2.1 Intrinsically Conducting Polymers

Polymer composite materials identifies as an indispensable stuff in our scientific arena. It creates a new distinguished class of material, which are light in weight and mechanically stronger in utility. The ease of preparation and possibility of reprocessing opens cost effective solutions for many applications using polymer composites. Polymers were previously

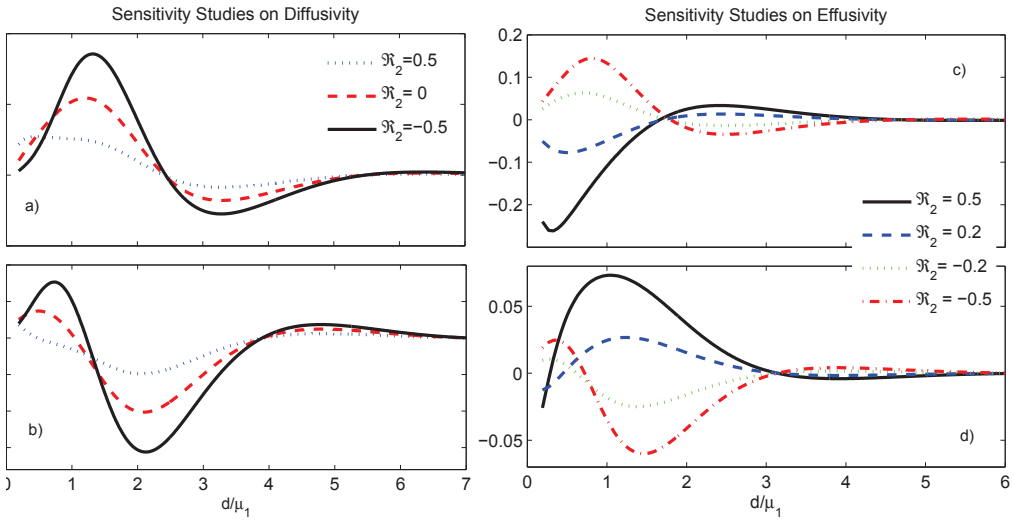

Figure 4.3: Simulations for the variation of normalized amplitude in percentage (a & c) and phase difference in degree (b & d) vs. d/μ_1 for various $\Re_2$ values. In a & b the thermal diffusivity (α_1) is varied 1% for all the plots. For c & d, 1% change in e_1 is introduced around each $\Re_2$ values while keeping 0% change in α_1. Values used for simulations are: $\alpha_1 = 3.2 \times 10^{-7}$ $\mathrm{m^2 s^{-1}}$, $e_1 = 1184$ $\mathrm{Jm^{-2}K^{-1}s^{-1/2}}$, d =200μm and $e_2 = 1581$ $\mathrm{Jm^{-2}K^{-1}s^{-1/2}}$

known as electrically insulting materials until the recent findings of appreciable electrical conductivity in them. This circumstantial findings lead to the developments on using such intrinsically conducting polymers (ICPs) as bio-materials [121], actuators [122], fabrics [123], corrosion inhibitors [124], in electronics [125], organic LEDs and PVs, charge dissipating (antistatic) layers and chemical sensor research. ICPs are polymers with extended π-conjugation along the molecular backbone. Their conductivity can be changed by several orders of magnitude from a semiconducting state to a metallic state by doping. Usually p-doping is achieved by partial oxidation of the polymer by a chemical oxidant or an electrochemical method, and causes depopulation of the bonding π orbital (HOMO) with the formation of "holes" [126]. The possibility of generating electricity [3, 127, 128] due to its thermoelectric (TE) properties, based on the Seebeck effect (property of a material to generate a potential difference between the ends when it is subjected to a temperature difference at those ends), is also a live research area. The conversion efficiency of thermo-electricity generation is governed by the dimensionless quantity known as figure of merit, $ZT = S^2\sigma T/\kappa$. Here S, σ, T and κ are the Seebeck coefficient(V/K), electrical conductivity(S/m), absolute temperature(K) and thermal conductivity(W/mK) respectively. Until now, metallic or semi-metallic composites are showing the best ZT and the highest

reported value is about 2.2 [129] at around 900^0C. Even though these ZT values are far below in comparison with the equivalent efficiency of compressor type cooling systems. This restricts the use of TE materials from efficient application oriented implementations. The class of polymer thermoelectrics have even lower ZT values, typically < 1. Even though, a significant interest on TE research stems on the solid state and cost effective energy conversion possibility and waste heat recovery advantages. Thus many of the researchers are being focused on improving the ZT values of both types (polymer and metallic) of TE materials by hoping on different theoretical predictions and possibilities such as nano structuring, doping etc. to increase S, σ and/or to decrease κ. Recent studies on conducting polymers have shown improved ZT values on the tailor-made polymer nano-composites than pure polymers. These composites exhibit high electrical conductivities, depending on the amount of nano inclusions, without a major increase in thermal conductivity.

4.2.2.2 Sample Preparation

The TE samples are pressed pellets (diameter: 13 mm) of Methanesulfonic acid (CH_3SO_3H) doped nanofibrous Polyaniline (PANI) used as sheath to wrap CNT core yielding nanostructured composite materials (Fig. 4.1). The Carbon Nanotubes (CNT) mass fraction is $\approx$ 6.6 wt-%. Four composites are investigated: PANI-CH_3SO_3H/unoxidized Single-Walled Carbon Nanotubes (PANI/unoxSWNT), PANI-CH_3SO_3H/unoxidized Multi-Walled Carbon Nanotubes (PANI/unoxMWNT), PANI-CH_3SO_3H/oxidized SWNT (PANI/oxSWNT) and PANI-CH_3SO_3H/oxidized MWNT (PANI/oxMWNT). Details of sample pellet processing are described elsewhere [22]. Each surface of the pellets were covered with a sputtered silver electrode on which electrical leads were silver pasted and plugged into an EG&G 7260 lock-in amplifier (Fig. 4.1). Figure 4.4 shows the SEM images of each samples of polyaniline-CNT nano hybrides. These images are confirming that the in situ polymerization of aniline has been taken place and as grown PANI-CNTs evidently forming fibrous hybrids with a minimum size bigger than the smallest nanotube diametrically. The longer lengths of all the hybrid nano fibres (fig. 4.4 b,c,d,e) than the pristine PANI fibres (fig. 4.4 a) are also justifying the guided growth of PANI along the CNT backbone.

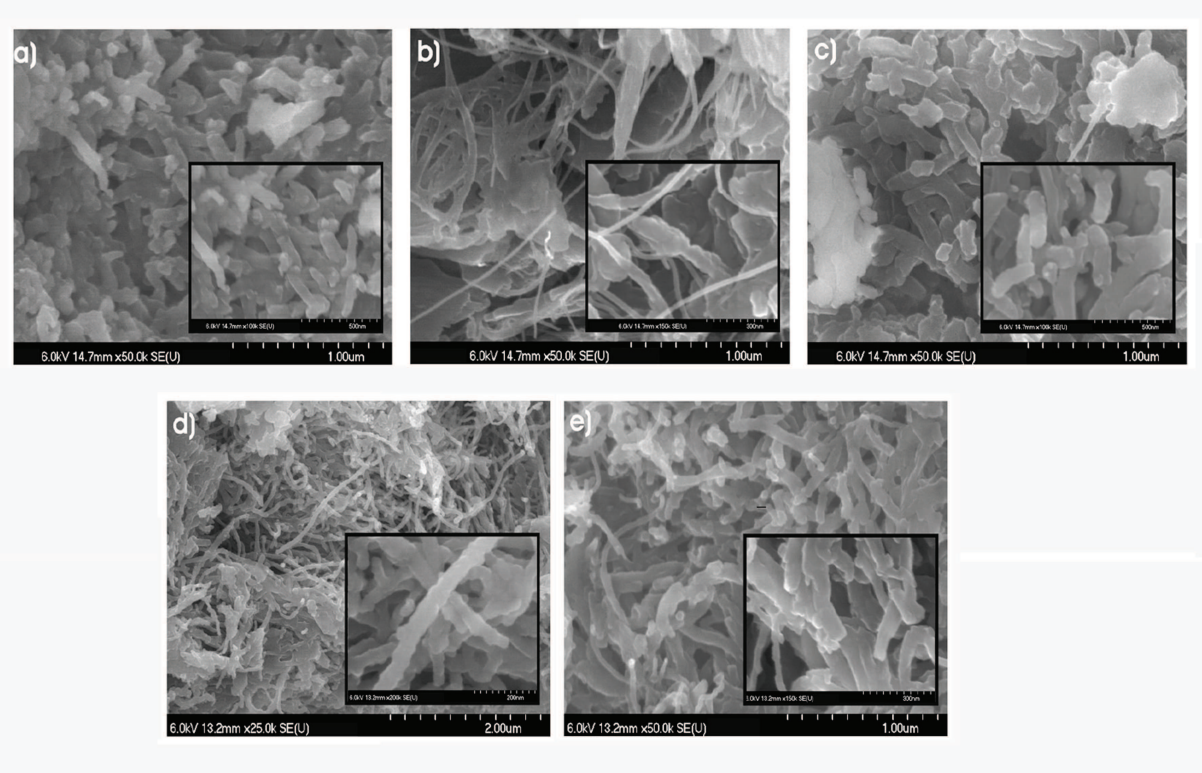

Figure 4.4: SEM images of CH3SO3H doped-PANI/CNT nanohybrids: (a) PANI, (b) PANI/UnOxSWNT, (c) PANI/OxSWNT, (d) PANI/UnOxMWNT, and (e) PANI/OxMWNT.

4.2.2.3 Experimental Details

Conducting experiments based on PTE technique are more or less similar to the phototpyroelectric (PPE) experiments [42, 130]. For PTE, the sensor is a thermoelectric (TE) device rather than a pyroelectric generator as in PPE. For making sensors all the PANI-CNT pellets were coated on both sides with gold or silver using a sputter coater (Cressington 108) or silver painted and attached electrical contacts on both sides. The electrically conducting coatings integrate all the generated charges on both surfaces of the sensor. A lock-in amplifier in voltage mode, connected directly to the PTE sensor, was used to detect the signal. We have used pure PANI samples and also composites with carbon nanotubes (CNT) as sensors. Typical electrical resistance between the terminals of the sensor measured was only a few ohms. The laser power used was also comparatively high ($\sim$ 750 mW) in order to get enough signal. Typically the signal was around 10 μV at a modulation frequency of 2 Hz and the noise level was as low as 50 nV. The laser power was chosen so that the signal to noise ratio stays better than 10 in the highest modulation frequency used for the experiment.

4.2.2.4 Results and Discussion

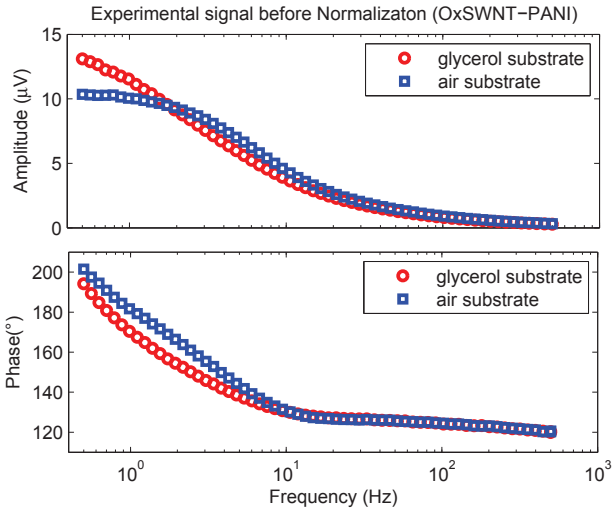

Figure 4.5: Experimental Signals obtained from PANI-OxSWNT using air and glycerol as backings. Amplitude (upper plot) and Phase (lower plot).

Experiments have been carried out using the setup described in Fig. 4.1. A typical Amplitude and phase data of a photothermoelectric (PTE) experimental signal for a 348.5μm thick doped PANI-OxSWNT are presented in fig.4.5 using either air or glycerol as substrates. Though the measured voltages for the signal amplitudes were weak ($\leq$ 10 μV), it can still be exploited with a satisfactory signal to noise ratio. Amplitude ratios and phase differences for the OxSWNT-PANI signals in fig. 4.5 are calculated and depicted as in fig.4.6. Thermal parameters are retrieved by fitting the signal against eq.(4.7) while considering $h_1 = 0$; the thermal diffusivity of $\alpha_1 = (4.68 \pm 0.04)\times10^{-7}$ m^{2}s^{-1} and a thermal effusivity of $e_1 = (1212 \pm 25)$ Ws$^{1/2}$m^{-2}K^{-1} are obtained. Then the thermal conductivity was calculated using the relationship $k_1 = e_1\sqrt{\alpha_1}$ and the result is $k_1 = (0.83 \pm 0.02)$ Wm^{-1}K^{-1}.

These results for OxSWNT-PANI sample were also calculated analytically using the zero crossing frequency ($f_0 = 11.5$ Hz) of the normalized phase using eq. (4.8). It led to a thermal diffusivity value of $(4.45 \pm 0.10)\times10^{-7}$ m^{2}s^{-1}. Based on this value, thermal effusivity has also been calculated from eq. (4.10) and obtained, $e = 1212 \pm 37$ Ws$^{1/2}$m^{-2}K^{-1} and the corresponding thermal conductivity value is 0.81 ± 0.04 Wm^{-1}K^{-1}.

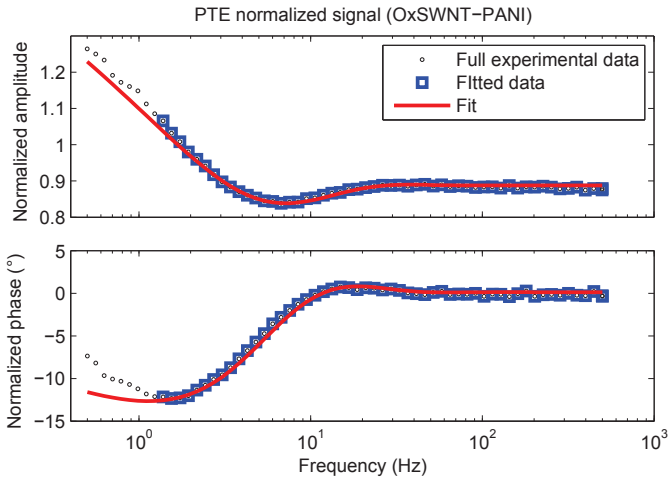

Figure 4.6: Normalized amplitude (upper plot) and phase (lower plot) from PTE experiment on OxSWNT-PANI

Table 4.1: Thermal parameters retrieved using PTE techniques for the PANI-OxSWNT composite; α: thermal diffusivity; e: thermal effusivity, k: thermal conductivity.

Parameter	PTE (fit)	PTE (analytic)
Diffusivity ($\times$ 10^{-7} m^2/s)	4.68± 0.04	4.45± 0.10
Effusivity ($J/Km^2s^{1/2}$)	1212 ± 25	1212 ± 37
Conductivity (W/mK)	0.83 ± 0.02	0.81 ± 0.04

4.3 Photothermal Radiometry Experiments as a Validation for PTE Results

Conducting measurements on solid samples using PTR are well established and extensively using for the accurate determination of thermal parameters [82, 131, 132]. The method for simultaneous determination of thermal diffusivity and effusivity of free standing thin layers is of interest [133]. Theoretical model for our experiments considers a three layer configuration with air as the top layer (*layer-0*), the sample as *layer-1* and air or liquid with well known thermal parameters as the backing (*layer-2*), depicted as in fig. 2.2. The sample is considered as optically opaque and the backing is thermally semi infinite. Using the surface absorption model described by eq. (2.41), at $z = 0$, can be used to find the temperature field at the sample surface and it reveals the thermal parameters of the sample. The reference signal for the normalisation can be obtained by performing the experiment with another backing material (e.g., air replaced with water) without altering the sample and *layer-1*. This means $\Re_2$, in eq. (2.41), is the only modifying parameter. Thus the equation for the normalised signal obtained by dividing two frequency scans with two different backing materials can be written as:

$$\Gamma_F(\omega, z=0) = \frac{I_0}{2\sigma_1 k_1(1+b_{01})}\left(\frac{1+\Re_2 e^{-2\sigma_1 d}}{1-\Re_0\Re_2 e^{-2\sigma_1 d}}\right) \times \frac{2\sigma_1 k_1(1+b_{01})}{I_0}\left(\frac{1-\Re_0\Re_{2r} e^{-2\sigma_1 d}}{1+\Re_{2r} e^{-2\sigma_1 d}}\right) \tag{4.11}$$

where, $\Re_2$ is replaced by $\Re_{2r}$ in the reference (normalization) signal.

Approximation while using 'air' interfaces:- Because of the extremely low effusivity of air medium makes the effusivity ratios b_{01} and b_{21} at both the sample interfaces will become negligibly small. The approximated terms are:

$$b_{01} \approx 0, \qquad b_{21} \approx 0, \qquad \Re_0 \approx 1, \qquad \Re_2 \approx 1$$

So the eq. (4.11) can be rearranged and rewritten as:

$$\Gamma_F(\omega, z=0) = \left(\frac{1+e^{-2\sigma_1 d}}{1-e^{-2\sigma_1 d}}\right)\left(\frac{1-\Re_{2r} e^{-2\sigma_1 d}}{1+\Re_{2r} e^{-2\sigma_1 d}}\right) \tag{4.12}$$

Multiplying the terms in the above eq. (4.12) and neglecting the higher order exponential term $\left(e^{-4\sigma_1 d}\right)$, which has again negligible contribution, will result in:

$$\boxed{\Gamma_F(\omega, z=0) = \frac{1+(\Re_{2r}-1)e^{-2\sigma_1 d}}{1-(\Re_{2r}-1)e^{-2\sigma_1 d}}} \tag{4.13}$$

Equation (4.13) represents the normalised temperature field on the top of a solid sample obtained by replacing the backing air with a known liquid. These approximations are well accepted and validated [134, 133].

4.3.0.5 Thermal Properties of PANI-CNT nanohybrids using PTR technique

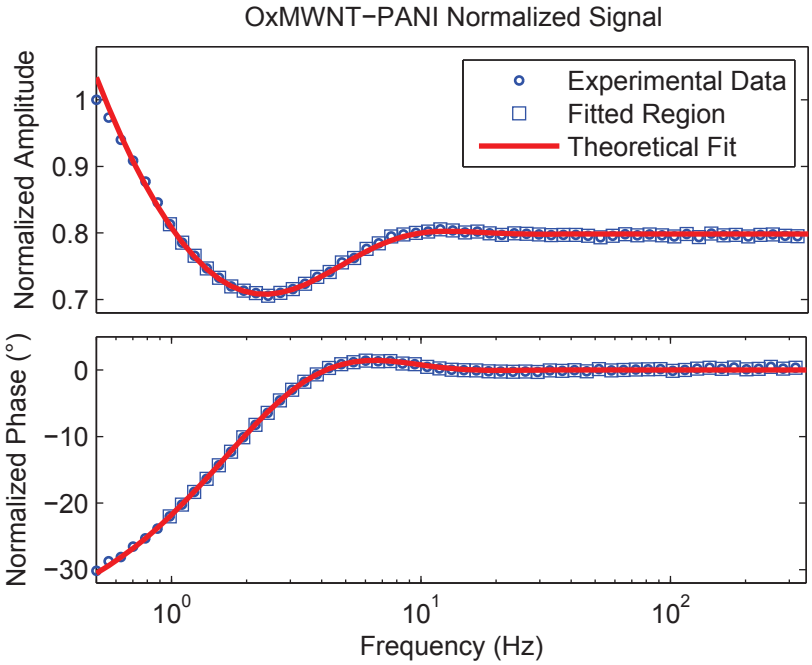

Figure 4.7: Normalized amplitude (upper plot) and phase(lower plot) and theoretical fit plotted vs. modulation frequency. The experiment has done on OxMWNT-PANI as sample having thickness 233μm and the normalization has done by replacing air with glycerol as substrate.

Using eq. (4.13), one can find the thermal diffusivity and effusivity of the sample layer while knowing the thermal parameters of the substrate. Thermal parameters for all the samples have been calculated by fitting amplitude and phase data separately and together simultaneously (complex fit). All the individual fit results are found consistent with each other and it validates the reliability of the experiment. The error bars are calculated by taken into account of the sample thickness errors and the statistical experimental errors. A typical normalized signal and theoretical fit from the experiment on OxMWNT-PANI sample is shown in fig. 4.7. Thermal diffusivity, effusivity and conductivity of PANI, OxMWNT-PANI, UnOxMWNT-PANI, OxSWNT-PANI, UnOxSWNT-PANI samples are shown in fig. 4.8. The results are also displayed in table 4.2.

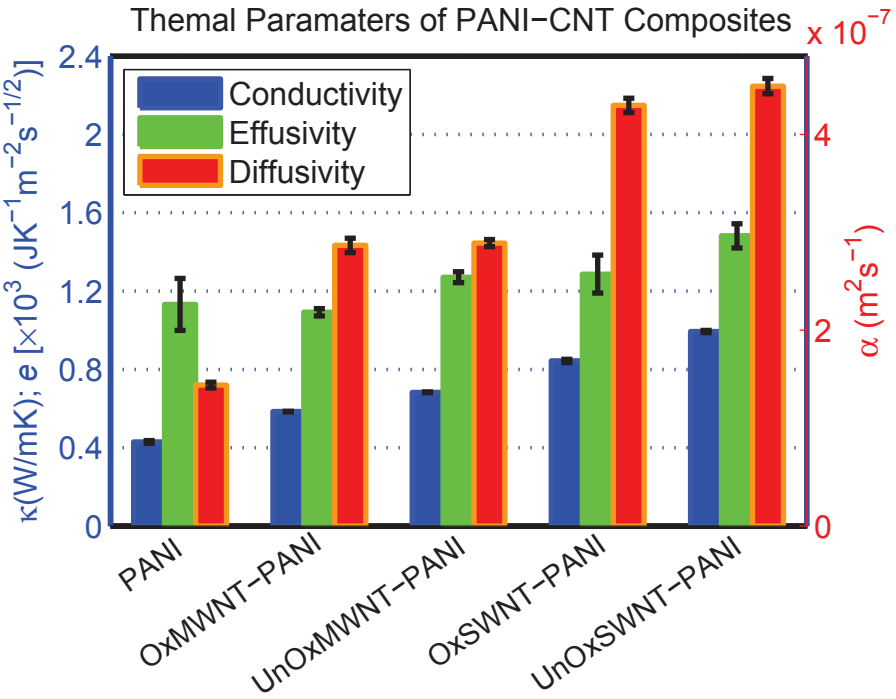

Figure 4.8: Thermal parameters with error bar of different PANI-CNT composites measured using PTR technique. The results are also displayed in table 4.2.

Table 4.2: Thermal diffusivity, effusivity and conductivity results of PANI-CNT samples (PTR results).

PANI-composite	Thermal diffusivity $\times 10^{-7}$ α (m^2s^{-1})	Thermal effusivity e ($JK^{-1}m^{-2}s^{-1/2}$)	Thermal conductivity κ ($Wm^{-1}K^{-1}$)
PANI	1.44±0.06	1132±133	0.43 ±0.01
-OxMWNT	2.87±0.01	1084±10	0.581±0.002
-UnOxMWNT	2.89±0.02	1293±21	0.695±0.001
-OxSWNT	4.3±0.1	1292±72	0.850±0.007
-UnOxSWNT	4.38±0.07	1523±53	1.01 ±0.004

4.4 Results and Discussions on Thermoelectric Properties of PANI-CNT nanohybrids

All the PANI-CNT samples were experimentally investigated using PTE technique and validated the results by conducting PTR experiments. A complete set of results on thermal diffusivities, effusivities and conductivities of all PANI composites measured using both PTE and PTR techniques are presented in table 4.3. Figure 4.9 is the graphical representation of the results using PTE technique alone. The results are clearly showing that the SWNT based composites exhibit higher thermal diffusivities and thermal conductivities than their MWNT counterparts. Evidently, UnOxSWNT-PANI showing the highest thermal conductivity with an increase of around 2.5 times than pure PANI. The lower conductivity values of MWNT composites than the SWNT composites are attributed to the usual higher thermal conduction property of SWNTs. Among all the four composites, oxidized nanotube composites are showing a little lower thermal conductivity values than their un-oxidized counter parts. This might be due to the presence of oxide layer along the surface of the nanotubes, which, upto a small extend, hindering the heat transport at the matrix-nanotube boundaries. Electrical conductivity studies on this same set of samples [22] are also confirming the same trend as from our thermal studies. Of interest, it is also pointing out that, regardless of the nature of the inclusions, the thermal effusivities stay roughly constant, which indicate the thermal conductivity behaviour is mainly controlled by the thermal diffusivity. Here, the higher thermal conductivities of individual SWNTs in comparison with individual MWNTs attributed to the higher thermal conductivity values of SWNT-PANI composites. Although it is acknowledged that SWNTs present a higher interfacial thermal resistance than the MWNTs [135], this property, however, is not sufficient to mitigate the effects of thermal conductivity differences between the aforementioned tubes. We believe, this is due to the strong polymer-nanotube interaction that came from the in situ polymerization procedure. Further, the thermal conductivities of oxidized nanotubes based composites are lower than their unoxidised counterparts. This behaviour can be explained by the oxidation process of CNTs which induces defects on the nanotubes. These defects scatter the phonons, and, thus, lower the thermal conductivity. A similar behaviour has been suggested for the lowering of the electrical conductivity in the case of oxidized CNT due to induced carrier scattering centres.

Table 4.3: Thermal diffusivity, effusivity and thermal conductivity Results of PANI-CNT samples.

PANI-	Thermal diffusivity $\times 10^{-7}$ α (m^2/s)		Thermal effusivity e ($J/Km^2s^{1/2}$)		Thermal conductivity κ (W/mK)	
	PTR	PTE	PTR	PTE	PTR	PTE
PANI	1.44±0.06	1.2±0.05	1132±133	1129±103	0.43 ±0.01	0.39±0.01
-OxMWNT	2.87±0.01	2.94±0.02	1084±10	1070±25	0.581±0.002	0.58±0.01
-UnOxMWNT	2.89±0.02	2.8±0.2	1293±21	1402±191	0.695±0.001	0.74±0.03
-OxSWNT	4.3±0.1	4.68±0.04	1292±72	1212±25	0.850±0.007	0.83±0.02
-UnOxSWNT	4.38±0.07	4.87±0.08	1523±53	1316±40	1.01 ±0.004	0.92±0.01

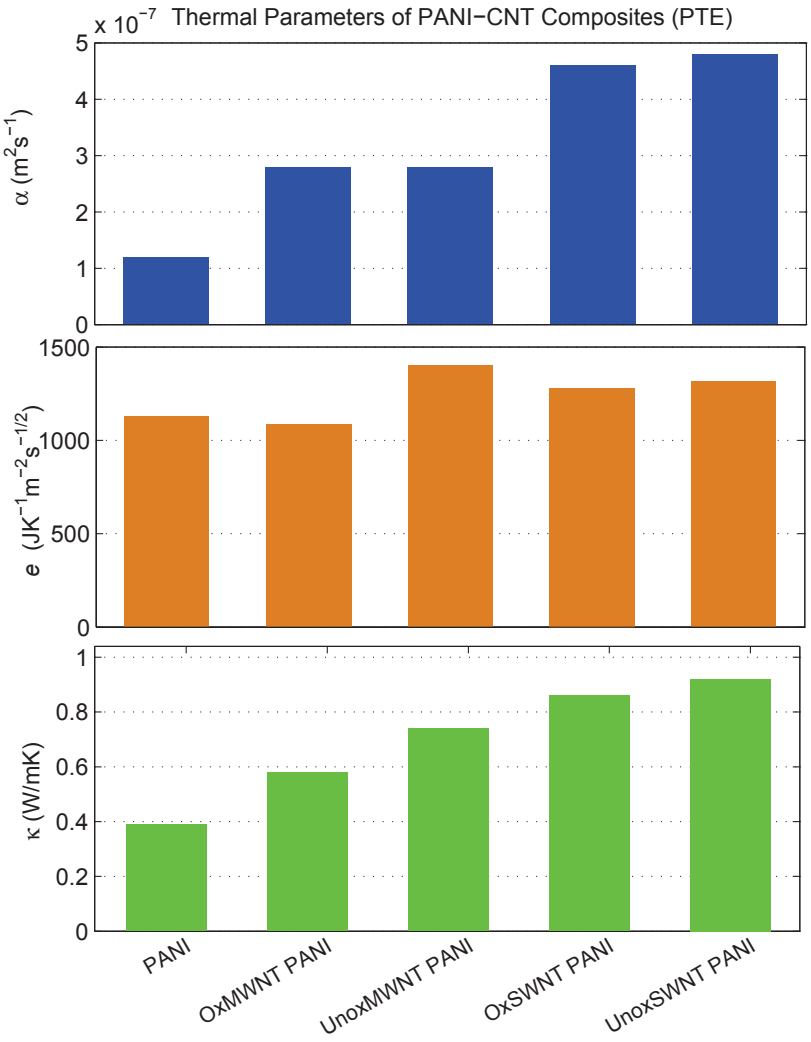

Figure 4.9: Experimental results of thermal parameters for PANI-CNT composites (PTE results)

Table 4.4 shows the Seebeck coefficient, electrical conductivity and thermal conductivities values obtained for various composites. Figure of merit (ZT) for each material samples have been calculated from these parameters using the formula $ZT = \frac{S^2\kappa_e}{k}T$, at ambient temperature ($T = 300$K). The results are displayed in figure 4.10. It is obvious from the figure that the ZT is considerably enhanced with the incorporation of carbon nanotubes into the polymer material even with a small fraction of CNT (6.6 wt-%). Overall, nanocomposites containing unoxidized and single-walled CNTs exhibit better thermophysical properties than their oxidized or multiple-walled counterparts.

Table 4.4: Seebeck coefficient, electrical conductivity and thermal conductivity Results.

Material	Seebeck Coefficient S (μV/K)	Electrical Conductivity κ_e (S/m)	Thermal Conductivity κ (W/mK)
PANI	5.8	0.82	0.39±0.01
PANI-OxMWNT	13.5	14	0.58±0.01
PANI-UnOxMWNT	10.6	70.1	0.74 ±0.03
PANI-OxSWNT	12	132.23	0.83±0.02
PANI-UnOxSWNT	33	530.98	0.92±0.004

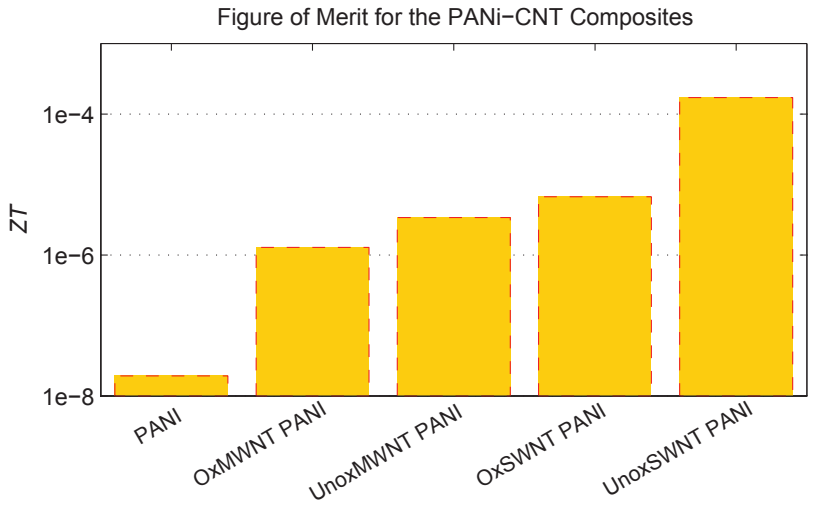

Figure 4.10: Figure of Merit for the PANI-CNT composites

Clearly, a careful choice of CNTs and their blending with traditional intrinsically conducting polymers have led to an enhancement of the hybrid Seebeck coefficient and electri-

cal conductivity without increasing significantly their thermal conductivity due to interfacial thermal resistances between the nanotubes and the polymeric matrix. These improvements contribute nearly four orders of magnitude increase in ZT value in the unoxidized, single-walled hybrid sample. However, its ZT value of 2×10^{-4} remains low and is far from reaching the recommended 2 - 3 ZT range required for a technological breakthrough. Nevertheless, the present work has its advantages because of the preparation methods and sample processing are inexpensive and straightforward. There are also possibilities for further improvements in hybrid physical characteristics by a judicial choice/amount of each constituent of the hybrid and their synthesize.

4.4.0.6 Summary of the results on PANI-CNT samples

We have reported a new photothermal experiment for the determination of thermal properties based on PhotoThermoElectric (PTE) effect. It has been demonstrated that parameters such as thermal diffusivity, effusivity and conductivity of a nano-structured thermoelectric material can be determined analytically and numerically using PTE technique. The main advantage of this approach permits the assessment of the thermal properties of a TE material without the need of an external sensor. The formalism of the PTE signal has been developed and numerical as well as analytical procedures for extracting thermal parameters are also proposed. The thermal parameters retrieved from the PTE signals for PANI-CNT samples have been compared with those obtained from the conventional Photothermal Radiometry experiment. A good agreement has been found between the two different experimental techniques demonstrating the relevance and the usefulness of the developed methodology. It is also noteworthy that the values obtained for the thermal conductivity from the analytical procedure were similar to the results obtained from the fitting procedure with an agreement better than 97 %. Therefore, the proposed methodology provides an accurate and simple way to determine the thermal conductivity of TE materials without any intermediate media which makes this technique full of prospects. Using this novel technique, various doped PANI/(oxidized or unoxidized, single or multiple-walled) CNT composites have been investigated and thermal parameters were deduced. Knowing the Seebeck coefficient and electrical conductivity values, ZT have been calculated. Among the investigated samples, PANI/unoxidized SWNT nano-composite showed the most promising TE characteristics. This result can be explained by i) the electrical con-

ductivity improvement provided by the high SWNT electrical conductivity ,and, ii) the weak thermal conductivity increase resulting from interfacial thermal resistances between nanotubes and PANI. The CNT oxidization process creates defects on the nanotubes leading to a decrease of the thermal conductivity.

4.5 PTE Technique for Thermal Investigation of Solids samples

TE materials can also be used as temperature sensors for the characterization of materials thermally. Similar to the PPE methods, the detection configurations can be classified as: (i) the "front" one (sensor directly irradiated and sample in back position) coupled with TWRC method (scan of the liquid's thickness), for thermal effusivity measurements [136, 137, 79] and (ii) the "back" one (sample directly irradiated and sensor in back position), together with the chopping frequency scan, for thermal diffusivity investigations [138]. Further we are deriving the equations for these two configurations, so called Front-PTE (FPTE) and Back-PTE (BPTE).

4.5.1 Front Photothermoelectric Configuration (FPTE)

Theoretical model for the FPTE configuration is depicted as in figure 4.11. Here the model has to accommodate one more layer than we have derived in the previous chapter. Since the basic procedure for any number of layers are same, we are expanding the already derived three layer model with extra terms in order to obtain a theoretical model for a four layer configuration. A proposed solution for the temperature field T_3 for an additional fourth layer can be written as:

$$T_3 = \left(A_3 e^{\sigma_3 z} + B_3 e^{-\sigma_3 z}\right) e^{i\omega t} \qquad [z \leq -(d+b)] \tag{4.14}$$

where, d and b are the thickness of *layer: 2* and *layer: 3*. A_3 and B_3 are the unknown constants. The boundary conditions for solving the equation are:

$$\kappa_2 \frac{\partial T_2}{\partial t} = \kappa_3 \frac{\partial T_3}{\partial t}, \qquad T_2 = T_3, \qquad [z = -(d+b)] \tag{4.15}$$

After solving the equations for temperatures for all layers including this fourth layer, one can arrive at an expression for voltage induced on the TE sensor given by:

$$\Delta V = S\int_{T(z=-d)}^{T(z=0)} dT = S[T(z=0) - T(z=-d)] \tag{4.16}$$

$$\Delta V = S\frac{I_0}{2\kappa_1\sigma_1}\frac{(1+Q)(e^{\sigma_1 d}-1)+(1-Q)(e^{-\sigma_1 d}-1)}{(1-Q)e^{-\sigma_1 d}-(1+Q)e^{\sigma_1 d}} \tag{4.17}$$

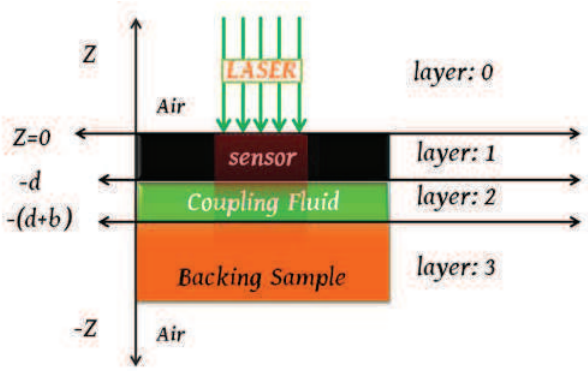

Figure 4.11: Front Configuration

where,

$$Q = b_{21}\frac{(1+b_{32})e^{\sigma_2 b}-(1-b_{32})e^{-\sigma_2 b}}{(1+b_{32})e^{\sigma_2 b}+(1-b_{32})e^{-\sigma_2 b}} \tag{4.18}$$

and $b_{21} = e_2/e_1$, $b_{32} = e_3/e_2$.

If we suppose that the thermoelectric element (*layer: 1*) is thermally thin, then $e^{\pm\sigma_1 d} = 1 \pm \sigma_1 d$ and eq. (4.17) reduces to:

$$\Delta V = -S\frac{I_0}{2\kappa_1\sigma_1}\frac{Q\sigma_1 d}{Q+\sigma_1 d} \tag{4.19}$$

Equation (4.19) indicates that the electrical signal obtained from a TE inserted in a sandwiched cell as presented in figure 4.11, and periodically illuminated with an optical radiation, is a complex voltage and depends on the thermal diffusivity and effusivity of TE element and coupling fluid and on the thermal effusivity of the material situated in the backing position. In principle, experimentally, we can perform a scanning procedure, using as scanning parameter: the chopping frequency of radiation or the thickness of the coupling fluid. In the FPPE experiments, it has been shown that the thickness scanning procedure (so-called thermal wave resonator cavity method TWRC [8]) leads to more accurate results and (when possible) it is preferred to frequency scanning procedure. Consequently, if we perform a scan of the phase or amplitude of the signal as a function of coupling fluid's thickness (at constant modulation frequency), we can obtain the thermal effusivity of the backing material.

It is useful to eliminate from equation (4.19) some quantities characterising the set-up, and this can be done, by performing a normalization with infinite thickness of coupling fluid ($b-$variable thickness). In such a case, Q reduces to b_{21} and the normalization signal is given by:

$$\Delta V_0 = -\frac{SI_0}{2\kappa_1\sigma_1}\frac{b_{21}\sigma_1 d}{(\sigma_1 d + b_{21})} \tag{4.20}$$

The normalized voltage becomes,

$$\Delta V_n = \frac{\Delta V}{\Delta V_0} = \frac{[\sigma_1 d + b_{21}]\left[(1+b_{32})\,e^{\sigma_2 b} - (1-b_{32})\,e^{-\sigma_2 b}\right]}{(1+b_{32})\,e^{\sigma_2 b}\,(\sigma_1 d + b_{21}) + (1-b_{32})\,e^{-\sigma_2 b}\,(\sigma_1 d - b_{21})} \tag{4.21}$$

4.5.2 Back Photothermoelectric Configuration (BPTE)

The 2-layers detection cell in back configuration is shown schematically in figure 4.12.

In this configuration, the opaque front surface of the sample is irradiated, and the heat is generated at the gas-sample interface. Thermal diffusion equations together with boundary conditions are the same. So the equation for the voltage generation in the TE sensor can be written as, according to figure 4.12,

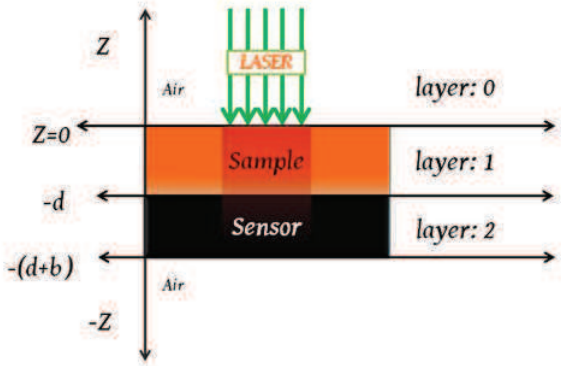

Figure 4.12: Front Configuration. Opaque sample and thermoelectric sensor

$$\begin{aligned}\Delta V &= S\int_{T(z=-d-b)}^{T(z=-d)} dT \\ &= S[T(z=-d) - T(z=-d-b)]\end{aligned} \tag{4.22}$$

If we impose from the beginning the condition of thermally thick sensor we can approximate $e^{-\sigma_2 b} \approx 0$, and applying the boundary conditions, we get the following expression for the PTE signal:

$$\Delta V = \frac{SI_0}{\kappa_2\sigma_2\left[(b_{12}-1)e^{-\sigma_1 d} - (b_{12}+1)\,e^{\sigma_1 d}\right]} \tag{4.23}$$

The easiest way to normalize the signal described by eq. 4.23 is to perform a measurement with empty sensor. If $d = 0$, the normalization signal becomes:

$$\Delta V_0 = -\frac{SI_0}{2\kappa_2\sigma_2} \tag{4.24}$$

and the normalized one:

$$\Delta V_n = \frac{2\exp(-\sigma_1 d)}{(b_{12}+1)-(b_{12}-1)\exp(-2\sigma_1 d)} \tag{4.25}$$

If, additionally, the sample is at quasi thermally thick frequency regime then $e^{-2\sigma_1 d} \approx 0$ and eq. (4.25) reduces to:

$$\Delta V_n = \frac{2e^{-\sigma_1 d}}{(b_{12}+1)} \tag{4.26}$$

Equation 4.26 indicates that a similar scan of the phase of the BPTE signal as a function of the chopping frequency (at constant thickness), or thickness of the layer 1 (for liquid samples, at constant frequency) can lead to the direct measurement of sample's thermal diffusivity. The amplitude can also be used for thermal effusivity measurement.

4.5.3 Comparison with PPE

When using the photopyroelctric (PPE) technique, in the same FPPE configuration and approximation (thermally thin sensor and coupling fluid), the normalized FPPE voltage is given by [139]:

$$V_n^{FPPE} = \frac{\sigma_1 d + b_{21}}{(\sigma_1 d) + b_{21}\left[\frac{1+\Re_{32}e^{-2\sigma_2 b}}{1-\Re_{32}e^{-2\sigma_2 b}}\right]} \tag{4.27}$$

with $\Re_{32} = (b_{32}-1)/(b_{32}+1)$ which is practically identical with eq. (4.21). When working with PPE, in the back (BPPE) configuration, in the thermally thick regime for the pyroelectric sensor we obtain:

$$V_n^{BPPE} = \frac{2}{(b_{12}+1)}e^{-\sigma_1 d} \tag{4.28}$$

which is different from eq. (4.25), but in the thermally thick limit for the sample, the two detection configurations lead to the same result.

4.5.4 Mathematical simulations

As pointed out before [140], when it is possible, we use as source of information only the phase of the signal because, being only a time delay, the phase is less noisy than

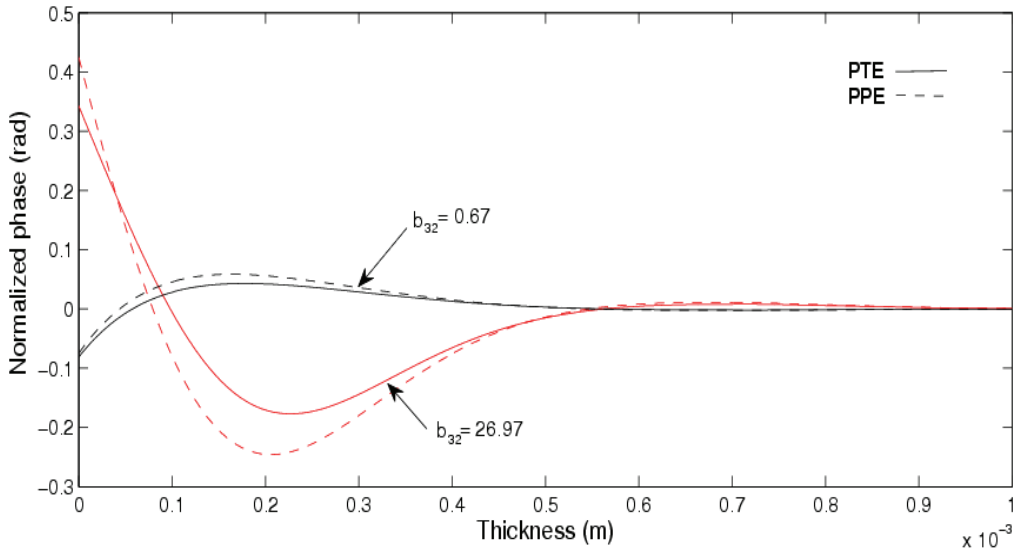

Figure 4.13: Normalized phase of the PTE and PPE signals, in front configuration, for two e_3/e_2 ratios. $b_{32} = 0.67$ - backing bad thermal conductor; $b_{32} = 26.97$ - backing good thermal conductor.

the amplitude (it is not influenced by the fluctuations of the laser beam intensity or the roughness of the illuminated surface). Some mathematical simulations of the normalized phase of the PTE and PPE signals in front configuration (Eqs. (4.21) and (4.25)), for different e_3/e_2 ratios, are presented in fig. 4.13

Figure 4.13 indicates that the shape of the curves are rather similar, the only differences are generated by the different values of the PPE and PTE sensors' thermal parameters. fig. 4.14 presents mathematical simulations (eq. (4.25)) of the normalized phase of the PTE signal as a function of $\sqrt{f}$ for three samples: aluminum, brass and $LiTaO_3$. In the thermally thick limit for the sample, the plot phase against $\sqrt{f}$ is linear as predicted by eq.(4.26).

4.5.5 Experiments on Solid Samples Using PTE technique

In the FPTE configuration, the sensor is glued on a rotating stage. The backing material is situated on a micrometric stage. The modulated radiation (800 mW YAG laser, f=0.3Hz) is partially absorbed by the (blackened) front electrode of the sensor. The space between the sensor and the backing material accommodates the liquid layer. The liquid's thickness variation is performed with a step of 0.03μm (9062M-XYZ-PPP Gothic-Arch-Bearing Pi-

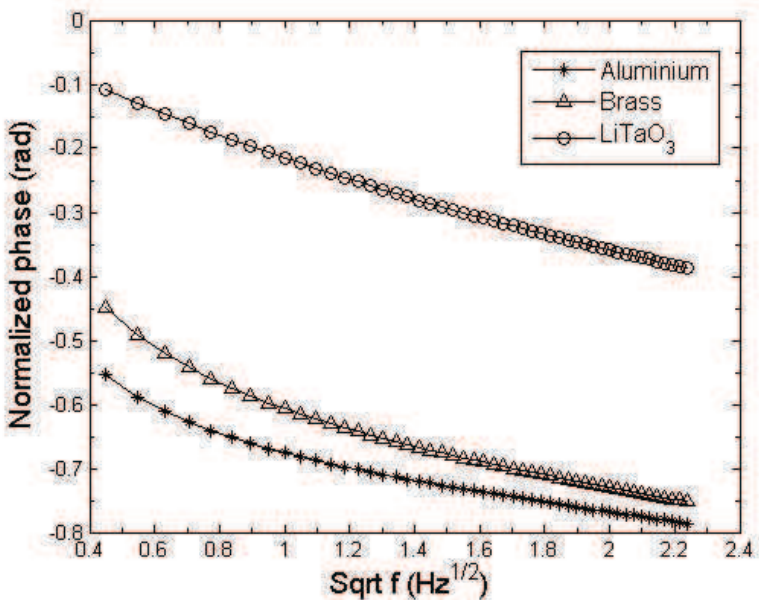

Figure 4.14: Normalized phase of the BPTE signal as a function of $\sqrt{f}$ for Al, brass and $LiTaO_3$. Layers' thickness: 1mm Al and brass; 0.5mm $LiTaO_3$.

comotor) and the data acquisition was taken each 30^{th} step. The "rough" control of the liquid's thickness and the parallelism between backing and sensor are assured by 3 and 6 -axis micrometric stages. During the scanning procedure, the sample's thickness variation is very rigorously controlled, but the absolute sample's thickness is not precisely known. Its correct value is obtained as a result of a fitting procedure [70]. The coupling fluid was ethylene glycol ($e_2 = 890 \mathrm{Ws}^{-1/2}\mathrm{m}^{-2}\mathrm{K}^{-1}$; $\alpha_2 = 9.36\mathrm{e}^{-8}\mathrm{m}^2\mathrm{s}^{-1}$) with thickness ranging from 0 to 1mm. The normalized signal is obtained with thermally thick (thickness larger than 700μm) coupling fluid. All the measurements were performed at room temperature. The PTE signal was processed with an SR 830 lock-in amplifier. Even if the signal generated by TE was rather small (10μV-50μV), the signal to noise ratio was good (S/N>100). Several backing solids with different values of thermal effusivity (Al, glass, teflon, polypropylene, processed as disks with 10 mm diameter and thicknesses of about 1 cm) were selected for investigations, thus covering a large range for the typical effusivity spectrum of solids. At 0.3 Hz chopping frequency, the request of the particular detection case (thermally thin regime for the sensor and thermally thick for the backing) was respected. The coupling fluid changes the thermal regime from thermally thick to thin at about 600μm. As demonstrated in the theoretical section, the information was collected in the thermally thin regime

for the coupling fluid.

In the back detection configuration (BPTE), the sample (disks of $d = 10$mm and $d \leq 1$mm) has glued on the surface of the sensor with a thin layer of silicon grease. The irradiated surface of the sample was blackened to assure good optical absorption. In this configuration, PTE has the same problem as PPE: due to the attenuation of the thermal wave in the sample, generally, good thermal conductors (as Al and brass in our work) can be selected as samples. The thermal isolators (at about 1mm thickness) attenuate too much the thermal wave, and the signal to noise ratio is too small to be useful. If trying to polish bad thermal conductors at thickness of 100-200μm, they become transparent, and one request of the particular detection case (opaque sample) is not fulfilled. The scanning parameter was in this case the chopping frequency of radiation; the typical scanning range was 0.3-3 Hz. At such low frequencies, 1mm thick good thermal conductors as Al and brass are normally thermally thin but, due to the properties of the adjacent layers (air on one side), as demonstrated by Chirtoc *et al.*[141], the critical frequency (the crossing frequency from thermally thin to thick regime) is in fact much lower and they can be considered thermally thick.

In order to prove the suitability of the BPTE method, as a challenge, the thermal diffusivity of a largely used pyroelectric sensor (500μm thick LiTaO3 single crystal) was measured.

4.5.5.1 Experimental Results

The results obtained for the measurements performed in the FPTE configuration are displayed in figs.4.15, 4.16, 4.17 and 4.18 together with the best fits (eq.(4.21)). The room temperature values of the thermal effusivity for the investigated materials are in rather good agreement with literature data [142, 143, 144].

Typical behaviours of the phase of the PTE signal, in the BPTE configuration, for the brass/TE sensor system, and for the empty sensor (signal used for normalization) as a function of the laser modulation frequency are presented in fig. 4.19. Figure 4.20 displays the normalized phase as a function of sqrt (f) for this system (brass/TE sensor) together with the best fit performed in order to obtain the value of thermal diffusivity of brass.

Figure 4.21 presents the behaviour of the phase of the BPTE signals, as a function of sqrt(f), in the linear region, for two good thermal conductors (Al and brass) and a $LiTaO_3$

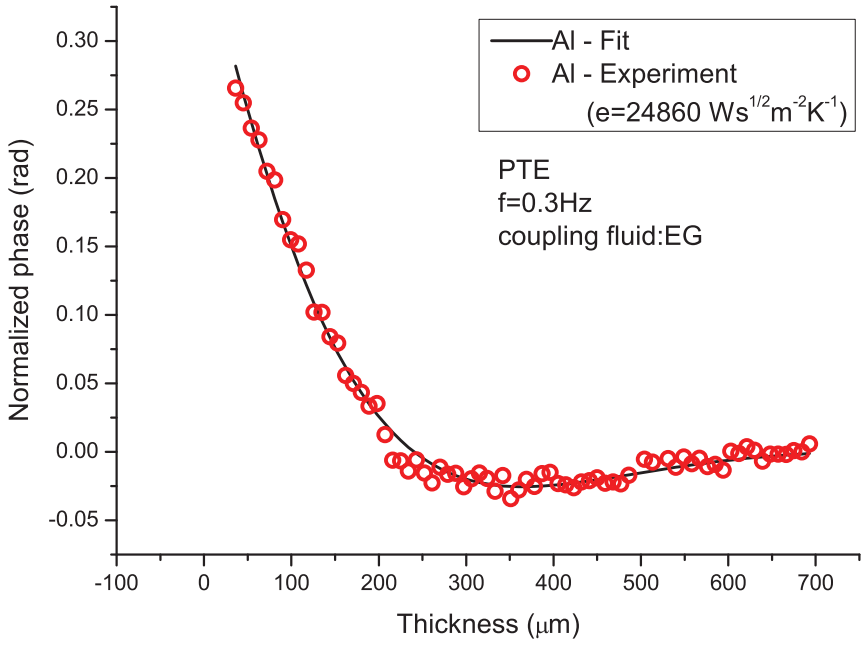

Figure 4.15: Normalized phase of the FPTE signal as a function of coupling fluid's thickness for aluminium sample

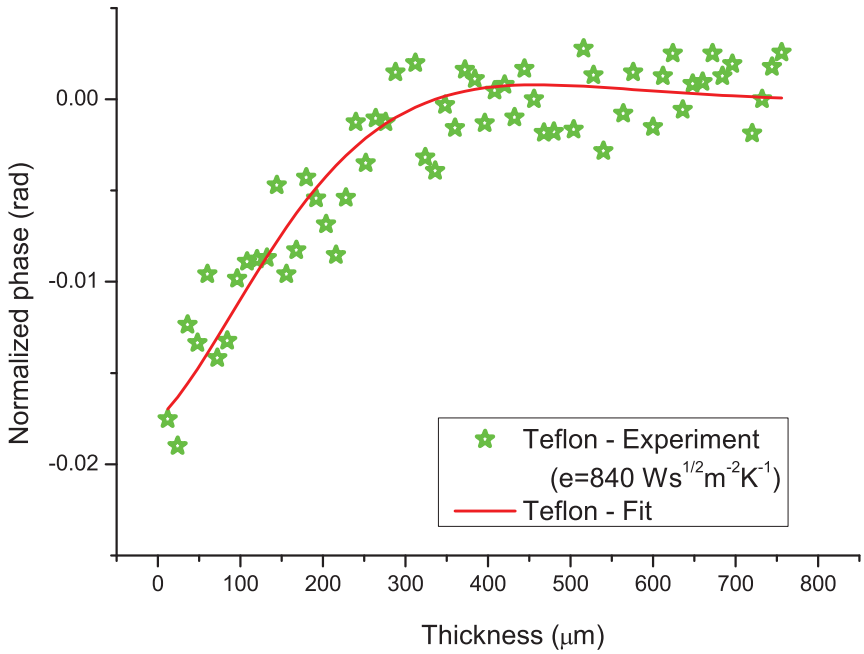

Figure 4.16: Normalized phase of the FPTE signal as a function of coupling fluid's thickness for teflon sample

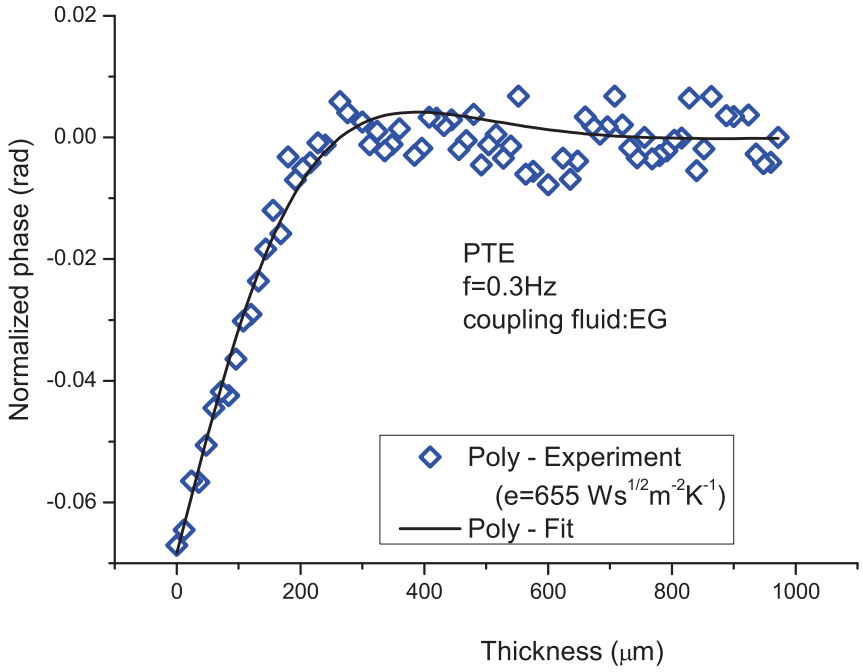

Figure 4.17: Normalized phase of the FPTE signal as a function of coupling fluid's thickness for polyethylene sample

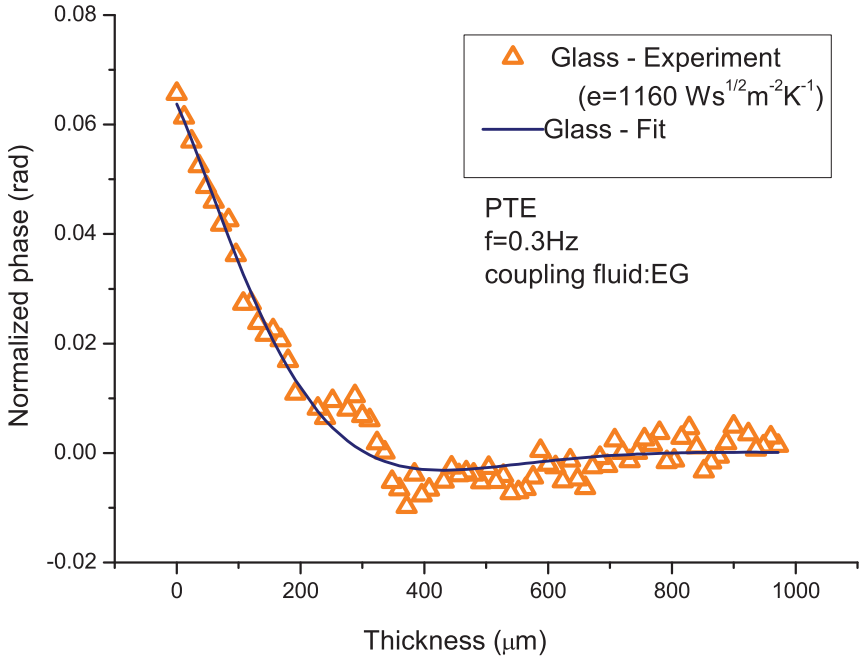

Figure 4.18: Normalized phase of the FPTE signal as a function of coupling fluid's thickness for glass sample

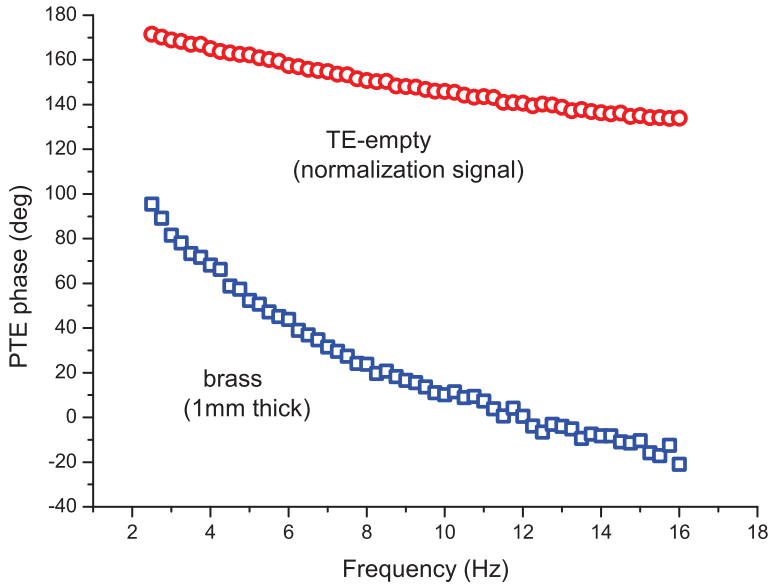

Figure 4.19: Experimental PTE phase signals as a function of frequency, in back configuration, for the brass/TE assembly (blue squares) and for the empty sensor (red circles).

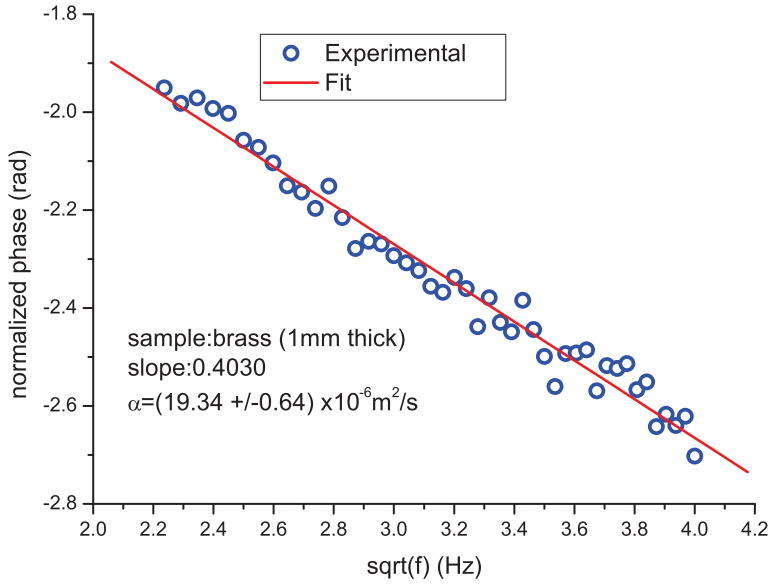

Figure 4.20: Normalized phase as a function of sqrt(f) for the BPTE signal from brass sample.

single crystal. Their room temperature values of the thermal diffusivities are displayed in table 4.5 together with the values measured using PPE and infrared thermography (IR-thermography) techniques on the same samples. These measured values are also in good agreement with the available literature data [143, 145].

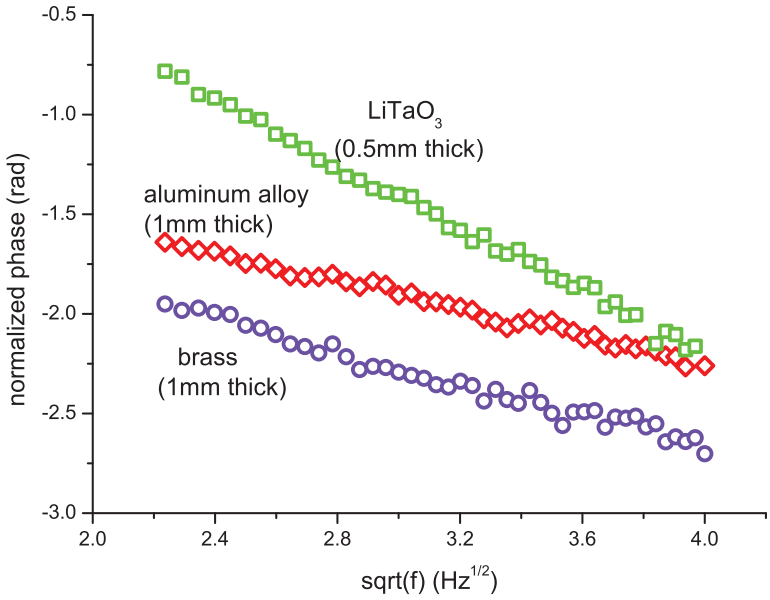

Figure 4.21: Normalized phases of the PTE signals, in back configuration, as a function of sqrt(f) for brass (violet circles), Al (red diamonds) and $LiTaO_3$ (green squares).

Table 4.5: Thermal diffusivities of aluminium, brass and $LiTaO_3$ measured using PTE, PPE and IR-thermography techniques.

Material	Thermal Diffusivity ($\times 10^{-6} m^2/s$)		
	PTE	PPE	IR-Thermography
Aluminium (alloy)	27.20±0.57	36.94±0.20	30±1
Brass	19.34±0.64	17.93±0.21	20±1
$LiTaO_3$	1.24±0.03	1.00±0.01	—

4.5.5.2 Summary of PTE Experimental Results on Solid Samples

The theory of the two detection configurations was developed and the results compared with PPE technique in section 4.5.3. In principle, the general results obtained for the PTE

voltage in both front and back configurations are different from PPE ones, but when using particular cases of experimental interest ((i) front configuration with opaque sensor, thermally thin sensor and coupling fluid, and semi-infinite backing, or (ii) back configuration with optically opaque sample and thermally thick sample and sensor) they are identical. Consequently, the only differences and possible advantages of this new technique come from the values of the sensors' (pyro and TE) thermal and/or electrical parameters. For example, in the case of the TE used in this work, both thermal effusivity and diffusivity of the TE are about 3 times smaller than the similar parameters of a $LiTaO_3$ pyroelectric sensor. Consequently, in order to fulfil the conditions for particular detection cases (thermally thin/thick regime for different layers of the detection cell), different ranges for the scanning parameters are required. This can be an advantage or disadvantage, depending on the type of investigated material. A huge difference between the TE and pyroelectric sensors is their electrical resistivity. From experimental point of view, the low electrical resistivity (few Ohms) of TE is correlated with low signal voltage (tens of μV), but also with very low noise signal (tens of nV). The typical S/N ratio is larger than 10^2 -10^3, similar with that obtained with pyroelectric sensors. To go on with the comparison of the two methods, the PTE needs higher levels of incident radiation (hundreds of mW), but the TE generators are not limited in temperature by a critical one, as in the case of pyroelectric sensors (Curie point).

Here, some applications on some solids, covering a large range for the typical values of thermal parameters (Aluminium, Glass, Teflon, Polyethylene and even a largely used pyroelectric material, $LiTaO_3$), were described, in order to demonstrate the suitability of the method. The results obtained for the values of the thermal parameters are in agreement with literature data. In conclusion, a new photothermal technique, the photothermoelectric method, was proposed for calorimetric investigations. The method is an alternative to the PPE; it is very similar with the PPE technique, but it is based on a new class of materials with different properties.

4.6 Summary

A novel technique, based on the photothermoelectric (PTE) effect has been introduced for thermal characterization of TE generators. For that, the voltage generated in TE sen-

sors due to the temperature variations between the two sides were modelled in terms of temperature fields and solved the heat diffusion equations. As obtained, equations for temperature fields contains the thermal transport properties of TE material. Thereby, we can thermally characterize the thermoelectrics without using a secondary sensing mechanism.

We have also proposed the very same technique as an alternative calorimetry technique for measuring dynamic thermal parameters of solid samples. In order to show the various technical possibilities, we have used both back and front detection configurations, coupled with laser chopping frequency as well as thickness scanning procedures. The front PTE configuration, together with the thermal-wave resonator cavity (TWRC) method as scanning procedure, has been used to measure the value of thermal effusivity. The back PTE configuration, together with the chopping frequency of incident radiation as scanning parameter, lead to the direct measurement of thermal diffusivity. The theory of the two detection configurations was developed. In principle, the general results obtained for the PTE voltage in both front and back configurations are different from PPE ones, but when using particular cases of experimental interest ((i) front configuration with opaque sensor, thermally thin sensor and coupling fluid, and semi-infinite backing, or (ii) back configuration with optically opaque sample and thermally thick sample and sensor) they are identical.

General Conclusions and Future Outlook

This thesis work is intended to investigate on the thermal transport properties of material composites using photothermal techniques. As a continuation of past research works in our laboratory, this work is aimed to study thermal properties of two different classes of technologically important materials. The first class deals with polymer dispersed liquid crystals and the second class is about thermoelectric (TE) polymer nano composites.

Polymer dispersed liquid crystal (PDLC) samples are chosen because of their rich physical properties, so that we can consider them as a model system to interpret many physical phenomena. One of its interesting nature is coming from the heterogeneity of the system by the presence of spherical inclusions of liquid crystals whose thermophysical properties can be controlled by external means without making any physical interruption to the sample system. The PDLC samples used in this studies are made of polystyrene (PS) and 4-Cyano-4'-pentylbiphenyl (5CB) liquid crystal. Samples having two different liquid crystal (LC) concentrations (73 wt% and 85 wt%) were prepared using a procedure based on solvent induced phase separation (SIPS).

We have chosen photothermal radiometry (PTR) technique to investigate the thermal properties of samples because of the experimental simplicity and non-contact nature. The latter property helps to conduct measurements on samples under external electric field with greater freedom in sample cell erection than contact photothermal (PT) methods. In order to perform the thermal investigations with high accuracy and resolution similar to the one obtained using contact PT techniques like photopyroelectric (PPE), we have developed novel methods with PTR, so called back-front-PTR (BF-PTR) and back-PTR (B-PTR), to study liquid samples. In this novel approach, a small amount (about 5 μl) of liquid sample is enclosed between two transparent windows (a quvette is used as bottom

window having known sample space thickness) in which the top window (made of CaF_2 and facing PTR detector) has been chosen so that it is transparent to infrared radiation specified by the detector. The sample cell is prepared to contain sample at the middle and thin opaque coatings are made at faces of each top and bottom windows on the sample touching surface to obtain laser heating exactly at the surface of the sample. In B-PTR, the heating of the sample is from the bottom window side for both the sample and reference scans. This method gives thermal diffusivity and effusivity of the sample. But the sample has to be replaced by a reference liquid for realizing the reference scan. Apart from this, in BF-PTR configuration, there is no sample replacement needed, while, frequency scans of the laser intensity modulations are performed from bottom side is normalized by a second frequency scan of the sample from top. Here, thermal diffusivity is the only parameter which can be deduced.
Both PTR methods are validated and compared with results from existing techniques and found they can be used for the thermal characterization of liquid samples with high accuracy and certainty. A possible disadvantage of these methods are coming from the higher laser power (a few tens of milliwatts) to be used for sample heating than compared to the PPE techniques. This may limit the temperature resolution in the case of high resolution phase transition studies are being performed.

We have studied thermal transport properties of PDLC samples under amplitude varying (at fixed frequency) and frequency varying (at fixed amplitude) electric field (EF). The measurements have been carried out using B-PTR configuration. Here, the EF varying results are obtained using experiments with single chopping frequency of the laser source, which is one of the advantages of this configuration if the sample properties are known at zero electric field.

The amplitude (of the EF) varying experiments are confirming our already published works and the frequency (of the EF) varying experiments clearly showing the Maxwell-Wagner-Sillars (MWS) effect (polarization field effect) on thermal properties of PDLC samples. Relations between thermal conductivity of PDLCs and existing MWS model are established and the results are numerically fitted to find electrical properties (electrical conductivities of PS and LC as well as the threshold electric field (E_0) for LC droplet alignment) of both PDLC samples (of 73% LC and 85% LC). Obtained results for E_0 has been used to calculate droplet elastic constants. Our results are showing that the amplitude

of the threshold electric field increases with reducing droplet size (or LC concentration) as expected.

An interesting outcome of PDLC results from frequency (of EF) varying experiments have shown, for the first time to the best of our knowledge, that the thermal transport through PDLCs can be controlled via changing the frequency of the applied EF. In other words, the thermal transport properties of PDLC films are also affected by depolarization field effects as in the case of optical transmission properties. Moreover, the experimental results give access to find various physical properties such as: elastic constants, threshold electric field, Kapitza resistance, average molecular long axis orientation of LC droplets.

The second part of this thesis work is concerned about thermal investigation of thermoelectric (TE) polymer nano-composites. Studies on TE materials are particularly interesting because of their growing importance in waste heat energy harvesting technology. As part of this work, we have developed novel photothermal technique based on photothermoelectric (PTE) effect to measure thermal properties of TE materials directly. The PTE technique is established theoretically and validated experimentally by finding thermal properties of the same set of samples using classical photothermal radiometry technique. The samples used are composites made of polyaniline (PANI), a widely used conducting polymer, and carbon nanotubes (CNT). Four sample composites are prepared at 6.6 wt% of four kinds of CNTs (un-oxidized or oxidized / single or multi walled nanotubes). Comparing with other already reported studies on PANI-CNT materials, our samples are stay aside due to its novel preparation method and oxidation levels of CNTs. A chemical synthesis procedure in which the CNTs are wrapped around by PANI and form hybridized composites via an in situation polymerization procedure. Scanning electron microscope (SEM) images of these as grown PANI-CNT composites are used to confirm their physical structures. Results from thermal properties of these samples showed that single walled CNT composites are more thermally conductive than multi-walled CNT composites. Moreover, composites with oxidized nanotubes have lower conductivity than their unoxidised counter parts. The results have shown that the maximum enhancement in thermal conductivity is only about 2.5 times higher than the pure PANI sample while the measured electrical conductivity and seebeck coefficients are about 650 times and 6 times higher than pure PANI, respectively. This observation is particularly interesting and highly recommended because, the efficiency of TE materials are proportional to electrical conductivity and see-

beck coefficient while it is inversely proportional to sample's thermal conductivity. The experimental observations are analysed in the light of nanotube physical properties and interfacial thermal resistance.

We have also described PTE technique for measuring thermal properties of solid samples while using TE materials as thermal sensors. The developed techniques are classified under back-PTE (B-PTE), in which the sample is periodically heated directly, and front-PTE (F-PTE), in which the sensor is heated directly. In B-PTE, a scan has been done by varying laser chopping frequency and the thermal diffusivity is the outcome. On the other hand, in F-PTE, a thickness scan of the coupling fluid in between the sample and sensor is used to find sample's thermal effusivity. Validation experiments have been conducted by choosing solid samples in wide range of thermal properties.
This novel PTE technique has some notable advantages like, possibility of direct thermal characterization of TE materials and its inherent simplicity. This technique can be used to thermally characterize different TE materials regardless their nature (polymers, glasses, metallic or semiconducting materials). At the same time, due to the lower electrical resistivity of used TE materials, the noise levels were observed as low as 50 nV in the experimental frequency domain. On the other hand, a higher laser power (about 750 mW at 8 mm spot size) is used to conduct the experiments.

This thesis primarily focused on the investigation of thermal transport studies of PDLC samples. Studies on these system's thermophysical properties vs. temperature, LC concentration, various kinds of LCs and polymer matrix will help to understand thermal transport behaviour in different circumstances. In a thermal point of view, these studies not only help to understand fundamental heat transport in heterogeneous systems but also contribute to the developments of electrically controlled heat shutters.

In the field of thermoelectric material research, a broad and extensive research works are being conducted by various research teams around the world to develop high efficient heat conversion materials. Our works on the thermal behaviour of certain samples by a chosen method must be investigated further by different nanotube concentrations, lengths of nanotubes, different host polymer matrices etc. in order to optimize them for producing highest efficiency. More than that, samples prepared by various methods (e.g., mechanical mixing, in situation polymerization and so on) could give more insight on the thermal transport through nano-composites and the role of Kapitza resistance with respect to

nanotube addition to the host matrix. Temperature dependent measurements are also needed to predict their performances in different temperatures.

As part of the PTE technique, further studies are needed to develop or find sensors which work at lower laser powers. This could be directly related to the Seebeck coefficients of materials. At the same time materials with higher electrical resistance (typically more than a few tens of ohms through sensor thickness) is preferable for the collection of generated majority carriers from both surface of the sensor efficiently via thin coatings.

Appendix

Beer-Lambert law: If I be the intensity of the transmitted light through a layer of material with thickness z for an incident intensity of radiation I_0. According to Beer-Lambert law:

$$I = I_0 e^{-\beta z}, (z \geq 0)$$

where, β is known as the attenuation coefficient (or optical absorption coefficient), given by:

$$\beta = -\frac{1}{z} \ln \left(\frac{I}{I_0} \right)$$

In such condition for absorption, the optical intensity of the light wave, (I), is exponentially reduced while travelling through the medium. Reciprocal of β is called penetration depth, the depth at which the intensity reduced by a factor of $1/e$ of the original signal.

Extinction Coefficient: The optical absorption coefficient can also be expressed as,

$$\beta = 4\pi K/\lambda$$

where, λ is the wavelength of the incident radiation and K is the extinction coefficient.

Solving by separation of variable method: The temperature field ($T(z,t)$), function of space and time, can be expressed as the product of two ordinary differential equations, given by:

$$T(z,t) = F(z)G(\tau) \tag{A-1}$$

Substituting eq. (A-1) into eq. (2.12) and dividing by the product $f\,g$ and excluding the source term gives:

$$\alpha \frac{1}{F} \frac{d^2F}{dz^2} = \frac{1}{G} \frac{dG}{d\tau} \tag{A-2}$$

Since both sides of the eq. (A-2) can vary quite independently of each other, the only way that this can happen is if the two side are equal to a constant. So both sides of the equation can be written as:

$$\alpha \frac{1}{F} \frac{d^2F}{dz^2} = \Lambda \tag{A-3}$$

$$\frac{1}{G} \frac{dG}{d\tau} = \Lambda \tag{A-4}$$

Substituting eq. (2.13) in eq. (A-4) for the time dependance gives:

$$\frac{1}{G} \frac{dG}{d\tau} = \Lambda = \frac{1}{e^{i\omega t}} \, i\omega \, e^{i\omega t} = i\omega \tag{A-5}$$

Substituting Λ from eq. (A-5) in the z dependent eq. (A-4) gives:

$$\frac{d^2F}{dz^2} = i\omega \frac{F}{\alpha} \tag{A-6}$$

This can also be expressed as an exponential solution, say $[e^{\sigma z}]$.

Bibliography

[1] Michael J Rightley, John A Emerson, C Channy Wong, Dale L Huber, and Blake Jakaboski. Advancement in Thermal Interface Materials for Future High-Performance Electronic Applications : Part 1. Technical Report February, Sandia National Laboratories, 2007. (document)

[2] A P C Ribeiro, S I C Vieira, J M França, C S Queirós, E Langa, M J V Lourenço, S M S Murshed, and C A Nieto De Castro. Thermal Properties of Ionic Liquids and Ionanofluids. 2009. (document)

[3] Nidhi Dubey and Mario Leclerc. Conducting polymers: Efficient thermoelectric materials. *Journal of Polymer Science Part B: Polymer Physics*, 49(7):467–475, April 2011. (document), 4.2.2.1

[4] Donald Hopkins, Ronald H Brown, and Mary L Good. PREDICTING THE IGNITION TIME AND BURNING RATE OF THERMOPLASTICS IN. (September), 1995. (document)

[5] Yulong Ding, Hajar Alias, Dongsheng Wen, and Richard A Williams. Heat transfer of aqueous suspensions of carbon nanotubes (CNT nanofluids). *International Journal of Heat and Mass Transfer*, 49(1-2):240–250, January 2006. (document)

[6] M. J. Assael, I. N. Metaxa, K. Kakosimos, and D. Constantinou. Thermal Conductivity of Nanofluids-Experimental and Theoretical. *International Journal of Thermophysics*, 27(4):999–1017, August 2006. (document)

[7] Anna Matvienko, Andreas Mandelis, and Stephen Abrams. Robust multiparameter method of evaluating the optical and thermal properties of a layered tissue struc-

ture using photothermal radiometry. *Applied optics*, 48(17):3192–203, June 2009. (document)

[8] Zheyu Shen, Ken Terao, Yasuyuki Maki, Toshiaki Dobashi, Guanghui Ma, and Takao Yamamoto. Synthesis and phase behavior of aqueous poly(N-isopropylacrylamide-co-acrylamide), poly(N-isopropylacrylamide-co-N,N-dimethylacrylamide) and poly(N-isopropylacrylamide-co-2-hydroxyethyl methacrylate). *Colloid and Polymer Science*, 284(9):1001–1007, April 2006. (document)

[9] Santhosh Onkaraiah and Chuan Seng Tan. Mitigating heat dissipation and thermo-mechanical stress challenges in 3-D IC using thermal through silicon via (TTSV). *2010 Proceedings 60th Electronic Components and Technology Conference (ECTC)*, pages 411–416, 2010. (document)

[10] http://techon.nikkeibp.co.jp/NEA/archive/200401/283392/. Design view from japan: Oki electric tackles heat dissipation. (document)

[11] Bo Feng, Zhixin Li, and Xing Zhang. Prediction of size effect on thermal conductivity of nanoscale metallic films. *Thin Solid Films*, 517(8):2803–2807, February 2009. (document)

[12] S Y Lu and J L Song. Effect of interfacial characteristics on effective conductivities of composites containing randomly distributed aligned long fibers. *Chemical engineering science*, 51(19), 1996. (document)

[13] Sergei Shenogin. Role of thermal boundary resistance on the heat flow in carbon-nanotube composites. *Journal of Applied Physics*, 95(12):8136, 2004. (document)

[14] S.S.A. Seo, H.N. Lee, and T.W. Noh. Infrared spectroscopy of CaTiO3, SrTiO3, BaTiO3, Ba0.5Sr0.5TiO3 thin films, and (BaTiO3)5/(SrTiO3)5 superlattice grown on SrRuO3/SrTiO3(001) substrates. *Thin Solid Films*, 486(1-2):94–97, August 2005. (document)

[15] Stefan Zollner, A. A. Demkov, R. Liu, P. L. Fejes, R. B. Gregory, Prasad Alluri, J. A. Curless, Z. Yu, J. Ramdani, R. Droopad, T. E. Tiwald, J. N. Hilfiker, and J. A. Woollam. Optical properties of bulk and thin-film SrTiO 3 on Si and Pt. *Journal of vacuum science and technology. B*, 18(4):2242–2254, 2000. (document)

[16] L. Liang and Baowen Li. Size-dependent thermal conductivity of nanoscale semiconducting systems. *Physical Review B*, 73(15):1–4, April 2006. (document)

[17] F L A Richardson, S D Peacor, C. Uher, and Franc0 Nori. YBa2Cu307-a films : Calculation path of the thermal conductiwity and phonon mean free path. *Journal of Applied Physics*, 72(10):4788–4791, 1992. (document)

[18] David G. Cahill, Wayne K. Ford, Kenneth E. Goodson, Gerald D. Mahan, Arun Majumdar, Humphrey J. Maris, Roberto Merlin, and Simon R. Phillpot. Nanoscale thermal transport. *Journal of Applied Physics*, 93(2):793, 2003. (document)

[19] Nicolas Houriez. *Etude du Transport Thermique dans des Fluides Complexes par Calorimetrie Photopyroelectric*. PhD thesis, UDSMM, Université littoral côte d'opale, Dunkerque, France, 2008. (document)

[20] T. Bouchaour, F. Benmouna, F. Roussel, J.-M. Buisine, X. Coqueret, M. Benmouna, and U. Maschke. Equilibrium phase diagram of poly(2-phenoxyethylacrylate) and 5CB. *Polymer*, 42(4):1663–1667, February 2001. (document), 3.23

[21] U. Maschke, A. Daoudi, F. Benmouna, F. Roussel, J.M. Buisine, X. Coqueret, and M. Benmouna. Equilibrium phase properties of polymer/liquid crystal blends: Theory and experiments. *Molecular Crystals and Liquid Crystals*, 365:1361–1369, 2001. (document)

[22] Roch Chan Yu King, Frédérick Roussel, Jean-François Brun, and Carole Gors. Carbon nanotube-polyaniline nanohybrids: Influence of the carbon nanotube characteristics on the morphological, spectroscopic, electrical and thermoelectric properties. *Synthetic Metals*, 162(15-16):1348–1356, September 2012. (document), 4.1, 4.2.2.2, 4.4

[23] Abdelhak Hadj Sahraoui, Sylvain Delenclos, Stéphane Longuemart, and Dorin Dadarlat. Heat transport in polymer-dispersed liquid crystals under electric field. *Journal of Applied Physics*, 110(3):033510, 2011. (document), 3.2.1.2, 3.2.2.2, 3.3.4.1

[24] Sarah Darby. *Literature review for the Energy Demand Research Project*. PhD thesis, University of Oxford. (document)

[25] Kenji Morita. Automotive power source in 21st century. *JSAE Review*, 24(July 2002):3–7, 2003. (document)

[26] Bruno Gervet. *Global Warming is mainly a result of Heat Emissions*. PhD thesis, Lulea University of Technology, Sweden, 2007. (document)

[27] C. White, R. Steeper, and A. Lutz. The hydrogen-fueled internal combustion engine: a technical review. *International Journal of Hydrogen Energy*, 31(10):1292–1305, August 2006. (document)

[28] Thamir K Ibrahim, M M Rahman, and Ahmed N Abdalla. Improvement of gas turbine performance based on inlet air cooling systems : A technical review. *International Journal of Physical Sciences*, 6(4):620–627, 2011. (document)

[29] David Michael Rowe. Review THERMOELECTRIC WASTE HEAT RECOVERY AS A RENEWABLE ENERGY SOURCE. *International Journal of Innovations in Energy Systems and Power*, 1(1):13–23, 2006. (document), 4.1

[30] Harumi Yokokawa. Materials for clean energy conversion. (document)

[31] Alaxander Graham Bell. Production of Sound by Radiant Energy. *Manufacturer and Builder (1869 - 1894)*, 0013(7):156–158, July 1881. 1.1, 1.1

[32] Qifang He, Reeta Vyas, and R. Gupta. Theory of photothermal spectroscopy in an optically dense fluid. *Applied Optics*, 36(9):1841–1859, 20 march 1997. 1.1

[33] Y.-X. Nie and L. Bertrand. Separation of surface and volume absorption by photothermal deflection. *Journel of Applied Physics*, 65(2):438–447, 15 January 1989. 1.1

[34] O.W. Käding, H. Skurk, A.A. Maznev, and E. Matthias. Transient thermal gratings at surfaces for thermal characterization of bulk materials and thin films. *Applied Physics A*, 61:253–261, 1995. 1.1

[35] V. Gusev, C. Desmet, W. Lauriks, C. Glorieux, and J. Thoen. Theory of Scholte, leaky Rayleigh, and lateral wave excitation via the laser-induced thermoelastic effect. *Journel of Acoustic Society of America*, 100(3):1514, september 1996. 1.1

[36] Andreas Mandelis and Martin M. Zver. Theory of photopyroelectric spectroscopy of solids. *Journel of Applied Physics*, 57(9):4421, May 1985. 1.1, 1.2.1, 2.2, 3.1.2.2

[37] N. Kawaguchi, Y. Nagasaka, and A. Nagashima. Fully automated apparatus to measure the thermal conductivity of liquids by the transient hot-wire method. *Review of Scientific Instruments*, 56(9):1788, 1985. 1.2

[38] H. Takahashi, Y. Hiki, and Y. Kogure. An improved transient hot-wire method for studying thermal transport in condensed matter. *Review of Scientific Instruments*, 65(9):2901, 1994. 1.2

[39] R. G. Richard and I. R. Shankland. A transient hot-wire method for measuring the thermal conductivity of gases and liquids. *International Journal of Thermophysics*, 10(3):673–686, May 1989. 1.2

[40] David G. Cahill and R. O. Pohl. Thermal conductivity of amorphous solids above the plateau. *Physical Review B*, 35(8):4067–4073, 1987. 1.2

[41] M. Chirtoc Mihailescu and G. Theory of the photopyroelectric method for investigation of optical and thermal materials properties. *Physical Review B*, 40, No: 14(November):9606–9617, 1989. 1.2.1

[42] Stephane Longuemart. *Study on Liquid Crystal and ferro fluids using Photopyroelectric Technique*. theses, université littoral côte d'opale, 2002. 1.2.1, 4.2.2.3

[43] S. Delenclos, D. Dadarlat, N. Houriez, S. Longuemart, C. Kolinsky, and A. Hadj Sahraoui. On the accurate determination of thermal diffusivity of liquids by using the photopyroelectric thickness scanning method. *Review of Scientific Instruments*, 78(2):024902, 2007. 1.2.1

[44] Dorin Dadarlat, Mircea Nicolae Pop, Mihaela Streza, Stephane Longuemart, Michael Depriester, Abdelhak Hadj Sahraoui, and Viorica Simon. Combined FPPE-PTR Calorimetry Involving TWRC Technique II. Experimental : Application to Thermal Effusivity Measurements of Solids. *International Journal of Thermophysics*, pages 2092–2101, 2011. 1.2.1, 2.2.1, 3.2.4

[45] Preethy Chirukandath Menon, Ravindran Nair Rajesh, and Christ Glorieux. High accuracy, self-calibrating photopyroelectric device for the absolute determination of thermal conductivity and thermal effusivity of liquids. *The Review of scientific instruments*, 80(5):054904, May 2009. 1.2.1, 3.3, 3.2.2.1

[46] J Caerels, C Glorieux, and J Thoen. Photopyroelectric thermal wave setup for the absolute measurement of the thermal conductivity of low density gases. *Review of Scientific Instruments*, 71(9), 2000. 1.2.1

[47] U. Zammit, M. Marinelli, F. Mercuri, S. Paoloni, and F. Scudieri. Invited Review Article: Photopyroelectric calorimeter for the simultaneous thermal, optical, and structural characterization of samples over phase transitions. *The Review of scientific instruments*, 82(12):121101, December 2011. 1.2.1, 1.3.4

[48] M M Farrow, R K Burnham, M Auzanneau, S L Olsen, N Purdie, and E M Eyring. Piezoelectric detection of photoacoustic signals. *Applied optics*, 17(7):1093–8, April 1978. 1.2.2

[49] A Hordvik and L Skolnik. Photoacoustic measurements of surface and bulk absorption in HF/DF laser window materials. *Applied optics*, 16(11):2919–24, November 1977. 1.2.2

[50] Per Helander and Ingemar Lundstrom. Separation of bulk and surface light adsorption with an open photoacoustic cell. *Journal of Applied Physics*, 54(9):5069, 1983. 1.2.2

[51] Maju Kuriakose, Michael Depriester, Roch Chan Yu King, Frédérick Roussel, and Abdelhak Hadj Sahraoui. Photothermoelectric effect as a means for thermal characterization of nanocomposites based on intrinsically conducting polymers and carbon nanotubes. *Journal of Applied Physics*, 113(4):044502, 2013. 1.2.3

[52] L. B. Kreuzer. Ultralow Gas Concentration Infrared Absorption Spectroscopy. *Journal of Applied Physics*, 42(7):2934, 1971. 1.3.1

[53] A. Rosencwaig. Photoacoustic scpectroscopy of solids. *Optics Communications*, 7(4):305–308, April 1973. 1.3.1

[54] H Vargas and L. C. M. Miranda. Photoacoustic and related photothermal techniques and related photothermal. *Physics Reports*, 161(2):43–101, 1988. 1.3.1, 1.3.4

[55] W B Jackson, N M Amer, a C Boccara, and D Fournier. Photothermal deflection spectroscopy and detection. *Applied optics*, 20(8):1333–44, April 1981. 1.3.2

[56] A. C. Boccara, D. Fournier, and J. Badoz. Thermo-optical spectroscopy: Detection by the "mirage effect". *Applied Physics Letters*, 36(2):130, 1980. 1.3.2

[57] Yongwu Yang and Keith A Nelson. Impulsive stimulated light scattering from glass-forming liquids. I. Generalized hydrodynamics approach. *Journal of Chemical Physics*, 103(June):7722–7731, 1995. 1.3.3

[58] A.A. Maznev, K.A. Nelson, and J. A. Rogers. Optical heterodyne detection of laser-induced gratings. *Optics letters*, 23(16):1319–21, August 1998. 1.3.3

[59] Rebecca M. Slayton, Keith a. Nelson, and a. a. Maznev. Transient grating measurements of film thickness in multilayer metal films. *Journal of Applied Physics*, 90(9):4392, 2001. 1.3.3

[60] Dora M Paolucci and Keith A Nelson. Impulsive stimulated thermal scattering study of structural relaxation in supercooled glycerol. *Journal of Chemical Physics*, 112(15), 2000. 1.3.3

[61] John A Rogers and Keith A Nelson. Study of Lamb acoustic waveguide modes in unsupported polyimide f Urns using real-time impulsive stimulated thermal scattering. *Journal of Applied Physics*, 75(3):1534–1556, 1994. 1.3.3

[62] A Mandelis, A Othonos, and C Christofides. Non-contacting measurements of photocarrier lifetimes in bulk- and polycrystalline thin-film Si photoconductive devices by photothermal radiometry. *Journal of Applied Physics*, 80(9):5332–5341, 1996. 1.3.4

[63] H. Vargas and L. C. M. Miranda. Photothermal techniques applied to thermophysical properties measurements (plenary). *Review of Scientific Instruments*, 74(1):794, 2003. 1.3.4, 3.1.3

[64] G Busse. Optoacoustic and photothermal material inspection techniques. *Applied optics*, 21(1):107–10, January 1982. 1.3.4

[65] D. P. Almond and P. M. Patel. *Photothermal Science and Techniques*. chapman & Hall, 1996. 1.3.4, 2.1, 3.1.3

[66] Agustín Salazar. Energy propagation of thermal waves. *European Journal of Physics*, 27(6):1349–1355, November 2006. 2.1

[67] Allan Rosencwaig and Allen Gersho. Theory of the photoacoustic effect with solids. *Journal of Applied Physics*, 47(1):64–69, January 1976. 2.1, 2.2

[68] R. Santos and L. C. M. Miranda. Theory of the photothermal radiometry with solids. *Journal of Applied Physics*, 52(6):4194, 1981. 2.2, 3.1

[69] A. L. Edwards. A Compilation of Thermal Property Data for Computer Heat-Conduction Calculations. UCRL-50589, University of California Lawrence Radiation Laboratory, 24 February 1969. 2.2.1

[70] D. Dadarlat. Photopyroelectric calorimetry of liquids; recent development and applications. *Laser Physics*, 19(6):1330–1339, June 2009. 2.2.1, 3.2.4, 4.5.5

[71] Per-Erik Nordal and Svein Otto Kanstad. Photothermal Radiometry. *Physica Scripta*, 20:659–662, 1979. 3.1

[72] S. J. Sheard and M. G. Somekh. Measurement of opaque coating thickness using photothermal radiometry. *Applied Physics Letters*, 53(26):2715, 1988. 3.1

[73] H. P. R. Frederikse and X. T. Ying. Heat conductivity of oxide coatings by photothermal radiometry between 293 and 1173 K. *Applied optics*, 27(22):4672–5, November 1988. 3.1

[74] Jean Lazare and Nzodoum Fotsing. *Investigation of Thermal Transport in Layered Sytems and Micro-structured Semiconductor Devices by Photothermal Techniques and Finite Element Simulations*. PhD thesis, 2004. 3.1

[75] Eric P. Visser, Erwin H. Versteegen, and Willem J. P. van Enckevort. Measurement of thermal diffusion in thin films using a modulated laser technique: Application to chemical-vapor-deposited diamond films. *Journal of Applied Physics*, 71(7):3238, 1992. 3.1

[76] A. Kusiak, Ch. Pradere, and J. L. Battaglia. Measuring the thermal conductivity of liquids using photo-thermal radiometry. *Measurement Science and Technology*, 21(1):015403, January 2010. 3.1

[77] K Sreekumar and V K Vaidyan. Measurement of thermal effusivity of liquids using a photothermal imager. *Measurement Science and Technology*, 17(4):666–669, April 2006. 3.1

[78] Maju Kuriakose, Michael Depriester, Dorin Dadarlat, and Abdelhak Hadj Sahraoui. Improved methods for measuring thermal parameters of liquid samples using photothermal infrared radiometry. *Measurement Science and Technology*, 24(2):025603, February 2013. 3.1.2

[79] J. A. Balderas-López and A. Mandelis. Self-normalized photothermal technique for accurate thermal diffusivity measurements in thin metal layers. *Review of Scientific Instruments*, 74(12):5219, 2003. 3.1.2.1, 4.5

[80] M. Chirtoc and G. Mihailescu. Theory of the photopyroelectric method for investigation of optical and thermal materials properties. *Physical Review B*, 40(14):9606–9617, November 1989. 3.1.2.2

[81] D. R. Lide. *CRC Handbook of Chemistry and Physics 78th edition*. CRC Press, Boca Raton Newyork. 3.1, 3.2, 3.3, 3.4, 3.3.2

[82] M. Depriester, P. Hus, S. Delenclos, and A. Hadj Sahraoui. New methodology for thermal parameter measurements in solids using photothermal radiometry. *Review of Scientific Instruments*, 76(7):074902, 2005. 3.1.2.3, 4.3

[83] J A Balderas-lópez, Andreas Mandelis, and J A García. Measurements of the Thermal Diffusivity of Liquids with a Thermal - Wave Resonator Cavity. *Analytical Sciences*, 17:519–522, 2001. 3.3

[84] Mitchell L Schlossman and Justin P Mccarthy. Lanolin and Its Derivatives. *Journel of the american oil chemists' society*, 447:447–450, 1977. 3.2.1.1

[85] M. Marinelli, F. Mercuri, U. Zammit, and F. Scudieri. Thermal conductivity and thermal diffusivity of the cyanobiphenyl (nCB) homologous series. *Physical Review E*, 58(5):5860–5866, 1998. 3.2.1.2, 3.2.2.3, 3.3.2, 3.5

[86] David D. Jackson. Most Squares Inversion. *Journal of Geophysical Research*, 81(5):1027–1030, 1976. 3.2.2.1

[87] Qingsheng Zeng, Sheng Wang, Leijing Yang, Zhenxing Wang, Tian Pei, Zhiyong Zhang, Lian-Mao Peng, Weiwei Zhou, Jie Liu, Weiya Zhou, and Sishen Xie. Carbon nanotube arrays based high-performance infrared photodetector [Invited]. *Optical Materials Express*, 2(6):839, May 2012. 3.2.4

[88] J.L.Fergason. Polymer encapsulated nematic liquid crystals for display and light control applications. *SID Int. Symp. Dig. Tech. Pap.*, 16(4,435,047):68, 1985. 3.3

[89] J. W. Doane, N. a. Vaz, B.-G. Wu, and S. Zumer. Field controlled light scattering from nematic microdroplets. *Applied Physics Letters*, 48(4):269, 1986. 3.3

[90] F. Basile, F. Bloisi, L. Vicari, and F. Simoni. Optical phase shift of polymer-dispersed liquid crystals. *Physical Review E*, 48(1):432, 1993. 3.3

[91] Yi-Hsin Lin, Hongwen Ren, and Shin-Tson Wu. High contrast polymer-dispersed liquid crystal in a 90^0 twisted cell. *Applied Physics Letters*, 84(20):4083, 2004. 3.3

[92] V. K. S. Hsiao and W.-T. Chang. Optically switchable, polarization-independent holographic polymer dispersed liquid crystal (H-PDLC) gratings. *Applied Physics B*, 100(3):539–546, March 2010. 3.3

[93] V. A. Loiko and A. V. Konkolovich. Focusing of light by polymer-dispersed liquid-crystal films with nanosized droplets. *Journal of Experimental and Theoretical Physics*, 103(6):935–943, December 2006. 3.3

[94] R. W. Sillars. The properties of a dielectric containing semi- conducting particles of various shapes. *Wireless Section, Institution of Electrical Engineers*, 80:378–394, 1937. 3.3.1

[95] Karl Willy Wagner. Erklärung der dielektrischen Nachwirkungsvorgänge auf Grund Maxwellscher Vorstellungen. *Archiv für Elektrotechnik*, 2(9):371–387, September 1914. 3.3.1

[96] Ragab M. Soliman. *Early Stages of Polymer Crystalization Studied by Dielectric Spectroscopy*. PhD thesis, Universität Rostock, 2004. 3.3.1

[97] Mourad Boussoualem, Roch Chan Yu King, Jean-François Brun, Benoît Duponchel, Mimoun Ismaili, and Frédérick Roussel. Electro-optic and dielectric properties of optical switching devices based on liquid crystal dispersions and driven by conducting polymer [poly(3,4-ethylene dioxythiophene):polystyrene sulfonate (PEDOT:PSS)]-coated electrodes. *Journal of Applied Physics*, 108(11):113526, 2010. 3.3.1

[98] Jinwoo Han. Memory and Depolarization Effects of Polymer-Dispersed Liquid Crystal Films Based on E7 / NOA61. *Journal of the Korean Physical Society*, 43(1):45–50, 2003. 3.3.1

[99] Mourad Boussoualem, Frédérick Roussel, and Mimoun Ismaili. Thermophysical, dielectric, and electro-optic properties of nematic liquid crystal droplets confined to a thermoplastic polymer matrix. *Physical Review E*, 69(031702):1–10, 2004. 3.3.1

[100] Mourad Boussoualem, Mimoun Ismaili, Jean-François Lamonier, Jean-Marc Buisine, and Frédérick Roussel. Polarization field effects at liquid-crystal-droplet-polymer interfaces. *Physical Review E*, 73(4):1–7, April 2006. 3.3.1

[101] Kelly J. R. and Seekola D. L. Dielectric losses in a polymer-dispersed liquid crystal film. volume 1257 of *Liquid Crystal Displays and Applications*. Proc. SPIE, 1990. 3.3.1

[102] P. S. Drzaic. *Liquid Crystal Dispersion*. World Scientific, Singapore, 1995. 3.3.1, 3.3.5.1, 3.3.5.3, 3.3.5.3

[103] F Roussel, Jm Buisine, U Maschke, X Coqueret, and F Benmouna. Phase diagrams and morphology of polymer dispersed liquid crystals based on nematic-liquid-crystal-monofunctional-acrylate mixtures. *Physical review. E, Statistical physics, plasmas, fluids, and related interdisciplinary topics*, 62(2 Pt A):2310–6, August 2000. 3.3.1

[104] Farida Benmouna, Abdelylah Daoudi, Frédérick Roussel, Jean-Marc Buisine, Xavier Coqueret, and Ulrich Maschke. Equilibrium phase diagram of polystyrene and 8cb. *Journal of Polymer Science Part B: Polymer Physics*, 37(15):1841–1848, 1999. 3.3.1

[105] G. W. Smith. Study of formation, phase behavior, and microdroplet size of a polyurethane-based polymer-dispersed liquid crystal. *Molecular Crystals and Liquid Crystals Incorporating Nonlinear Optics*, 180(2):201–222, 1990. 3.3.1

[106] G. Perrier and A. Bergeret. Maxwell-wagner-sillars relaxations in polystyrene-glass-bead composites. *Journel of Applied Physics*, 77:2651, 1995. 3.3.2

[107] Bo Gestblom and Stanislaw Wrobel. A thin cell dielectric spectroscopy method for liquid crystals. *Liquid Crystals*, 18(1):31–35, 1995. 3.3.2

[108] V. Allouchery. *Theses*. PhD thesis, Université du littoral côte d'Opale, Dunkerque, France, 2000. 3.3.2

[109] Abderrahim Boudenne and Smain Khaldi. Temperature and Liquid Crystal Concentration Effect on Thermal Conductivity of Poly (styrene) Dispersed 5CB Liquid Crystal. *Journal of Applied Polymer Science*, 89:481–486, 2003. 3.3.2

[110] Ce-Wen Nan, R. Birringer, David R. Clarke, and H. Gleiter. Effective thermal conductivity of particulate composites with interfacial thermal resistance. *Journal of Applied Physics*, 81(10):6692, 1997. 3.3.4.1

[111] J. W. Doane, A. Golemme, J. L. West, J. B. Whitehead Jr., and B. G. Wu. Polymer Dispersed Liquid Crystals for Display Application. *Molecular Crystals and Liquid Crystals Incorporating Nonlinear Optics*, 165(1):511, 1988. 3.3.5.3

[112] Terry Hendricks and William T. Choate. Engineering Scoping Study of Thermoelectric Generator Systems for Industrial Waste Heat Recovery. Technical Report November, 2006. 4.1

[113] G Jeffrey Snyder and Eric S Toberer. Complex thermoelectric materials. *Nature materials*, 7(2):105–14, February 2008. 4.1

[114] Deyu Li, Scott T. Huxtable, Alexis R. Abramson, and Arun Majumdar. Thermal Transport in Nanostructured Solid-State Cooling Devices. *Journal of Heat Transfer*, 127(1):108, 2005. 4.1

[115] Weishu Liu, Xiao Yan, Gang Chen, and Zhifeng Ren. Recent advances in thermoelectric nanocomposites. *Nano Energy*, 1(1):42–56, January 2012. 4.1

[116] G Chen, T Zeng, T Borca-Tasciuc, and D Song. Phonon engineering in nanostructures for solid-state energy conversion. *Materials Science and Engineering: A*, 292(2):155–161, November 2000. 4.1

[117] Hideki Shirakawa, Edwin J. Louis, Alan G. MacDiarmid, Chwan K. Chiang, and Alan J. Heeger. Synthesis of electrically conducting organic polymers: halogen derivatives of polyacetylene, (CH) x. *Journal of the Chemical Society, Chemical Communications*, (16):578, 1977. 4.1

[118] A. J. Minnich, M. S. Dresselhaus, Z. F. Ren, and G. Chen. Bulk nanostructured thermoelectric materials: current research and future prospects. *Energy & Environmental Science*, 2(5):466, 2009. 4.1

[119] A. Mandelis. *Diffusion-Wave Fields, Mathematical Methods and Green Functions*. Springer Verlag New York, 2001. 4.2

[120] A. Hadj Sahraoui, S. Longuemart, D. Dadarlat, S. Delenclos, C. Kolinsky, and J. M. Buisine. The application of the photopyroelectric method for measuring the thermal parameters of pyroelectric materials. *Review of Scientific Instruments*, 73(7):2766, 2002. 4.2

[121] D D Ateh, H a Navsaria, and P Vadgama. Polypyrrole-based conducting polymers and interactions with biological tissues. *Journal of the Royal Society, Interface / the Royal Society*, 3(11):741–52, December 2006. 4.2.2.1

[122] John D W Madden, Bryan Schmid, Martin Hechinger, Serge R Lafontaine, G A Peter, Franz S Hover, Richard Kimball, and Ian W Hunter. Application of Polypyrrole Actuators : Feasibility of Variable Camber Foils. *IEEE Journal of Oceanic Engineering*, 2003. 4.2.2.1

[123] Eric Hu, Akif Kaynak, and Yuncang Li. Development of a cooling fabric from conducting polymer coated fibres: Proof of concept. *Synthetic Metals*, 150(2):139–143, April 2005. 4.2.2.1

[124] Uffana Riaz, S.M. Ashraf, and Sharif Ahmad. High performance corrosion protective DGEBA/polypyrrole composite coatings. *Progress in Organic Coatings*, 59(2):138–145, May 2007. 4.2.2.1

[125] Mihaela Baibarac and Pedro Gómez-Romero. Nanocomposites Based on Conducting Polymers and Carbon Nanotubes from Fancy Materials to Functional Applica-

tions. *Journal of Nanoscience and Nanotechnology*, 6(11):3325–3328, November 2006. 4.2.2.1

[126] Alan G Macdiarmid. "Synthetic Metals" : A Novel Role for Organic Polymers (Nobel Lecture). *Angew. Chem. Int. Ed*, 40:2581–2590, 2001. 4.2.2.1

[127] Y. Xuan, X. Liu, S. Desbief, P. Leclère, M. Fahlman, R. Lazzaroni, M. Berggren, J. Cornil, D. Emin, and X. Crispin. Thermoelectric properties of conducting polymers: The case of poly(3-hexylthiophene). *Physical Review B*, 82(11):1–9, September 2010. 4.2.2.1

[128] Dasaroyong Kim, Yeonseok Kim, Kyungwho Choi, Jaime C Grunlan, and Choongho Yu. Improved thermoelectric behavior of nanotube-filled polymer composites with poly(3,4-ethylenedioxythiophene) poly(styrenesulfonate). *ACS nano*, 4(1):513–23, January 2010. 4.2.2.1

[129] Kanishka Biswas, Jiaqing He, Ivan D Blum, Chun-I Wu, Timothy P Hogan, David N Seidman, Vinayak P Dravid, and Mercouri G Kanatzidis. High-performance bulk thermoelectrics with all-scale hierarchical architectures. *Nature*, 489(7416):414–8, September 2012. 4.2.2.1

[130] M Chirtoc, E H Bentefour, C Glorieux, and J Thoen. Development of the front-detection photopyroelectric (FPPE) configuration for thermophysical study of glass-forming liquids. *Thermochimica Acta*, 377:105–112, 2001. 4.2.2.3

[131] H. K. Park, C. P. Grigoropoulos, and A. C. Tam. Optical Measurements of Thermal Diffusivity of a Material. *International Journal of Thermophysics*, 16(4):973–995, 1995. 4.3

[132] Jyotsna Ravi, Yuekai Lu, Stéphane Longuemart, Stefano Paoloni, Helge Pfeiffer, Jan Thoen, and Christ Glorieux. Optothermal depth profiling by neural network infrared radiometry signal recognition. *Journal of Applied Physics*, 97(1):014701, 2005. 4.3

[133] M. Streza, D. Dadarlat, M. N. Pop, C. Prejmerean, D. Prodan, M. Depriester, S. Longuemart, and A. Hadj Sahraoui. Photothermal radiometry (PTR) investigation of dynamic thermal parameters of dental composites. *Optoelectronics and Advanced Materials-Rapid Communications*, 4(11):1830–1834, 2010. 4.3, 4.3

[134] Michael Depriester. *Study on carbon nanotube based composites using photothermal radiometry.* PhD thesis, Université littoral côte d'Opale, 2007. 4.3

[135] Ce-Wen Nan, Gang Liu, Yuanhua Lin, and Ming Li. Interface effect on thermal conductivity of carbon nanotube composites. *Applied Physics Letters*, 85(16):3549, 2004. 4.4

[136] Jun Shen and Andreas Mandelis. Thermal-wave resonator cavity. *Review of Scientific Instruments*, 66(10):4999–5005, 1995. 4.5

[137] J. A. Balderas-López, A. Mandelis, and J. A. Garcia. Thermal-wave resonator cavity design and measurements of the thermal diffusivity of liquids. *Review of Scientific Instruments*, 71(7):2933, 2000. 4.5

[138] M. Marinelli, F. Mercuri, U. Zammit, R. Pizzoferrato, F. Scudieri, and D. Dadarlat. Photopyroelectric study of specific heat, thermal conductivity, and thermal diffusivity of Cr2O3 at the Neel transition. *Physical Review B*, 49(14):9523–9532, 1994. 4.5

[139] D. Dadarlat, M. Streza, M. N. Pop, V. Tosa, S. Delenclos, S. Longuemart, and a. Hadj Sahraoui. Photopyroelectric calorimetry of solids. *Journal of Thermal Analysis and Calorimetry*, 101(1):397–402, November 2009. 4.5.3

[140] Dorin Dadarlat and Camelia Neamtu. High Performance Photopyroelectric Calorimetry of Liquids. *Acta Chim. Slov.*, 56:225–236, 2009. 4.5.4

[141] Chirtoc M., Antoniov J. S., and Egee M. The Effective Thermal Thickness: A New Concept for Photothermal Investigation of Layered Systems. In *Proc 10-th Int. Conf. on Photoacoustic and Photothermal Phenomena (Rome, 84-86)*, 1998. 4.5.5

[142] A Mandelis. *Principles and perspectives of photothermal and photoacoustic phenomena.* New York: Elsevier, 1992. 4.5.5.1

[143] D. Dadarlat. Contact and non-contact photothermal calorimetry for investigation of condensed matter. *Journal of Thermal Analysis and Calorimetry*, 110(1):27–35, January 2012. 4.5.5.1, 4.5.5.1

[144] Touloukian YS. *Thermophysical Properties of High Temperatures Solid Materials.* New York: MacMillan, 1967. 4.5.5.1

[145] Masaru Nakamura, Shunji Takekawa, and Kenji Kitamura. Anisotropy of thermal conductivities in non- and Mg-doped near-stoichiometric LiTaO3 crystals. *Optical Materials*, 32(11):1410–1412, September 2010. 4.5.5.1